

CALIBRATION OF THE
PRODUCTION RATES OF
COSMOGENIC ^{36}Cl FROM
POTASSIUM

BY

Jodie Manderson Evans

A thesis submitted for the degree of
Doctor of Philosophy
at The Australian National University

July, 2001

For
Ciaran and Heather

Preface

This thesis describes the complete calibration of ^{36}Cl produced *in-situ* from potassium. This project was suggested by Dr John Stone and Dr Keith Fifield, and carried out at the Australian National University (ANU) jointly between the Research School of Earth Sciences (RSES), and the Department of Nuclear Physics, RSPHysSE. The author has taken primary responsibility from the beginning of this project to its conclusion. This has involved collecting the samples, performing mineral separations, preparing them for many different measurements, performing the measurements, and finally, carrying out the analysis and interpreting the data. During this process the author was assisted and advised by many people, as discussed below.

With the exception of the samples AT-10, AT-11, AT-12 and AT-13, which were collected by Dr Stone, all the Scottish samples were collected by the author with advice from Dr Colin Ballantyne and assistance from Keith Salt, Matt Franks, Angela Lamb and Dr Greg Lane. The samples for the depth profile from Wyangala were collected by the author with Dr Stone, Dr Fifield, Dr Richard Cresswell, Dr Mariana Di Tada and Dr Kexin Liu.

The original trace element measurements were made by ICP-MS at RSES with assistance from Mr Leslie Kinsley. X-ray fluorescence measurements (major element whole rock concentrations and some whole rock uranium and thorium concentrations) were made by Dr Bruce Chappell in the Geology Department at ANU. Later repeat trace element measurements were made by Prompt Gamma Analysis by XRAL in Canada.

Potassium concentrations were measured by the author with assistance from Mrs Robyn Maier. Initial calcium measurements were made by the author with the assistance of Mr Mike Shelley. These measurements were then repeated at Ecowise Environmental Laboratories, Australia.

All chloride measurements (pyrohydrolysis and isotope dilution) were made by the author following processes developed by Dr Stone. Likewise AgCl

samples for the ^{36}Cl analyses were prepared by the author following procedures adapted by Dr Stone from the original work of Conrad *et al* [Con86] and Zreda *et al* [Zre91].

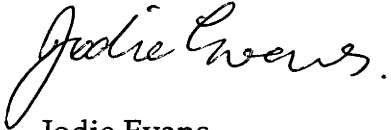
AMS measurements were made by the author using the 14UD Pelletron in the Department of Nuclear Physics. Successful ^{36}Cl measurements on the samples relied on the expertise of Dr Fifield and Dr Cresswell, and additional assistance in measuring the samples was provided by Dr Stone, Dr Di Tada and Dr Liu. Acquisition of the multi-parameter data for these measurements employed the software written for the laboratory's data acquisition system by Dr Gordon Foote. The subsequent off-line sorting of these data, which was required to derive the $^{36}\text{Cl}/\text{Cl}$ values, was carried out by the author using the same software.

Analysis and interpretation of the results was performed by the author with initial assistance from Mathematica programs written by Dr Stone and invaluable discussions with Dr Stone, Dr Fifield and Dr Lane.

The focus of this work has changed over time. The original intention was to include measurements made on eight samples collected from the Sierra Nevada, USA, by Dr Stone, and three samples collected in the Antarctic by Jeff Klein, but due to uncertainties in their exposure histories that became apparent after this work was underway, they were ultimately omitted from this dissertation. Some of the results obtained on these samples, in addition to four of the Scottish samples included in this work, can, however, be found in the following article:

J.M. Evans, J. O. H. Stone, L. K. Fifield and R. G. Cresswell
Cosmogenic chlorine-36 production in K-feldspar
Nucl. Instr. And Meth. In Phys. Res. B **123**, p 334 – 340, 1997.

No part of this thesis has been submitted for a degree at any other university.



Jodie Evans

Acknowledgements

*Today is gone. Today was fun.
Tomorrow is another one.
Everyday,
from here to there,
funny things are everywhere.*

Dr Seuss

As I put the finishing touches on my thesis I'm amazed at how interested I still am in the subject, and I have a twinge of regret that I won't be continuing the investigation. I don't believe that anyone really enjoys writing up their thesis, but I think I could make a pretty good case that my situation has been more difficult than most! I've gone from being single with no kids, to married with 2 (and it's the best thing that's ever happened to me!). I've moved overseas and back again twice. And I won't even go into how difficult it is to discuss your work with your supervisors when all three of you are living thousands of miles apart. But I will soon be finished and I have many people I would like to thank for helping me get from here to there.

First I would like to thank my "tag team" supervisors, John Stone and Keith Fifield. John's enthusiasm for the work has been inspiring, and I'm very grateful for his time and patience in teaching a physicist enough of the geology and chemistry to carry out the project. Keith's expertise with the accelerator, his efforts reading and rereading what I'm sure seemed like endless chapters so promptly, and keeping me focussed when I started stressing out at the end, were a godsend.

Thanks to all my official and unofficial advisers during my time here: Garry Allan, Richard Cresswell, Alan Chivas, Trevor Ophel and the person who is really responsible for me finishing, Greg Lane. George Dracoulis has supported me throughout my time at nuclear and I greatly appreciate his efforts at the very end as my default supervisor and critically reading my entire thesis in final form. (I'd also like to thank George for making sure the girls finally got a shower in the

refurbishment of the building!). On the RSES side of the road, I'd also like to thank Kurt Lambeck for his support of my Ph.D.

I'd like to thank Mariana Di Tada and Kexin Liu for all their special help making my final AMS measurements when I was nine months pregnant with Ciaran. Their support really meant a lot to me. I'd also like to thank Sam King and Phil Day for being great people!

As I said, I'm not a geologist, so I have to thank Colin Ballantyne, Keith Salt, Matt Franks and Angela Lamb for all their advice and assistance with collecting samples in Scotland.

I'd also like to thank everyone who helped me with various measurements at RSES: Robin Maier, Ian McDougall, John Chappell, Leslie Kinsley, Mike Shelley, John Mya, Shane Paxton and Joe Cali.

I'd like to express my appreciation to everyone at nuclear physics for being so supportive over the last 8 years, particularly Gordon Foote and Aidan Byrne, who have been my cheerleaders in the last 6 months, giving me words of encouragement every time they go past my desk to their offices, and Anna Wilson, Nanda Dasgupta and Susan Helyar for reading parts of my thesis. I'd also like to thank Clyde and Susan for being such great friends in Stony Brook!

I also really appreciate the help I got from both sets of grandparents when Greg went away for two weeks during the last month of writing up. I'd like to thank my brother for the words of encouragement I'm sure everyone else was thinking, but only he could give ("Just finish the bloody thing!"). I'd like to thank my Dad for his support and doing that last check for typos. And I'd like to thank my Mum for her support and, particularly, for finishing her thesis X years ago with three young kids!

Finally, I'd like to thank my two precious children, Ciaran and Heather, for their tolerance of mum disappearing to work all the time for the last couple of weeks, and being stressed and grumpy when she was at home. But mostly I'd like to thank my husband Greg, without whom there is no way I would have finished. He listened to me go on and on about various aspects of my thesis when we were living too far away from my supervisors to talk to them about it properly. He read pages and pages of rubbish I'd written, but most importantly he always believed I'd get there. Thank you!

Abstract

Chlorine-36 production rates from potassium have been calibrated for the top 10m of the lithosphere, where ^{36}Cl is produced by two main reaction channels: i) spallation, which dominates ^{36}Cl production in the top 2 metres below the earth's surface, and ii) negative muon capture, which dominates at depths of between 2 and ~20 metres below the earth's surface.

Rock samples were collected from two sites: i) rock surfaces exposed by the end of the Loch Lomond Readvance glaciation in Scotland 11,600 years ago, and ii) a 6.1m depth profile at a granite quarry in south eastern Australia, for which a steady state ^{36}Cl concentration dictated by a history of constant erosion was assumed. In addition, the ^{36}Cl measurements were made on pure K-feldspar mineral separates to remove the ^{36}Cl contributions from calcium, iron and titanium, and to minimise the ^{36}Cl contribution from chloride.

The potassium spallation production rate was deduced from 18 Scottish K-feldspar mineral separates to be $161 (9) \text{ atom (gK)}^{-1} \text{ yr}^{-1}$ at sea level and high latitude. This value lies between two earlier calibrations after these had been adjusted to allow for ^{36}Cl production by negative muon capture and low-energy neutron capture.

The ^{36}Cl yield per stopped negative muon was determined from 15 K-feldspar mineral separates in the depth profile to be $5.80(0.48) \times 10^{-2}$ atom per stopped μ^- at sea level and high latitude. Assuming a negative muon stopping rate of $175 \mu^- \text{ g}^{-1} \text{ yr}^{-1}$, with a 10% uncertainty, the ^{36}Cl production rate by negative muon capture on ^{39}K is $10.2 (1.3) \text{ atom (gK)}^{-1} \text{ yr}^{-1}$ at sea level and high latitude.

A calibration of the fast neutron flux just above the air/ground boundary was also obtained from ^{36}Cl measurements on eight pure quartz mineral separates prepared from the Scottish samples. This quantity is required for determining the ^{36}Cl production due to low-energy neutron capture on ^{35}Cl in the near-surface. A value of $740 (63) \text{ n (g air)}^{-1} \text{ yr}^{-1}$ scaled to sea level and high latitude was determined, which is ~35% higher than the previously published value.

Table of Contents

Chapter One

INTRODUCTION	1
--------------	---

Chapter Two

COSMOGENIC NUCLIDE PRODUCTION <i>IN-SITU</i>	7
2.1 Overview of Exposure Age Dating	7
2.2 Important Features of Cosmic Rays	11
2.2.1 Temporal and Spatial Variation of Cosmic Rays	13
2.2.2 Description of Important Cosmic Ray Induced Nuclear Reactions	14
2.3 <i>In-Situ</i> Production Channels for ^{36}Cl	20
2.3.1 Production due to Spallation	25
2.3.2 Production due to Negative Muon Capture	26
2.3.3 Production due to Low-Energy Neutron Capture	28
2.3.3A Thermal Neutrons Produced by Spallation Reactions	29
2.3.3B Epithermal Neutrons Produced by Spallation Reactions	31
2.3.3C Thermal Neutrons Produced by the Negative Muon Capture Reaction	33
2.3.3D Thermal Neutrons Produced by the Photodisintegration Reaction	34
2.3.3E Thermal Neutrons Produced by the Radioactive decay of U and Th	35
2.4 The Importance of AMS	36

Chapter Three

CALIBRATION OF THE PRODUCTION OF ^{36}Cl FROM POTASSIUM: BACKGROUND AND STRATEGY	39
3.1 Previous Work	39
3.1.1 The Calibration by Zreda <i>et. al.</i> (1991)	40
3.1.2 The Calibration by Swanson (1994)	42
3.1.3 The Calibration by Phillips <i>et. al.</i> (1996)	43

3.2 Low-energy Neutrons at the Air/Ground Boundary	45
3.2.1 Simulations of the Earth's Crust	46
3.2.2 Computational Models	47
3.2.3 Physically Isolating the $^{35}\text{Cl}(n,\gamma)^{36}\text{Cl}$ Channel	50
3.3 Calibration Strategy Adopted in this Study	52
3.3.1 Well-Constrained Exposure History	52
3.3.2 Potassium Concentration	57
3.3.3 Analysis Strategy	57
<i>Chapter Four</i>	
METHODOLOGY	61
4.1 Sample Collection	61
4.1.1 Surface Samples	62
4.1.2 Depth Profile	63
4.2 Chemical Preparation of Samples	63
4.2.1 Mineral Separation: K-feldspar and Quartz	63
4.2.2 AgCl Preparation	64
4.2.3 Major Element and Trace Element Compositions	66
4.3 Accelerator Mass Spectrometry	67
4.4 Chloride Measurements	71
4.4.1 Pyrohydrolysis	72
4.4.2 Isotope Dilution	73
<i>Chapter Five</i>	
^{36}Cl PRODUCTION DUE TO LOW-ENERGY NEUTRON CAPTURE: SCOTTISH QUARTZ MINERAL SEPARATES	75
5.1 Isolating the ^{36}Cl Produced by Low-Energy Neutron Capture on ^{35}Cl	75
5.2 The Scottish Quartz Samples	76
5.2.1 Evaluation of $\mathcal{P}_i(0)$	79
5.3 The Effects of Erosion and Local Geometry on the ^{36}Cl Produced from Low-Energy Neutrons	80
<i>Chapter Six</i>	
^{36}Cl PRODUCTION BY SPALLATION: SCOTTISH K-FELDSPAR MINERAL SEPARATES	83
6.1 Chlorine-36 Production from Spallation on Potassium	84

6.2 The Potassium Spallation Production Rate and Comparison with Previous Work	88
6.3 Measured vs. Model Dependent Correction of the Low-energy Neutron Capture on ^{35}Cl	89
 <i>Chapter Seven</i>	
^{36}Cl PRODUCTION DUE TO NEGATIVE MUON CAPTURE: WYANGALA DEPTH PROFILE	93
7.1 Surface Samples	94
7.2 The Depth Profile	99
7.3 Possible Sources of Uncertainty in the Derived Value of Y_K	104
7.3.1 The Possible Effect of Quarrying on the Calibration	105
7.3.2 Chlorine-36 Production by Low-energy Neutron Capture	106
7.4 Discussion on the Negative Muon Capture on Potassium Production Rate	108
 <i>Chapter Eight</i>	
CONCLUSIONS	111
 <i>Appendix A</i>	
EARLY ATTEMPTS AT ISOLATING THE ^{36}Cl PRODUCED BY LOW-ENERGY NEUTRON CAPTURE ON ^{35}Cl	117
A.1 Early Attempts: The Crushing Technique	117
A.2 Second Attempt: The Quartz Samples	119
 <i>Appendix B</i>	
THE SCOTTISH SAMPLES: SAMPLE LOCATIONS, WHOLE ROCK MEASUREMENTS AND DERIVED QUANTITIES	121
 <i>Appendix C</i>	
THE POSSIBLE INFLUENCES OF PRE-EXPOSURE AND EROSION ON THE SCOTTISH SAMPLES	125
C.1 Pre-exposure	125
C.2 Erosion	127

<i>Appendix D</i>	
THE WYANGALA SAMPLES: SAMPLE LOCATIONS, WHOLE ROCK MEASUREMENTS AND DERIVED QUANTITIES	131
D.1 The Surface Samples	131
D.2 The Depth Profile	132
<i>Bibliography</i>	135

List of Figures

Figure 1.1	Potassium, calcium and chloride concentrations in samples that have been used to calibrate the production of ^{36}Cl from potassium [Zre91, Swa94, Phi96 and this work].	4
Figure 2.1	The surface accumulation of ^{36}Cl over time.	8
Figure 2.2	Schematic diagram showing a primary cosmic ray entering the Earth's atmosphere and triggering a cascade of reactions, producing secondary cosmic rays and possibly cosmogenic nuclides	12
Figure 2.3	Thermal neutron intensities as a function of depth in granite	31
Figure 2.4	Schematic comparison of Accelerator Mass Spectrometry to normal Mass Spectrometry.	38
Figure 3.1	Comparison of the results for the thermal neutron flux as a function of depth	47
Figure 3.2	Comparison of the thermal neutron flux with depth as calculated by Liu's model (given by labeled lines) and Dep's model (given by labeled symbols) for basalt, granite and carbonate rock. From Liu <i>et al.</i> , [Liu94].	49
Figure 3.3	Measured and predicted depth dependence of $^{36}\text{Cl}/\text{Cl}$ in quartz mineral separates.	51
Figure 3.4	Extent of glacial limits in Great Britain and Ireland.	53

Figure 3.5	The location of Wyangala.	56
Figure 4.1	Schematic diagram of the ANU 14UD tandem accelerator.	68
Figure 4.2	Schematic diagram of the heavy ion detector used for $^{36}\text{Cl}/\text{Cl}$ measurements at ANU.	70
Figure 4.3	The ungated spectra (a) and the gated spectra (b) of the Residual Energy vs Total Energy measured in the heavy ion detector.	71
Figure 4.4	Sample ML-1 was measured nine times by pyrohydrolysis, giving a range of values from 185 to 368 ppm.	73
Figure 4.5	Repeat isotope dilution measurements.	74
Figure 5.1	$\mathcal{P}_f(0)$ versus χ^2 for the eight Scottish quartz mineral separates.	79
Figure 6.1	Map of Western Scotland indicating the locations from which the samples were collected.	84
Figure 6.2	The χ^2 surface for $P_{\kappa,sp}(0)$ determined from 18 Scottish K-feldspar mineral separates.	87
Figure 7.1	Schematic diagram showing the positions of WYBACK and WYTOP relative to the main depth profile.	95
Figure 7.2	The steady state ^{36}Cl concentration produced by spallogenic thermal neutron capture on ^{35}Cl as a function of depth.	96
Figure 7.3	The erosion rate relative to the surrounding terrain. The erosion rate increases down the hill, as expected.	98
Figure 7.4	The measured ^{36}Cl concentration with depth. The error bars are the experimental uncertainty. Scatter in the profile is expected due to the variations in the chemical composition of the samples.	101
Figure 7.5	The χ^2 surfaces for Y_κ and ϵ .	103
Figure 7.6	Projections of the χ^2 surfaces for a) Y_κ and b) ϵ .	103
Figure 7.7	A breakdown of the ^{36}Cl concentrations in the Wyangala K-feldspar depth profile.	104
Figure 8.1	Summary of the ^{36}Cl production rates from potassium as a	114

function of depth at sea level and high latitude. . .

Figure C.1 The effects of erosion on the surface ^{36}Cl concentration, 128
normalised to surface ^{36}Cl concentration with zero erosion for
the K-feldspar mineral separate 95SCOT004.

Figure C.2 The effects of erosion on the surface ^{36}Cl concentration, 130
normalised to surface ^{36}Cl concentration with zero erosion for
the K-feldspar mineral separate 95SCOT068.

List of Tables

Table 2.1	Gross composition of cosmic rays.	13
Table 2.2	Terms used to describe neutron energies.	15
Table 2.3	The dominant ^{36}Cl production channels <i>in-situ</i> , in most rock types.	21
Table 2.4	Description of variables used in this work.	23
Table 2.5	The threshold energies for the major ^{36}Cl , ^{26}Al and ^{10}Be production channels.	26
Table 2.6	The atomic mass of isobars and molecules that can smother the ^{36}Cl peak during conventional mass spectrometry.	38
Table 3.1	Results of the previous three calibrations.	40
Table 3.2	Samples used by Phillips <i>et al.</i> to determine the ratios of the ^{36}Cl production [Phi96].	44
Table 3.3	Surface thermal neutron fluxes and ^{36}Cl production by neutron capture for different rock types and water content, calculated by the Monte Carlo method [Dep95].	48
Table 5.1	Measurements on Scottish Quartz Samples.	77
Table 5.2	Breakdown of the components making up the measured $^{36}\text{Cl}/\text{Cl}$ ratio.	79
Table 6.1	Composition of K-feldspar mineral separates.	85
Table 6.2	Breakdown of ^{36}Cl concentration by production channel in the Scottish K-feldspar samples.	86

Table 6.3	Comparison of the values determined for the ^{36}Cl production by spallation on potassium.	88
Table 6.4	The total ^{36}Cl production from neutron capture on potassium calculated using two different methods.	90
Table 7.1	Location and Correction factors of the Wyangala surface samples.	95
Table 7.2	Composition of the Wyangala surface K-feldspar mineral separates.	97
Table 7.3	The ^{36}Cl concentration measurements made on duplicate AgCl samples prepared from the same K-feldspar mineral separate.	97
Table 7.4	Breakdown of ^{36}Cl concentrations by production channel in the Wyangala surface samples.	98
Table 7.5	Erosion Rates of the Wyangala surface samples.	98
Table 7.6	Depths of Wyangala samples.	100
Table 7.7	K-feldspar mineral separate compositions for the Wyangala depth profile.	100
Table 7.8	Breakdown of the ^{36}Cl concentration by production channel in the Wyangala K-feldspar samples.	102
Table 7.10	The values for ϵ and Y_K that minimise the χ^2 for the scenarios that 0 cm, 20 cm and 40 cm of rock (or equivalent density of soil) was removed prior to the quarrying.	105
Table 7.11	Breakdown of the ^{36}Cl concentration by low-energy neutron capture.	106
Table 8.1	The results of this calibration, scaled to sea level and high latitude.	112
Table 8.2	Comparison of Production Rates determined in this study to those determined in previous work.	112
Table B.1	Location Parameters and Correction Factors for the Scottish Samples	121
Table B.2	Whole Rock Major Element Concentrations (%wt) for the	122

Scottish Samples

Table B.3	Whole Rock Trace Element Concentrations (ppm) for the Scottish Samples	122
Table B.4	Derived Quantities for Scottish K-feldspar Mineral Separates.	123
Table C.1	The thickness of material which would need to have been removed by the Loch Lomond Readvance to satisfy the condition of negligible pre-exposure.	126
Table D.1	Whole Rock Major Element Chemistry for the Wyangala surface samples (% wt).	131
Table D.2	Whole Rock Trace Element Concentrations for the Wyangala surface samples.	131
Table D.3	Derived Quantities for the Wyangala surface samples.	132
Table D.4	Whole Rock Major Element Chemistry for the Wyangala depth profile (% wt).	132
Table D.5	Whole Rock Trace Element Concentrations for the Wyangala depth profile.	133
Table D.6	Derived Quantities for Wyangala K-feldspar mineral separates.	133

Chapter One

INTRODUCTION

Geomorphic processes that add material are relatively easy to date. However, many geomorphical processes remove material, and geologists have struggled to place time constraints on them. In recent years cosmogenic nuclides produced *in-situ* (in the lithosphere) have shown great potential for improving this situation.

Cosmogenic nuclides are produced by secondary cosmic rays colliding with terrestrial nuclei. To be useful, the cosmogenic nuclei must have a low terrestrial background. This condition is usually met because: i) there is no terrestrial source of radiation (such as the decay of ^{238}U) with sufficient energy to produce a significant amount of them, and ii) the cosmogenic nuclei have either a negligible primordial concentration, or a sufficiently short half life that their initial concentration has decayed away.

Because cosmic rays are strongly absorbed in the atmosphere and lithosphere, *in-situ* production of cosmogenic nuclides takes place predominantly at the surface of the lithosphere. This makes cosmogenic nuclide accumulation, in effect, a surface exposure "clock" that can be used to put time constraints on destructive processes that leave nothing to be dated directly by traditional methods. When the surface of the lithosphere is static the "clock" runs at a rate determined by the half life of the cosmogenic nuclide, and the production rate *in-situ* of the cosmogenic nuclide. If the surface is being eroded, then the "clock" slows down in proportion to the erosion rate. If the surface is removed or replaced in a catastrophic event, such as a glacial retreat, land slide or lava flow, then the "clock" is reset and measures the exposure age of the new surface.

An accurate and comprehensive knowledge of production rates of cosmogenic nuclides is critical to the application of this relatively new dating tool.

This thesis is concerned with the complete *in-situ* production rate of one particular cosmogenic isotope, ^{36}Cl , produced from one particular target element, potassium. There have been several conflicting calibrations of this production rate. Scaling all measured values to sea level and high latitude, the earliest calibration was performed by Zreda *et al.* [Zre91] who obtained a value of $107 \pm 8 \text{ atom (gK)}^{-1} \text{ yr}^{-1}$. This value was revised to $154 \pm 10 \text{ atom (gK)}^{-1} \text{ yr}^{-1}$ in 1996 [Phi96]. In contrast, Swanson *et al.* [Swa94] determined the value to be $225 \pm 28 \text{ atom (gK)}^{-1} \text{ yr}^{-1}$.

The differences in these values may result from four problems with the methods employed by all the previous groups. Firstly, calcium and ^{35}Cl are also targets which could lead to the production of ^{36}Cl in the lithosphere. The previous researchers attempted to calibrate the production rates from all three target elements simultaneously by performing measurements on whole rock samples. For the majority of samples, ^{36}Cl production was dominated by contributions from calcium and/or ^{35}Cl , with a small contribution from potassium. Consequently, any errors in the calcium or ^{35}Cl production rates were magnified in the calculation of the potassium production rate.

The second area of concern is that the production of ^{36}Cl due to potassium was treated as a single value, whereas it is in fact the sum of three reaction channels: (i) spallation caused by fast neutrons, (ii) negative muon capture, and (iii) low-energy neutron capture. Because of the different physical properties of neutrons and muons, the fast neutron flux and the negative muon flux change with altitude at different rates*. To obtain the correct total production rate due to potassium at any altitude other than that of the original calibration samples, the production rate of each reaction channel must be determined separately so that it can be scaled appropriately.

Thirdly, to perform a well constrained calibration it is essential to select samples from surfaces of well known exposure age that have not been eroded or covered since their initial exposure. This is no simple task and generally restricts samples to those with an exposure age within the calibrated range of ^{14}C dating.

* Low-energy neutrons are predominantly produced by fast neutrons and muons, so their altitude dependence scales partially with fast neutrons and partially with muons.

The majority of the previous calibration samples were either from glacial moraines or young basalt lava flows, both of which have often proved difficult to date with conventional methods. Some of the original calibration measurements appear to have been based on sites where the geological history is poorly known, or where the preservation of surfaces cannot be guaranteed, or where the independently determined age of the sample is unreliable.

Finally, there are additional minor reaction channels that produce *in-situ* ^{36}Cl in the lithosphere, such as spallation of iron and titanium. These minor production channels are a source of systematic error as iron and titanium concentrations are typically a characteristic of a particular rock type, and each study tended to use whole rock samples of one particular type. Consequently, the results of the previous studies were internally consistent, and problems with the set of ^{36}Cl production rates were not apparent when they were applied to samples of a similar rock type. However, there is the possibility of significant error if these production rate values are applied to rock-types with a different composition to those of the original calibration samples.

This thesis is focussed on the complete ^{36}Cl production from potassium and represents the most complete calibration yet available. Measurements were made on pure K-feldspar mineral separates which virtually eliminated contributions from calcium, iron and titanium, and minimized the contributions due to chloride*. A comparison of the calibration samples used in this work with those used in the previous calibrations are shown in Figure 1.1. It should be noted that the scales are logarithmic, and, as can be seen, the higher K/Ca and K/Cl ratios in the present work are much more suitable for calibrating the complete production rate from potassium.

Samples were collected from bedrock surfaces and glacially transported boulders that were exposed by the end of the Loch Lomond Readvance glaciation in Scotland. This event has been studied in detail and is well defined in both age and location. In addition, a depth profile to 6 metres was measured in a granite quarry at Wyangala, Australia, to separate the negative muon capture production

* Chloride is often present in the fluid inclusions of the minerals and so to a large extent is an intrinsic characteristic of a rock outcrop. By obtaining pure K-feldspar mineral separates, however, the chloride content of a sample can be minimised by removing chloride in the fluid inclusions of other (K-poor) minerals.

rate from the spallogenic production rate. Precise chloride measurements (with a reproducibility of $\pm 1\%$) were made by isotope dilution mass spectrometry. This substantially reduced the uncertainty both in deriving the ^{36}Cl concentration from the $^{36}\text{Cl}/\text{Cl}$ ratio measured by Accelerator Mass Spectrometry (AMS), and in correcting for the ^{36}Cl which is produced from ^{35}Cl . In some samples with higher chloride concentrations, the ^{36}Cl contribution for low-energy neutron capture on ^{35}Cl was investigated by measuring the $^{36}\text{Cl}/\text{Cl}$ ratio in pure quartz mineral separates.

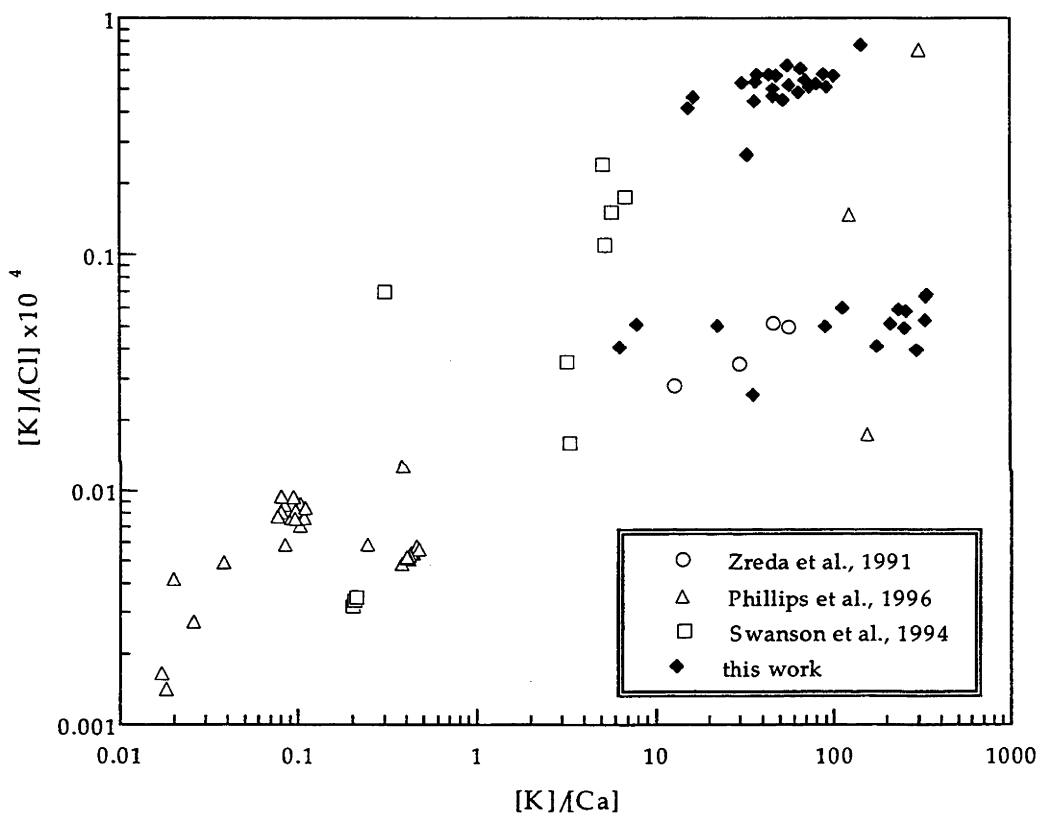


Figure 1.1 Potassium, calcium and chloride concentrations in samples that have been used to calibrate the production of ^{36}Cl from potassium [Zre91, Swa94, Phi96]. Samples used in this study fall into two groups differing primarily in chloride concentrations. Samples from the Wyangala granite have low chloride concentrations (21 ± 4 ppm). Samples of Torridon Sandstone from Scotland have chloride concentrations of 140 -275 ppm. An additional calibration sample used by Phillips *et al.* [Phi96] does not appear on the graph as its $[\text{K}]/[\text{Cl}]$ and $[\text{K}]/[\text{Ca}]$ ratios are too low.

During the course of this study samples were also measured from the Sierra Nevada, U.S.A., and Antarctica, preliminary results of which are given in Evans *et*

al. [Eva97]. These samples were not included in the final calibration as their exposure histories could not be sufficiently guaranteed. As a result they are only referred to in this dissertation where they were used to test a procedure that is relevant to this work.

The layout of this thesis is as follows. Chapter 2 gives an overview of how the measurement of cosmogenic nuclei concentrations can be applied to geological problems. It also discusses the production of cosmogenic nuclides, from cosmic ray fluxes, to the different nuclear reactions involved, and the actual production channels that produce ^{36}Cl from potassium.

Chapter 3 reviews the previous work that is relevant to this study, including earlier calibration attempts of ^{36}Cl from potassium, and recent studies on the low-energy neutron production at the air/ground boundary. Following this is an outline of the strategy used for this calibration.

The methodology and chemical procedures used in this work are described in Chapter 4.

Chapter 5 discusses the production rate of spallogenic secondary neutrons in the air above ground level, $\mathcal{P}_f(0)$ as determined from the Scottish quartz mineral separates. The surface production rate for ^{36}Cl from potassium spallation determined using the Scottish K-feldspar mineral separates is discussed in Chapter 6. The ^{36}Cl production rate from negative muon capture, as determined from the K-feldspar mineral separates from the granite depth profile, is discussed in Chapter 7, while Chapter 8 summarises of the results and presents the conclusions.

Chapter Two

COSMOGENIC NUCLIDE PRODUCTION *IN-SITU*

An overview of exposure age dating with cosmogenic nuclides produced *in-situ* is given in Section 2.1. This includes the equations that describe the accumulation of *in-situ* cosmogenic nuclides and shows how they can be used to obtain geological information such as exposure ages and erosion rates.

Calibration of the production rate of cosmogenic nuclides requires an understanding of the physics of cosmic rays, which initiate the whole process, and a basic understanding of the nuclear reactions that produce the cosmogenic nuclides. An overview of the relevant issues is given in Section 2.2.

The equations that describe each production channel for *in-situ* ^{36}Cl are given in Section 2.3, using examples of production from potassium.

Finally, any study of *in-situ* cosmogenic nuclides would not be possible if it weren't for the ultra sensitive measurement technique of Accelerator Mass Spectrometry. Section 2.4 gives an introduction into this unique method of counting nuclei and illustrates how it differs from, and the advantages it has over, conventional methods of measuring long lived radionuclide concentrations.

2.1 Overview of Exposure Age Dating

The basic principles of exposure age dating are the same for all cosmogenic radionuclides produced *in-situ* (for a discussion on stable cosmogenic nuclides see [Lal88]). For a static (non-eroding) surface, the rate of accumulation of a cosmogenic nuclide in a surface sample with an initial concentration of zero is:

$$\frac{dN}{dt} = P - \lambda N \quad (2.1)$$

where N is the cosmogenic nuclide concentration, P is the production rate at the sample location and λ is the decay constant (for ^{36}Cl , $\lambda = 2.303 \times 10^6 \text{ yr}^{-1}$). Solution of this gives the expression for concentration N , as a function of time:

$$N = \frac{P}{\lambda}(1 - e^{-\lambda t}) \quad (2.2)$$

where t is the exposure time.

Figure 2.1 shows the accumulation of a cosmogenic isotope in a static surface. It can be seen that during the initial period of nuclide growth, the cosmogenic nuclide concentration can give the length of time the sample has been exposed.

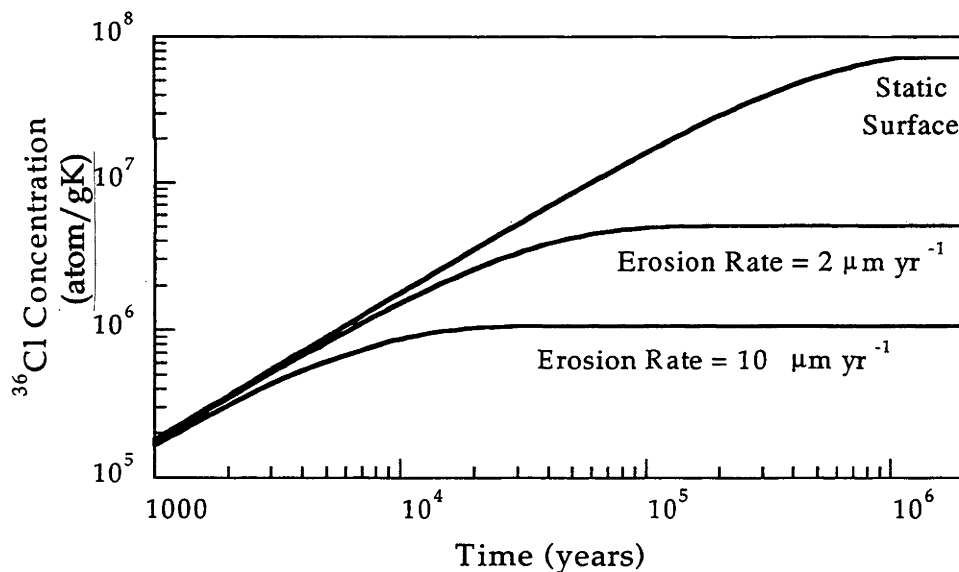


Figure 2.1 The surface accumulation of ^{36}Cl over time t , calculated using a production rate of $180 \text{ atom (g K)}^{-1} \text{ yr}^{-1}$ and assuming i) a static surface, ii) a constant erosion rate of $2 \mu\text{m yr}^{-1}$, and iii) a constant erosion rate of $10 \mu\text{m yr}^{-1}$. Prior to reaching steady state the ^{36}Cl concentration can be used to determine the exposure age of a static surface. As the erosion rate increases, the time required to reach steady state decreases, as does the steady state concentration. If the surface is known to be at steady state, the reduced ^{36}Cl concentration can be used to determine the erosion rate.

As the concentration increases, the number of decaying nuclei also increases to the point where the production and decay rates balance one another, and a steady state concentration is approached.

$$N \rightarrow \frac{P}{\lambda} \quad (2.3)$$

Near steady state, a measurable change in the concentration takes longer to achieve and so the uncertainty in the exposure age increases. The time it takes for a surface to reach steady state depends on the isotopic half life and its production rate*. Uncertainties in concentration measurements, the half life, and especially the ^{36}Cl production rate, set an upper limit on the use of exposure dating at ~3 lifetimes (~1 Ma), beyond which it would be difficult to distinguish a measured concentration from steady state.

The accumulation of cosmogenic nuclides at an eroding surface is reduced by the continuous movement of deeper, more heavily shielded material towards the surface. This material experiences a continually increasing production rate[†], and the surface is being refreshed with material that has a lower cosmogenic nuclide concentration. In a reference frame fixed to the surface, the differential equation which describes the accumulation of the nuclide with time at depth z (z increasing downwards), is:

$$\left. \frac{\partial N}{\partial t} \right|_z = P(z) - \lambda N(z) - \epsilon \left. \frac{\partial N}{\partial z} \right|_z \quad (2.4)$$

where ϵ is the erosion rate, $\partial z / \partial t$.

The three terms on the right hand side of the equation describe changes in the concentration with time. $P(z)$ is the production rate as a function of depth, the second term describes the loss of the cosmogenic nuclide due to radioactive decay, while the third term describes the rate at which surface material is replaced by underlying material with (typically) a lower concentration.

* There have been two measurements of the ^{36}Cl half life. The first measurement made in 1955 obtained the value $3.08 (0.03) \times 10^5$ yr [Bar55]. Goldstein measured the value in general use, $3.01 (0.02) \times 10^5$ yr, in 1966. [Gol66]

[†] except for low-energy neutron capture production rates near the surface, as discussed in §3.2

As a result of the additional loss of cosmogenic nuclides from erosion, it takes less time for the loss of cosmogenic nuclides (decay plus erosion) to balance the production of cosmogenic nuclides, and a steady state is approached more quickly. In addition, the steady state concentration is less than that for a static surface. Consequently, the steady state ^{36}Cl concentration can be used to measure the long term erosion rate (see Figure 2.1). However, unless the erosion rate has been constant for a long period of time, this may not correspond to the current erosion rate.

There are two common pitfalls in attempts to determine the exposure age of a surface. The first is to incorrectly assume that the initial cosmogenic nuclide concentration was negligible. If a young surface has been exposed by a shallow excavation there may be a significant initial cosmogenic concentration due to pre-exposure. This may be due to production by negative muon capture, or even from the tail of the spallation reactions, if the excavation was less than a few metres. If this isn't accounted for, then the "apparent exposure age" will be higher than the "actual exposure age". The second common pitfall is to assume a surface is static, when it is actually eroding. The effect this would have is to make the "apparent exposure age" lower than the "actual exposure age".

As the "apparent exposure age" can be greater than or less than the "actual exposure age", a cosmogenic isotope concentration by itself isn't sufficient to determine an upper or lower age limit, as is possible with many other dating techniques. Consequently, obtaining a reliable exposure age requires an understanding of the production mechanisms of cosmogenic isotopes so that during sample collection, suitable geomorphological information can be collected to provide supporting evidence of a minimum or maximum exposure age, for example, glacial striations which provide evidence of negligible erosion since the retreat of the glacier.

Besides additional geological and geomorphological information, there are two ways cosmogenic nuclides can be used to discriminate between the effects of age, erosion and pre-exposure:

1. Measurement of the concentrations of two or more cosmogenic nuclides with different half lives in the same sample [Nis91a, Liu94].

2. Measurement of the nuclide concentration at different depths, thus exploiting the different depth dependencies of each production mechanism [Sto94, Sto98, Dep95] (see §2.2 and §2.3).

In principle, measurement of several cosmogenic nuclides at several depths should allow for multiple variables to be determined so that complex exposure histories to be unraveled. In practice, the current uncertainties in the production rates, and in the measurement of most cosmogenic nuclide concentrations, are still too large to enable more than two variables to be determined.

2.2 Important Features of Cosmic Rays

There are two sources of the primary cosmic ray particles which continuously bombard the Earth's atmosphere. "Galactic" cosmic rays originate outside the solar system; "solar" cosmic rays originate from the Sun. Solar cosmic rays make up the major proportion of the primary cosmic ray flux, but their energies rarely exceed 100 MeV. The galactic cosmic ray flux is much lower, but consists of protons and nuclei with a much higher average energy. In fact, their energies extend far beyond those attainable in the laboratory.

As primary cosmic rays impact on the Earth's atmosphere they trigger a chain of nuclear reactions called a cascade (see Figure 2.2) that produces secondary particles, nuclides and photons [Lin76]. The cascade exhausts itself when the energy of the original primary cosmic ray is shared among the large number of secondaries. Therefore the depth of penetration of the cascade is dependent on the energy of the primary cosmic ray. The average galactic cosmic ray proton has several GeV in energy, and can induce a nuclear cascade which propagates down to sea level. Only occasional solar flares produce solar cosmic rays in the GeV range [She92]. Consequently solar cosmic ray cascades occur almost entirely in the top layers of the atmosphere and the production *in-situ* of cosmogenic nuclides is almost entirely due to the secondary products of galactic cosmic rays.

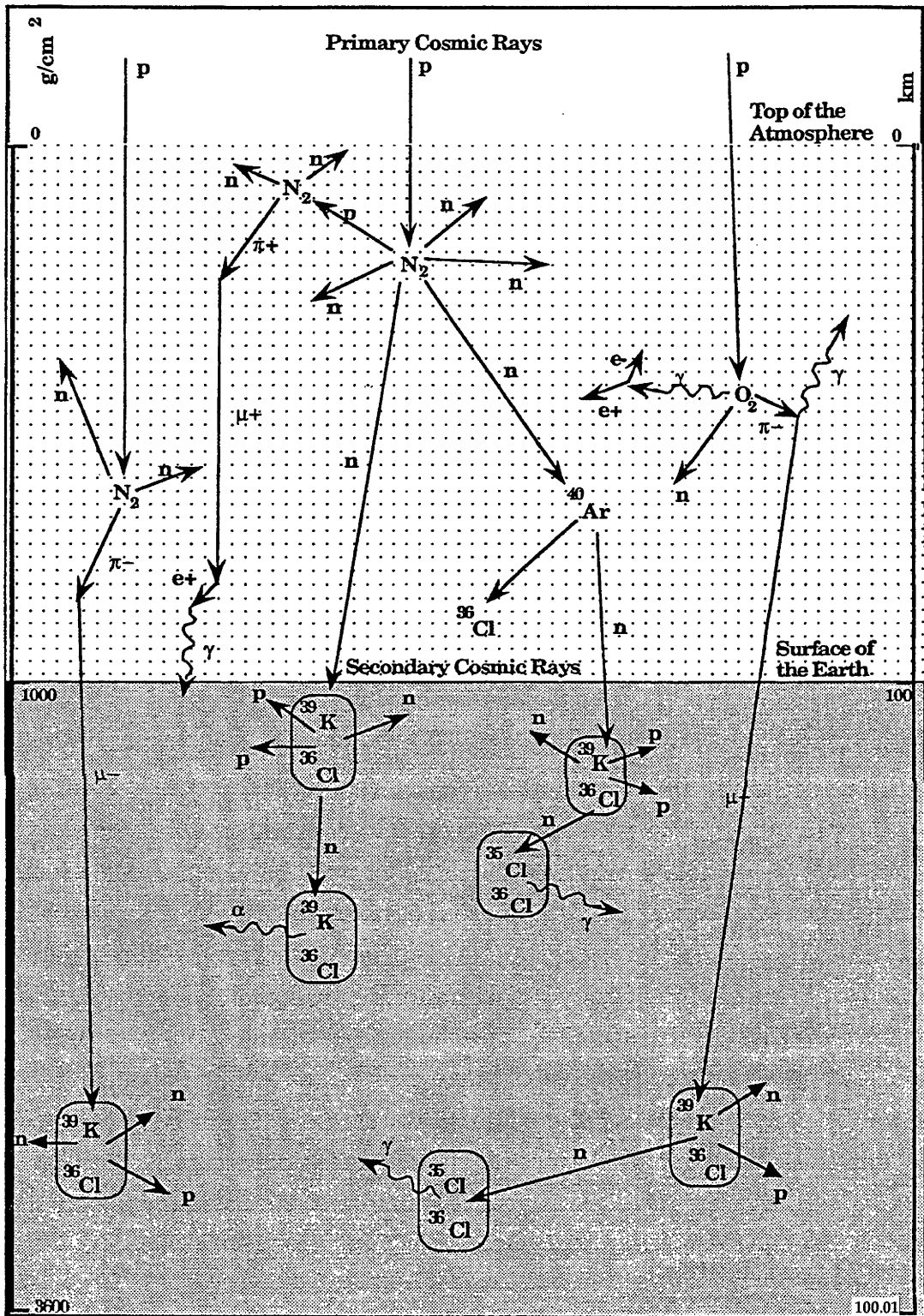


Figure 2.2 A schematic diagram showing a primary cosmic ray entering the Earth's atmosphere and triggering a cascade of reactions and producing secondary cosmic rays and possibly cosmogenic nuclides.

Table 2.1 shows the gross features of primary and secondary cosmic rays. Most notably, primary cosmic rays are composed chiefly of protons and α -particles, whereas the majority of secondary cosmic rays reaching the Earth's surface are chiefly electrons, photons, neutrons and muons (the composition and energies of secondary cosmic rays naturally vary with depth into the atmosphere and lithosphere).

Table 2.1 Gross composition of cosmic rays.

Cosmic ray type	Major Components	Typical Energies
Primary: Solar	98% protons	1 - 100 MeV
Primary: Galactic	87% protons, 12% α -particles	10 MeV – 20 GeV
Secondary	electrons, photons, muons	0 – 20 GeV
	neutrons	0 - 500 MeV

2.2.1 Temporal and Spatial Variation of Cosmic Rays

Any temporal or spatial variation in the cosmic ray flux will directly affect the production of cosmogenic nuclides. Scaling factors discussed below can be used to adjust the calibrated cosmogenic nuclei production rates to any location where a sample is collected.

The Earth's magnetic field allows only charged cosmic rays above a certain cut-off energy to enter the magnetosphere. However, this only affects the cosmic rays entering at latitudes less than 60° , as at higher latitudes the cut off energy is lower than that allowed through to the earth by the solar magnetic field. Consequently, the cosmogenic nuclei production rates must be scaled for samples collected below 60° latitude.

In addition, cosmic rays are attenuated as they pass through the atmosphere, so the production rate increases with altitude above sea level. Altitude and latitude scaling factors for spallation and spallogenic neutron production have been deduced by Lal and Peters [Lal67]. Altitude scaling for negative muon capture (for both the production of ^{36}Cl and muon-induced secondary neutrons) was calculated assuming an attenuation length of 247 g cm^{-2}

for the slow muon flux in the atmosphere [Con50; Win56], and for latitude assuming the same sea level variation as for neutrons [Lal67].

As neither the intensity nor the dipole axis orientation of the Earth's field is fixed, the cosmic ray flux varies with time at points on the Earth's surface below 60° latitude (due to the solar magnetic field cut-off described above). Measurements of past geomagnetic field strengths can be obtained from paleointensity records in lava and sediment cores, which can then be used to calculate the time-averaged field strength for a sample [Nis89, Cla95].

The secondary cosmic ray flux also varies with the angle at which the particles travel through the atmosphere. If a sample site were shielded from cosmic rays coming vertically to it, then the flux at the sample site would be much less than if the same area were shielded from the horizon. Incoming cosmic rays are believed to have a $(\sin\vartheta)^{2.3}$ angular dependence, with ϑ being taken from the horizon [Lal91]. Consequently, a correction is needed for any obstruction of greater thickness than a few metres that reduces the cosmic ray flux reaching the sample surface, and samples are normalised to a 2π exposure surface.

Because the cosmic rays continue to attenuate through the lithosphere, the thickness of the sample will effect the average production rate experienced by the whole sample. This is particularly true for surface samples as their production is dominated by spallation which decreases steeply with depth. Therefore a thickness correction is also applied to each sample.

2.2.2 Description of Important Cosmic Ray Induced Nuclear Reactions

For the purposes of this study cosmic rays can initiate four main nuclear reactions. These are:

1. spallation
2. negative muon capture
3. photonuclear reactions
4. low-energy neutron capture

These reactions are important for the production of significant cosmic ray secondaries, as well as the production of cosmogenic nuclides (which are, in effect, secondaries themselves). A brief description of each reaction is given below.

Since different energy ranges are important in many of the production channels considered in this work, use of non-quantitative terms, such as low/high and fast/slow energy, can be confusing and hence a definition of quantities is given in Table 2.2.

Table 2.2 Terms used to describe neutron energies.

Approximate Energy Range	Term used to describe the neutron ^a
≥ 50 MeV	Fast
≤ 100 keV	Slow
≤ 1 keV	Low-energy ^b
0.1 eV – 1 keV	Epithermal
≤ 0.1 eV	Thermal

^a All the neutrons can also be described as secondary.

^b Note that low-energy neutrons encompass both thermal and epithermal neutrons.

1. Spallation is a energetic inelastic nuclear reaction in which at least one of the two collision partners is a complex nucleus and the energy available well exceeds the binding energy between the nucleons* in the nucleus (approximately 8 MeV/nucleon) [She76].

A spallation reaction is described as occurring in two steps. In the first step, known as the intranuclear cascade or “knock-on step”, the particle enters the target. Because of the high energy of the particle, its wavelength is small enough that it becomes sensitive to the granular structure of the nucleus[†]. Consequently it interacts with some of the nucleons through a series of successive scatterings from individual nucleons. In doing so a few nucleons can be knocked out of the target nucleus. If the incident energy is ≥ 300 MeV, pions and K-mesons[‡] will be created and these may also be emitted from the nucleus. An incident nucleon with very high energy remains largely unaffected by the interaction, as it retains a large fraction of its energy and momentum [Sat90].

* The collective term for protons and neutrons, *i.e.* a constituent of an atomic nucleus.

[†] At 1 GeV a proton has a wavelength of about 0.12 fm (1 fm = 1×10^{-15} m). Comparatively, the nuclear radius has the dimensions of, $1.2 \times A^{1/3}$ fm, where A is the atomic number. For example, ³⁹K has a nuclear radius of ~4 fm.

[‡] Pions and K-mesons are elementary particles that can take part in strong interactions and that have an integral spin. If given a chance to decay spontaneously they will produce muons, however, deep in the atmosphere and in rock they almost always interact with other nuclei before this can occur.

The residual target is left in an excited state and in the second step it de-excites by evaporating γ -rays, a number of single nucleons, or small clusters of nucleons. This second stage is referred to as the “evaporation” or “slow” stage.

The spallogenic nucleons (neutrons, protons or α -particles emitted during either stage of the spallation reaction) can have a range of energies, from ~ 1 MeV up to the energy of the bombarding particle (≥ 50 MeV). The particles emitted in the first step, however, are more energetic and less isotropic (in the laboratory reference frame) than those emitted in the second step. In addition, the slower the incident nucleons, the more isotropic the emission of the spallogenic secondary nucleons.

Spallogenic secondary neutrons with sufficient energy may induce several more spallation reactions, while most spallogenic protons and α -particles will quickly come to rest as the result of ionisation losses [Lal67]. Consequently, successive steps in the cascade become progressively richer in neutrons until at ground level, about 90% of interactions producing cosmogenic nuclides are initiated by neutrons.

The spallation reaction is the dominant production mechanism of ^{36}Cl at the surface of the lithosphere in typical crustal rock compositions. It is also the main source of secondary neutrons in the top few meters of the lithosphere. Once the secondary neutrons have slowed down, they may take part in the slow neutron capture reaction discussed below. In addition, spallation reactions initiate the production of muons (mostly in the top 100 g cm^{-2} of the atmosphere). The pions and K-mesons that are emitted in the first stage of a spallation reaction can decay to produce negative and positive muons. These can then take part in negative muon capture reactions and photonuclear reactions, as discussed below.

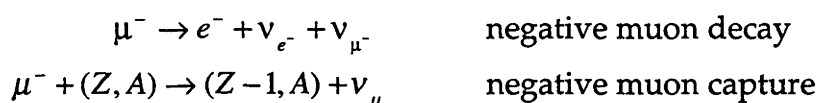
2. The second reaction mechanism is negative muon capture. Muons are unstable subatomic particles with a mass of $207 m_e$ and a charge of $\pm 1e$. As such, they behave like a heavy electron/positron. Muons are produced by the decay of pions and K-mesons at an average height of 15 km above the Earth's surface [Cha71].

* Lengths and depths in the Earth's atmosphere and lithosphere are given in the units g cm^{-2} so that they are independent of density. For example, a cosmic ray with 150 MeV energy will travel $\sim 50 \text{ g cm}^{-2}$ in both the atmosphere and the lithosphere. This is equivalent to ~ 420 m at the bottom of the atmosphere and ~ 20 cm in the lithosphere.

They have a meanlife* of 2.2 μ s when at rest, but can penetrate long distances into the Earth due to the absence of strong interactions and relativistic time dilation. The Coulomb force of the nucleus repels positive muons, and therefore only negative muons can be captured.

There are several steps in negative muon capture. The negative muon typically loses energy through collisions with electrons before being slowed sufficiently to be caught by an atom to form a μ -mesic atom.

The muon then cascades rapidly to the 1s level of the μ -mesic atom, where it may decay or be captured by the nucleus and combine with a proton to produce a neutron. As the muonic orbit radius in the 1s level of the atom is smaller than the electron orbit radius of the same quantum number by a factor of m_e/m_μ (1/207), the K-orbit may be entirely within the nucleus in a heavy atom, which increases the opportunity for the muon and proton to combine.



In the latter case, a large part of the 107 MeV liberated is carried off by the neutrino, and the nucleus is left with an average excitation energy of 15 MeV. The nucleus may then de-excite by emitting neutrons and/or protons and/or α -particles. The emission of protons or α -particles, however, is much less likely (typically 2% of the time for protons, and 0.5% of the time for α -particles [Cha71]) as the Coulomb barrier of the nucleus impedes the escape of charged particles.

The negative muon capture reaction is important in this study not only as a production mechanism for ^{36}Cl from negative muon capture on ^{39}K , but as an additional source of secondary neutrons from negative muon capture on all the constituents of the rock samples.

3. The third reaction is the production of secondary neutrons by photonuclear reactions which are initiated by bremsstrahlung, which is produced by the rapid

* Meanlife or lifetime is different from half life: meanlife ($= 1/\lambda$, where λ is the decay constant) is the average time an elementary particle (in a given medium) or radionuclide exists. A half life ($= \ln 2/\lambda$) is the amount of time which it takes for one half of a number of radioactive nuclei to decay.

deacceleration, or “braking”, of high energy, positive and negative, muons* during a close approach to a nucleus. The energy lost at these encounters is radiated as a single photon and the radiative loss increases rapidly with the energy of the muon.

The photonuclear reaction occurs when the high energy photon is absorbed by another nucleus. This can cause either the emission of nucleons similar to the evaporation stage of the spallation reaction, or fission in heavy nuclides. The significance of this reaction is as a third source of secondary neutrons (the direct production of ^{36}Cl from ^{39}K via $^{39}\text{K}(\gamma, n2p)^\dagger$ being negligible). This reaction has a low neutron yield and is a minor source of low-energy neutrons at the surface compared to spallogenic and mu-genic secondaries, but because it decreases more slowly with depth, it becomes more important below ~ 3 m in the lithosphere.

4. The final reaction is slow neutron capture, which is comprehensively described in Gladstone [Gla55]. The slow neutrons are captured by the nucleus in two distinct stages: first, the neutron is absorbed by the target nucleus to form a compound nucleus that is in an excited state. The excited compound nucleus then quickly undergoes the second stage of the reaction, involving either the emission of a γ -ray, α -particle or proton ‡ , or it is broken up into two more or less equal parts, i.e. it fissions. Of these reactions the (n, γ) reaction is the most common, for it occurs with a wide variety of elements. The reactions that are accompanied by the emission of a charged particle, the (n, α) and (n, p) reactions, can only occur if there is sufficient energy to overcome the Coulomb potential in addition to detaching the particle from the nucleus. As a result these reactions are generally limited to isotopes of low proton number. On the other hand, the (n, f) reaction is generally restricted to a few isotopes of high mass number.

The likelihood of a nucleus taking part in a slow neutron capture reaction is expressed by its cross section, which is depicted as the effective area the nucleus

* Electrons also produce bremsstrahlung, but are not the principal source of high energy, cosmic ray induced bremsstrahlung in the lithosphere.

† Nuclear reactions are often represented by enclosing within brackets the symbols for the incoming or outgoing particles or quanta, with the initial and final nuclides being shown outside the brackets. For example $^{35}\text{Cl}(n, \gamma)^{36}\text{Cl}$ represents the reaction $^{35}\text{Cl} + n \rightarrow ^{36}\text{Cl} + \gamma$. This can be shortened to (n, γ) when discussing the type of reaction, rather than a specific reaction.

‡ In the case where a neutron is emitted, the reaction is called a scattering reaction *i.e.* the neutron interacts with, and transfers some or all of its energy to the nucleus, but the neutron remains free in the process.

represents to the slow neutron, typically measured in barns^{*}. The slow neutron capture cross section not only depends on the neutron energy, but varies from one isotope to another isotope of the same element, and changes with the nature of the reaction. In many instances, however, this is simplified by the fact that one reaction predominates, and/or one particular isotope has a much larger cross section than the other isotopes of the same element.

The macroscopic cross section of a bulk material consisting of a mixture of different isotopes can be determined by summing the individual reaction cross sections, each weighted by the abundance of the target nuclei in the material. There are several isotopes that have notably high cross sections, such as ¹⁰B, ^{155,157}Gd and ¹⁴⁹Sm. These isotopes can greatly influence the macroscopic cross section of a rock sample even though their relative concentrations are very low in most common rock types.

For many elements (particularly those with mass number greater than 100) the capture cross section exhibits different characteristics in three different energy regions.

The lowest energy region, ≤ 0.1 eV, is where the neutrons are in thermal equilibrium with their environments. The cross section decreases steadily with increasing neutron energy. As the capture cross section varies inversely with the neutron velocity, thermal neutron capture is said to obey the $1/v$ law. Although the thermal neutrons have a range of energies, they obey the Maxwell-Boltzmann distribution law, so that a unique temperature-dependent energy can be assumed. At 20°C, for example, the mean energy of a thermal neutron is ~ 0.025 eV.

At neutron energies between 0.1 eV and 1 keV there is an epithermal or resonance region. This region is characterized by the occurrence of peaks, or resonances, where the capture cross section rises fairly sharply to high values for certain neutron energies and then falls again. Resonances occur when the energy of the slow neutron is equal to one of the quantum states of the nucleus. Some isotopes have only one resonance peak, while others have two or more.

Beyond the resonance region the nuclear cross sections decrease rapidly with increasing neutron energy. For energies of the order of 0.1 MeV or more, the

* The symbol for barns is b: $1 \text{ b} = 10^{-28} \text{ m}^2 = 100 \text{ fm}^2$

capture cross sections decrease until they are similar in magnitude to the geometrical cross section.

Since the cross sections for this reaction are largest in the thermal and epithermal region, production of ^{36}Cl due to capture of neutrons at higher energies will be neglected and only low-energy (thermal and epithermal) neutron capture will be considered.

Chlorine-35 has a high thermal neutron capture cross section and dilute resonance integral* for the (n, γ) reaction of 43.6 barns and 17 barns respectively. Consequently this is a major production mechanism of ^{36}Cl wherever chloride is present.

2.3 In-Situ Production Channels for ^{36}Cl

Cosmogenic nuclides are produced in both the atmosphere and uppermost lithosphere, and as a result they are divided into two categories according to their production location. Cosmogenic nuclides produced in the lithosphere are referred to as being "produced *in-situ*". Meteoric (or "garden-variety") cosmogenic nuclides are produced in the atmosphere and then dispersed through near surface reservoirs†.

The cosmogenic nuclides produced *in-situ* that are most commonly used for geomorphic studies are ^{36}Cl , ^{10}Be and ^{26}Al . Chlorine-36 has a half life of 301 kyr and is produced in K-rich or Ca-rich minerals such as K-feldspar and calcite [Zre91, Swa94, Phi96, Eva97, Sto97, Sto98]. Beryllium-10 and ^{26}Al have half lives of 1.5 Myr and 705 kyr, respectively. Both ^{10}Be and ^{26}Al are produced in quartz and other silicates [Lal91, Nis89].

* The dilute resonance integral is the integrated cross section over the resonance, or epithermal, energy range:

$$\int_{E_2}^{E_1} \sigma(E) dE, \text{ where } E_1 \text{ and } E_2 \text{ are the upper and lower limits of the resonance energy region. The term}$$

"dilute" refers to the fact that this parameter is only applicable to an infinitely dilute mixture of neutron absorbers and moderators, so that the medium through which the neutrons travel does not significantly modify the neutron-energy spectrum, an effect known as flux depression. This condition is met in most geochemical environments (Fab88).

† The most well known meteoric cosmogenic nuclide is ^{14}C , which is produced by $^{14}\text{N}(n,p)^{14}\text{C}$, and then mixes throughout the atmosphere and is taken up by living organisms. When the organism dies it stops taking up ^{14}C and the concentration begins to decrease due to decay, which is the basis of ^{14}C dating.

Some nuclides, such as ^{36}Cl and ^{10}Be , have both meteoric and *in-situ* components. Meteoric ^{36}Cl is produced by spallation of argon, and meteoric ^{10}Be is produced by spallation of oxygen and nitrogen. Others, such as ^{26}Al , only have an *in-situ* component as there is no suitable target nucleus in the atmosphere.

Meteoritic production rates are much higher than *in-situ* production rates due to the greater intensity of the cosmic ray flux in the atmosphere. For example, argon makes up ~1% of the atmosphere, compared to ~11% potassium in K-feldspars, but the amount of ^{36}Cl produced in the atmosphere is 2 orders of magnitude larger than in K-feldspar at the Earth's surface. Therefore, meteoric ^{36}Cl must be removed from a rock sample before an *in-situ* ^{36}Cl measurement is possible. Fortunately, due to the hydrophilic nature of chloride, it is not strongly retained by mineral surfaces, and tends to migrate into ground water, whereas the *in-situ* ^{36}Cl remains captured in the mineral lattice.

There are several production channels in the lithosphere which result in the production of ^{36}Cl . The most important of these are given in Table 2.3:

Table 2.3 The dominant ^{36}Cl production channels *in-situ* in most rock types.

Spallation	Negative Muon Capture	Low-energy Neutron Capture
$^{39}\text{K}(n, 2p2n)^{36}\text{Cl}$	$^{39}\text{K}(\mu, p2n)^{36}\text{Cl}$	$^{39}\text{K}(n, \alpha)^{36}\text{Cl}$
$^{40}\text{Ca}(n, 3p2n)^{36}\text{Cl}$	$^{40}\text{Ca}(\mu, 2p2n)^{36}\text{Cl}$	$^{35}\text{Cl}(n, \gamma)^{36}\text{Cl}$

In this work there is no distinction between $(n,2p2n)$ and (n,α) production channels (for example), as only the abundance of the target and product nuclei can be measured. In addition, a simplification has been made in only expressing the spallation and negative muon capture production channels involving ^{39}K and ^{40}Ca . There is a small ^{36}Cl contribution from other less-abundant calcium and potassium isotopes, but as ^{39}K and ^{40}Ca have an isotopic abundance of 93.3% and 96.9% respectively, these are by far the dominant production channels. In contrast, the low-energy neutron capture on ^{35}Cl and ^{39}K production channels are isotope specific. The $^{37}\text{Cl}(n,2n)^{36}\text{Cl}$ and $^{41}\text{K}(n,\alpha 2n)^{36}\text{Cl}$ reactions have a negative Q-value*, and therefore cannot be initiated by low-energy neutrons.

* The amount of energy produced in a nuclear reaction. A negative Q-value means that energy is required for a reaction to occur.

There are a few other less significant production channels for the production *in-situ* of ^{36}Cl , mainly from the spallation of iron and titanium. These have much smaller production rates per target nucleus [Fab88] and can be discounted altogether in this work, as the iron and titanium concentrations in K-feldspar are negligible.

The total production rate *in-situ* of ^{36}Cl is the sum of the production rates for each production channel at a specific depth.

$$P_{total}(z) = P_{sp}(z) + P_{\mu^-}(z) + P_n(z) \quad (2.5)$$

where sp , μ , and n denote production due to spallation, negative muon capture and low-energy neutron capture, respectively. Each of the individual production channels can be expressed as a function of several components, as described for the potassium production channels below.

Table 2.4 gives a summary of all the symbols used in this and subsequent chapters to describe the production and accumulation of ^{36}Cl .

Table 2.4 Description of variables used in this work.

Symbol	Description	Value, Range and/or Units	Notes	Reference
General Symbols				
z	depth	g cm^{-2}		
ρ	density	2.643 g cm^{-3}	(1)	Measured
		2.65 g cm^{-3}	(2)	
ϵ	Erosion rate at the top of the depth profile	$\mu\text{m yr}^{-1}$		
λ	^{36}Cl decay constant	$2.303 \times 10^6 \text{ yr}^{-1}$		
$t_{1/2}$	^{36}Cl half life	$3.01 \times 10^5 \text{ yr}$		[Gol66]
P	^{36}Cl production rate	$\text{atom g}^{-1} \text{ yr}^{-1}$		
N	^{36}Cl concentration	atom g^{-1}		
N_{meas}	Measured ^{36}Cl concentration	atom g^{-1}		
σ_{meas}	± 1 std deviation uncertainty of measured ^{36}Cl concentration	atom g^{-1}		
A_a	Average atomic mass of air	14.5 g mol^{-1}		[Liu94]
A_s	Average atomic mass of rock			
P_K	Total ^{36}Cl production rate due to potassium	$\text{atom (gK)}^{-1} \text{ yr}^{-1}$		
P_{Ca}	Total ^{36}Cl production rate due to calcium	$\text{atom (gCa)}^{-1} \text{ yr}^{-1}$		
^{36}Cl produced by spallation				
$P_{\text{sp,K}}(z)$	^{36}Cl production rate due to spallation on potassium	$\text{atom (gK)}^{-1} \text{ yr}^{-1}$		
$P_{\text{sp,Ca}}(0)$	Surface ^{36}Cl production rate due to Ca	$48.8 \pm 3.4 \text{ atom (gCa)}^{-1} \text{ yr}^{-1}$	(3)	[Sto97]
Λ_{sp}	Effective attenuation length for spallation production	160 g cm^{-2}		Assumed value (cf. Nis94)]
^{36}Cl produced by negative muon capture				
$P_{\mu}(z)$	^{36}Cl production rate by negative muon capture	$\text{atom g}^{-1} \text{ yr}^{-1}$		
$P_{\mu,\text{Ca}}(0)$	^{36}Cl production rate by negative muon capture on Ca at the surface	$5.3 \pm 1.1 \text{ atom (gCa)}^{-1} \text{ yr}^{-1}$	(3)	[Sto98]
$\Psi_{\mu}(z)$	Intensity of negative muons stopping at depth z	stopped $\mu \text{ g}^{-1} \text{ yr}^{-1}$		[Sto98] and Refs. therein
Y_K	^{36}Cl yield per stopped μ in K-feldspar	atom per stopped μ		
f_c	Chemical compound factor (fraction of negative muons reaching the 1s muonic level of the target atom)			
f_i	Isotopic abundance of ^{39}K or ^{40}Ca	93.3% for ^{39}K , 96.6% for ^{40}Ca		
f_d	Fraction of nuclear captures from 1s muonic level			
$f_{p,2n}$	Probability of emission channel required to produce ^{36}Cl (for potassium this is a p2n emission channel and for calcium this is an α or 2p2n emission channel)			
^{36}Cl produced by low-energy neutrons				
$P_n(z)$	^{36}Cl production rate from low-energy neutrons	$\text{atom g}^{-1} \text{ yr}^{-1}$		
σ_{35}	Thermal neutron capture cross section of ^{35}Cl	436 barns		
σ_{39}	Thermal neutron capture cross section of ^{39}K	4.3 millibarns		
f_{35}	Fraction of thermal neutrons captured by ^{35}Cl	0.00133 – 0.00229	(1)	
		0.00141 – 0.0274	(2)	
f_{39}	Fraction of thermal neutrons captured by ^{39}K	0.00086 – 0.00118	(1)	
		0.00041 – 0.00138	(2)	
$P_r(0)$	Production rate of spallogenic secondary neutrons in air above ground level. Equivalent to $P_r(0)$ in [Liu94]			
Ψ_n	^{36}Cl production rate by thermal neutron capture rate on ^{36}Cl	$\text{atom g}^{-1} \text{ yr}^{-1}$		Notation used by [Zre91, Swa94].
Φ_n	Thermal neutron production rate at sea level and high latitude	$\text{neutrons Kg}^{-1} \text{ yr}^{-1}$		Not terms used in this work.
^{36}Cl produced by spallogenic thermal neutron capture				
$P_{n,\text{sp-th}}$	Thermal neutron production from spallation reaction	$\text{neutrons g}^{-1} \text{ yr}^{-1}$		
k_1	Pre-exponential term describing production of spallogenic thermal neutrons in rock. Equals $\phi_{\text{ss}}^* \Sigma_{\text{th,ss}}$ / $P_r(0)$ in notation of [Liu94]	0.001907 – 0.001933	(1)	[Liu94]
		0.001810 – 0.001929	(2)	
k_2	Pre-exponential term related to loss of albedo neutrons. Equals $F\Delta\phi_{\text{ss}}^* \Sigma_{\text{th,ss}}$ / $P_r(0)$ in notation of [Liu94]	-0.001178 – -0.001262	(1)	[Liu94]
		-0.001092 – -0.001339	(2)	
L_{th}	Characteristic length for thermal neutron diffusion.	21.05 – 23.44	(1)	[Liu94]
		18.922 – 26.337	(2)	

Table 2.4 continued

Symbol	Description	Value, Range and/or Units	Notes	Reference
$\Delta\phi_{\infty}$	Difference between the thermal neutron fluxes in the air and the ground at the land surface elevation that would be observed in the absence of an interface.			[Liu94]
$\Sigma_{n,\infty}$	Macroscopic thermal neutron capture cross section for a rock	0.00580 – 0.00755 0.00445 – 0.00895	(1) (2)	[Liu94]
F	Weighting factor that determines the balances of the end members in the actual interface fluxes			[Liu94]
³⁶Cl produced by spallogenic epithermal neutron capture				
$P_{n,sp-epi}$	Epithermal neutron production from spallation reactions	neutrons g ⁻¹ yr ⁻¹		
I_{35}	Dilute resonance integral for epithermal neutron absorption of ³⁵ Cl	17 ± 2 barns		
I_{39}	Dilute resonance integral for epithermal neutron absorption of ³⁹ K	~1.9 millibarns		
$f_{epi,35}$	Fraction of subsurface epithermal neutrons absorbed by ³⁵ Cl	0.00142 – 0.00220 0.00164 – 0.0232	(1) (2)	
$f_{epi,39}$	Fraction of subsurface epithermal neutrons absorbed by ³⁹ K	0.00095 – 0.00123 0.00054 – 0.00127	(1) (2)	
k_3	Pre-exposure term describing production of spallogenic epithermal neutrons in rock.	0.1271 – 0.1456 0.1129 – 0.1787	(1) (2)	
k_4	Pre-exponential term related to loss of albedo neutrons.	0.05084 – 0.05824 0.04516 – 0.07148	(1) (2)	
L_{epi}	Characteristic length for epithermal diffusion in a particular rock type	32.09 – 34.91 29.441 – 36.648	(1) (2)	
$p(E_{th,\infty})$	Resonance escape probability for epithermal neutrons in the rock.			
F_{epi}	Fractional reduction (relative to an infinite rock medium) in the epithermal neutron flux at the atmosphere/rock interface	assigned a value of 0.4 based on Monte Carlo simulations		[Phi95]
Neutrons produced following negative muon capture				
$P_{n,\mu}(z)$	Thermal neutron production from negative muon capture reaction	neutrons g ⁻¹ yr ⁻¹		
Y_{μ}	Average neutron yield from muon capture	0.5 neutrons per stopped μ		
Neutrons produced by photodisintegration reactions				
$P_{n,\mu f}$	Thermal neutron production from muon-induced photoneutron reactions	neutrons g ⁻¹ yr ⁻¹		
$\Phi_{\mu f}(z)$	Fast muon flux at depth z	muons cm ⁻² yr ⁻¹		[Sto98]
Y_f	Average neutron yield per photodisintegration	1 neutron disintegration ⁻¹		[Wyk65]
$k_3 \ln(z/k_6)$	Accounts for the energy lost by the total muon flux at depth z.	$7.75 \times 10^{-6} \ln(0.1065 z)$	(1)	
Neutron produced by U fission and (α,n) reactions				
$P_{n,U+Th}$	Thermal neutrons produced by radioactive decay of U and Th	neutrons g ⁻¹ yr ⁻¹		
P_{α}	Production rate of thermal neutrons by (α,n) reactions	neutrons g ⁻¹ yr ⁻¹		
P_f	Production rate of thermal neutrons by U fission	neutrons g ⁻¹ yr ⁻¹		
S_i	Mass stopping power of element i for α-particles	MeV g ⁻¹ cm ²		[Van73]
F_i	Fractional abundance of element i	ppm		
$Y_n(U)$	Neutron yield of element i per ppm U	neutrons g ⁻¹ yr ⁻¹ (ppm U) ⁻¹		[Van73]
$Y_n(Th)$	Neutron yield of element i per ppm Th	neutrons g ⁻¹ yr ⁻¹ (ppm Th) ⁻¹		[Van73]
N_{238}	Atomic concentration of ²³⁸ U in the sample	atom g ⁻¹		
λ_{238}	Decay constant for ²³⁸ U	1.5513×10^{10} yr ⁻¹		[Van73]
Γ_{238}	Branching ratio for spontaneous fission	5.45×10^{-7}		[Van73]
ν_n	Number of neutrons emitted per spontaneous fission of ²³⁸ U	2.00 (0.03)		[Van73]

- (1) Wyangala samples or mineral separates
 (2) Scottish samples or mineral separates
 (3) At sea level and high latitude

2.3.1 Production due to Spallation

The fast neutron flux decreases exponentially in the lithosphere with an attenuation length, Λ_{sp} of $\sim 160 \text{ g cm}^{-2}$. Therefore, the cosmogenic production due to spallation from potassium can be expressed by the equation:

$$P_{sp,K}(z) = P_{sp,K}(0)[K] e^{\frac{-z}{\Lambda_{sp}}} \quad (2.6)$$

where $P_{sp,K}(0)$ is the surface spallation production rate ($\text{atom (gK)}^{-1} \text{ yr}^{-1}$) due to potassium, $[K]$ is the potassium concentration (%wt), and z is depth in the lithosphere (g cm^{-2}).

An expression analogous to Equation 2.6 can be used to describe the spallation production for calcium. In the K-feldspar samples used for this study, $P_{sp,Ca}(0)$ is typically $\ll 1\%$ or less of the total spallation production. The value of $P_{sp,Ca}(0)$ used to make this small correction is $48.8 \pm 3.4 \text{ atom (gCa)}^{-1} \text{ yr}^{-1}$ at sea level and high latitude [Sto96].

Recent models of secondary cosmic ray transportation through the atmosphere and lithosphere predict that some of the fast neutrons produced in the lithosphere are lost into the air due to the different transport properties of the air and ground [Mas95]. This would mean that the spallation depth dependence was not exponential near the surface (as in Equation 2.6), but was approximately constant for the first $\sim 20 \text{ g cm}^{-2}$. Corrections to this work of about 5% (depending on sample thickness) may be required at a later date if this effect is confirmed experimentally. At this point, however, an exponential attenuation from the surface will be assumed. Little error would be introduced to the exposure age measurement of an "unknown" sample, so long as the same thickness corrections were used and the sample was roughly the same thickness ($\sim 5\text{cm}$) as the calibration samples.

It is interesting to note, however, that of all the major production channels producing *in-situ* ^{26}Al , ^{10}Be and ^{36}Cl , the spallogenic production of ^{36}Cl from ^{39}K , an (n, α) reaction, would be the most sensitive to this effect as it has the lowest threshold energy (see Table 2.5). The low threshold energy is important because the lower the incident neutron energy, the more isotropic the spallogenic neutrons (see § 2.2.2), so more are likely to be emitted back out of the surface. This is

especially significant as the major contribution to isotope production comes from the part of the nucleon energy spectrum within ~10 MeV above the threshold value for the particular reaction [Lal67]. Consequently, the ^{36}Cl production in the top 20 g cm⁻² would be expected to be flatter than the ^{26}Al or ^{10}Be production rates in the same depth interval.

Table 2.5 The threshold energies for the major ^{36}Cl , ^{26}Al and ^{10}Be production channels. The $^{39}\text{K}(n,\alpha)^{36}\text{Cl}$ reaction channel has by far the lowest threshold energy.

^{36}Cl Spallogenic Production		^{26}Al Spallogenic Production		^{10}Be Spallogenic Production	
Reaction Channel	Threshold Energy	Reaction Channel	Threshold Energy	Reaction Channel	Threshold Energy
$^{39}\text{K}(n,\alpha)^{36}\text{Cl}$	1.36 MeV	$^{28}\text{Si}(n,p2n)^{26}\text{Al}$	24.76 MeV	$^{16}\text{O}(n,4p3n)^{10}\text{Be}$	63.1 MeV
$^{39}\text{K}(n,2p2n)^{36}\text{Cl}$	27.1 MeV			$^{16}\text{O}(n,\alpha2pn)^{10}\text{Be}$	34.6 MeV
$^{40}\text{Ca}(n,\alpha p)^{36}\text{Cl}$	7.1 MeV			$^{12}\text{C}(n,2pn)^{10}\text{Be}$	27.4 MeV
$^{40}\text{Ca}(n,3p2n)^{36}\text{Cl}$	35.6 MeV				

(Isotopic abundances are 93.3% for ^{39}K , 96.9% for ^{40}Ca , 92.2% for ^{28}Si , 99.8% for ^{16}O and 98.9% for ^{12}C).

2.3.2 Production due to Negative Muon Capture

Muons are weakly interacting particles and therefore the muon flux decreases much more slowly with depth than the fast neutrons flux. This leads to three important consequences:

1. Isotope production by negative muons increases less steeply with altitude than production by spallation. Thus, the total isotope production rate cannot be correctly scaled from one location to another unless the relative balance of production by spallation and negative muon capture is known.
2. While the surface negative muon production rate is a small portion of the total surface production rate, it is the dominant production mechanism between depths of a few metres and a few tens of meters in the lithosphere. At shallower depths, spallation is generally the dominant production mode, and at greater depths radiogenic and fast-muon-induced reactions become more important.
3. As the negative muon capture production rate diminishes less steeply with depth than spallation, changes to the surface, such as erosion or burial, will

affect the muon capture component of the ^{36}Cl concentration much less dramatically than the spallogenic component at a given depth.

Negative muon capture is, therefore, an important production mechanism not only for deep samples, but also for surface samples with high erosion rates and young surface samples that have been exposed by shallow excavation.

The negative muon capture reaction is described in Section 2.2.2. The production rate of ^{36}Cl by negative muon capture on potassium is given by the equation:

$$P_{\mu^-,K}(z) = \Psi_{\mu^-}(z) f_c f_i f_d f_{p,2n} \quad \text{atom g}^{-1} \text{yr}^{-1} \quad (2.7a)$$

$$= \Psi_{\mu^-}(z) Y_K \quad (2.7b)$$

where $\Psi_{\mu^-}(z)$ is the negative muon stopping rate as a function of depth, z ,

f_c is the compound factor, which is the fraction of negative muons stopped in K-feldspar that reach the 1s level of a potassium atom, as opposed to silicon, aluminium or oxygen atoms,

f_i is the isotopic abundance of ^{39}K ,

f_d is the fraction of negative muons which, having reached the 1s level of the atom, are captured by the nucleus rather than decaying in orbit,

$f_{p,2n}$ is the probability of the exit channel in which a proton and two neutrons are emitted to produce a ^{36}Cl nucleus, and

Y_K is the yield of ^{36}Cl per stopped negative muon in K-feldspar.

The negative muon stopping rate at sea level and high latitude, $\Psi_{\mu^-}(z)$, has been evaluated by Stone *et al.* [Sto98] at depths from 100 g cm^{-2} to 5500 g cm^{-2} using range spectra of muons incident at the Earth's surface that were measured largely in the 1950s and early 60s (see references in [Sto98]) and is given by the expression:

$$\log(\Psi_{\mu^-}(z)) = a + b \log_{10}(z) + c(\log_{10}(z))^2 + d(\log_{10}(z))^3 + e(\log_{10}(z))^4 + f(\log_{10}(z))^5 \quad (2.8)$$

where $a = 1.586$, $b = 1.709$, $c = -1.817$, $d = 1.185$, $e = -0.9642$, $f = 0.01955$.

In this work the value of $Y_K (= f_i f_d f_c f_{p2n})$ is the unknown being determined. This is because amongst its four component factors only f_i and f_d are well constrained experimentally. However, it must be appreciated that incorporated into the value of Y_K is the compound factor, f_c , which is dependent on the mineral composition in which the target atom is held. Therefore, the value of Y_K obtained in this work is specific to K-feldspar and an additional uncertainty will be involved when applying this value to another K-bearing rock or mineral.

The value of the ^{36}Cl production rate for negative muon capture on calcium that was used to apply minor corrections in this work was $5.3 \text{ atom (gCa)}^{-1} \text{ yr}^{-1}$ at sea level and high latitude [Sto98]. As the correction is small, the additional uncertainty of applying the value obtained from calcite to K-feldspar will have a minimal effect on the uncertainty in the value of Y_K determined in this work.

2.3.3 Production due to Low-Energy Neutron Capture

Chlorine-36 is produced by low-energy (thermal and epithermal) neutron capture on both ^{35}Cl and ^{39}K . The cross section for the $^{35}\text{Cl}(n,\gamma)^{36}\text{Cl}$ reaction for thermal neutrons is 43 ± 2 barns, and the dilute resonance integral is 17 ± 2 barns, therefore the production rate of ^{36}Cl due to low-energy neutron capture on ^{35}Cl is substantial wherever chloride is present.

On the other hand, the thermal neutron capture cross section for the $^{39}\text{K}(n,\alpha)^{36}\text{Cl}$ reaction on ^{39}K is only 4.3 ± 0.5 millibarns, and the dilute resonance integral is ~ 1.9 millibarns*. Low-energy neutron capture on ^{39}K is only expected to account for $\sim 2\%$ of the total ^{36}Cl production rate from potassium at the surface.

There are four sources of secondary neutrons in the lithosphere which are considered in this work: spallation reactions, negative muon capture reactions, photonuclear reactions and the decay of uranium and thorium. Because the cross section for neutron capture is highest at thermal energies, only the thermal neutron

* The alpha branching ratios have not been measured for any of the ^{39}K resonances. However for light nuclei the level densities are relatively low and the dominant contribution to the resonance integral comes not from the resonances, but from the $1/v$ fall-off in cross section with energy (this is essentially due to the tail of the nearest subthreshold resonance), which contributes cross section beyond the thermal region. The Chart of the Nuclides assumes that the $1/v$ contribution to the resonance integral is 0.45 times the thermal cross section. Hence, to a good approximation, the resonance integral for the alpha-particle branch can be assumed to be 0.45 times the known (n,α) thermal cross section.

capture cross section is considered for each source, except for the spallation reactions. Because spallogenic secondaries at the surface are the largest of all the secondary neutron sources at any depth, epithermal neutron capture will also be considered for spallation secondaries. As a result the production of ^{36}Cl by low-energy neutron capture can be expressed by:

$$P_n(z) = P_{sp-th}(z) + P_{sp-epi}(z) + P_{\mu s}(z) + P_{\mu f}(z) + P_{U+Th} \quad (2.9)$$

The subscripts $sp-th$, $sp-epi$, μs , μf and $U+Th$ denote spallogenic thermal neutrons, spallogenic epithermal neutrons, mu-genic thermal neutrons, photonuclear thermal neutrons, and radiogenic thermal neutrons, respectively.

Secondary neutrons are typically produced with energies above the epithermal and thermal energy ranges and the neutrons have to be slowed down by collisions with terrestrial nuclei to reach epithermal and thermal energy ranges. During this process the number of neutrons may decrease as some take part in other reactions or, at shallow depths, are lost into the air due to an air/ground boundary effect (see § 3.2). As a result of the loss of neutrons near the air/ground boundary, the low-energy neutron sources require a correction at shallow depths, as described below. Section 3.2 contains a more detailed discussion of recent work related to this air/ground boundary effect.

Away from the air/ground boundary, thermal and epithermal neutron production is in equilibrium with the secondary neutron production for all secondary neutron sources.

2.3.3A Thermal Neutrons Produced by the Spallation Reaction

The dominant source of secondary neutrons in the uppermost few metres of the lithosphere is spallation reactions. For this work the thermal neutron model described by Liu *et al.* [Liu94] was adopted, discussed in Section 3.2.2. This model describes the production of ^{36}Cl at the air/rock boundary by solving a diffusion-type equation that balances thermal neutron production and absorption.

$$P_{n,sp-th} = \mathcal{P}_f(0) (f_{35} + f_{39}) (k_1 e^{(-z/\Lambda_{sp})} + k_2 e^{(-z/L_{th})}) \quad (2.10)$$

This expression is effectively an exponential depth profile describing the production of thermal neutrons in the lithosphere, minus (as k_2 has a negative value) an exponential depth profile that describes the diffusion of thermal neutrons into the air.

The parameter f_A is the fraction of thermal neutrons captured by nuclide A (either ^{35}Cl or ^{39}K) and can be expressed by:

$$f_A = \frac{\sigma_A N_A}{\sum_i \sigma_i N_i} \quad (2.11)$$

where σ and N are the thermal neutron cross section and the abundance respectively, and i represents all the nuclides in the rock that significantly contribute to the macroscopic cross section of the rock.

The parameter $\mathcal{P}_f(0)$ is the production rate of spallogenic secondary neutrons (i.e. prior to thermalisation) in the air directly above the ground. The parameter L_{th} is the characteristic length for thermal neutron diffusion in the rock. The parameter k_1 describes production of spallogenic secondary neutrons in rock and can be expressed as:

$$k_1 = \phi_{ss}^* \Sigma_{th,ss} / \mathcal{P}_f(0) \quad (2.12)$$

where ϕ_{ss}^* is the thermal neutron flux that would be observed at the land surface if some neutrons didn't diffuse upward into the atmosphere (as shown in Figure 2.3), and $\Sigma_{th,ss}$ is the macroscopic thermal neutron capture cross section of the rock, which is the denominator in the expression for f_A in Equation 2.11.

The parameter k_2 is related to loss of neutrons into the air, calculated by:

$$k_2 = F \Delta \phi_{ss}^* \Sigma_{th,ss} / \mathcal{P}_f(0) \quad (2.13)$$

where F is the weighting factor that determines the balance of the end members in the actual interface fluxes, and $\Delta \phi_{ss}^*$ is the difference between the thermal neutron fluxes in the air and the ground at the land surface elevation, in the absence of an interface, as shown in Figure 2.3.

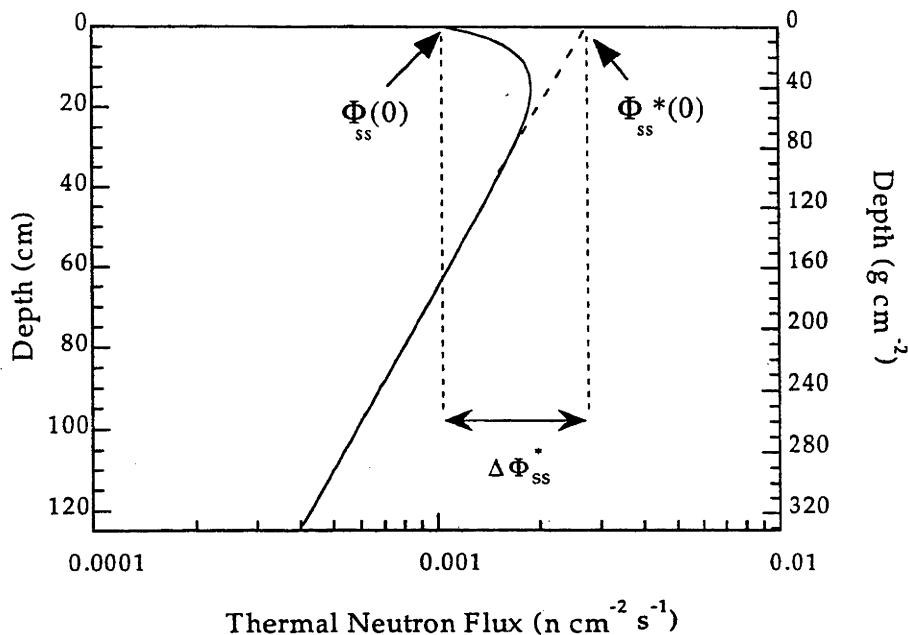


Figure 2.3 Thermal neutron intensities as a function of depth in granite, calculated by the equation $\mathcal{P}_f(0)(k_1 e^{(-z/\Lambda_\varphi)} + k_2 e^{(-z/L_{th})})$ using typical values for granite given by Liu *et al.* [Liu94], where $\mathcal{P}_f(0) = 586$ fast n (g air)⁻¹ yr⁻¹ [Phi96], $k_1 = 1.008$, $\Lambda_\varphi = 170$ g cm⁻², $k_2 = -0.624$, and $L_{ss} = 22.6$ g cm⁻².

The parameters f_{35} , f_{39} , k_1 , k_2 , and L_{th} in Equation 2.10 depend on composition and can be calculated for each sample. As a result, $\mathcal{P}_f(0)$ is the component of the spallogenic portion of the thermal neutron flux in the lithosphere that must be calibrated to determine the production rate of ³⁶Cl from thermalised spallogenic secondary neutrons.

2.3.3B Epithermal Neutrons Produced by the Spallation Reaction

The dilute resonance integral is reasonably large for ³⁶Cl compared to the thermal neutron capture cross section (~40%). Consequently, the proportion of ³⁶Cl produced by spallogenic secondaries in the epithermal range is 20-40% of the total ³⁶Cl produced by spallogenic neutrons. However, the actual proportion depends strongly on the chemistry of the rock, as discussed in Section 3.2.

The expression describing spallogenic epithermal neutron production of ^{36}Cl is analogous to Equation 2.10

$$P_{n,sp-epi} = \mathcal{P}_f(0)(f_{epi,35} + f_{epi,39})(k_3 e^{(-z/\Lambda_{sp})} - k_4 e^{(-z/L_{epi})}) \quad (2.14)$$

The parameter L_{epi} is the characteristic length for epithermal neutron diffusion in a particular rock type. The parameter $f_{epi,A}$ is the fraction of subsurface epithermal neutrons absorbed by ^{35}Cl or ^{39}K respectively, and is the epithermal equivalent of Equation 2.11, except that it contains the dilute resonance integral I_A instead of the thermal neutron cross section:

$$f_{epi,A} = \frac{I_A N_A}{\sum_i I_i N_i} \quad (2.15)$$

The parameters k_3 and k_4 can be expressed by the relations:

$$k_3 = (1 - p(E_{th})_{ss}) \times \left[\frac{A_{ss}}{A_a} \right]^{\frac{1}{2}} \quad (2.16)$$

$$k_4 = F_{epi} (1 - p(E_{th})_{ss}) \times \left[\frac{A_{ss}}{A_a} \right]^{\frac{1}{2}} \quad (2.17)$$

where $p(E_{th})_{ss}$ is the resonance escape probability for epithermal neutrons in the rock. A is the average atomic mass of the medium (air or sub-surface rock), and the subscripts ss and a refer to the subsurface and the atmosphere respectively. F_{epi} is the fractional reduction (relative to an infinite rock medium) in the epithermal neutron flux at the atmosphere/rock interface. This parameter was assigned a value of 0.4 based on simulations of neutron transport by the Monte Carlo method [Phi95].

As with Equation 2.10, the parameters in Equation 2.14 can be calculated from the sample composition, with the exception of $\mathcal{P}_f(0)$, which must be calibrated.

2.3.3C Thermal Neutrons Produced by the Negative Muon Capture Reaction

The second source of thermal neutrons is from negative muon capture reactions. Following the capture of a negative muon by any constituent of the rock, the nucleus most commonly de-excites by the evaporation of one or more neutrons. Therefore the calculations include all target nuclei present in the rock and all emission channels that include neutrons.

The production of ^{36}Cl from mu-genic neutron capture can then be expressed by:

$$P_{n,\mu^-}(z) = \Psi_{\mu^-}(z) Y_s (f_{35} + f_{39}) \quad (2.18)$$

The term Y_s is the average neutron yield from a muon capture and can be calculated by:

$$Y_s = \sum_i f_{c,i} f_{d,i} (f_{1n,i} + 2 \times f_{2n,i} + 3 \times f_{3n,i} + \dots) \quad (2.19)$$

where i is an elemental constituent in the rock, and f_c is the compound factor and f_d is the fraction of muons captured from the 1s muonic level by the nucleus, as described in § 2.3.2.

The value of Y_s is specific to a particular rock-type for two reasons. Firstly, the number of neutrons emitted by a particular nucleus varies from nucleus to nucleus. And secondly, the compound factor term, f_c , affects the portion of negative muons that will be captured by each component of a mineral. The variation of this value from rock type to rock type, however, is expected to be small, and given that this is not a dominant production channel, an assumed value of 0.5 neutrons per stopped μ^- has been used.

The air/ground boundary effect has only been investigated for spallogenic secondary neutrons. However, for surface samples, the air/ground boundary effect can be approximated by multiplying Equation 2.18 by the same correction determined for spallogenic thermal neutrons, Φ_{ss}/Φ_{ss}^* , or in the terms used in Equation 2.10, $(k_1 + k_2)/k_1$.

2.3.3D Thermal Neutrons Produced by the Photodisintegration Reaction

The third (and final cosmogenic) source of thermal neutrons is from photodisintegration reactions initiated by positive and negative fast muons, as described in Section 2.2.2. The treatment of photonuclear secondaries follows the treatment used by Fabryka-Martin [Fab88], and can be described by the equation:

$$P_{n,f}(z) = \Phi_{\mu\pm}(z) Y_f k_5 \ln(k_6 z) (f_{35} + f_{39}) \quad (2.20)$$

The term $\Phi_{\mu\pm}(z)$ is the total cosmic ray muon flux at depth z at sea level and high latitude as given by the expression derived by Stone *et al.* [Sto98]:

$$\log_{10} [\Phi_{\mu\pm}(z)] = A + B \log_{10}(z) + C (\log_{10}(z))^2 + D (\log_{10}(z))^3 + E (\log_{10}(z))^4 + F (\log_{10}(z))^5 \quad (2.21)$$

where $A = 5.059$, $B = 2.088$, $C = -2.235$, $D = 1.127$, $E = -0.2634$, $F = 0.02138$

The term Y_f is the average neutron yield per photodisintegration. As this is a very minor source of secondary neutrons in the depth range we are considering, the conventional value of one neutron per disintegration [Wyk65; Hay69] can be assigned to Y_f without fear of added uncertainty due to oversimplification.

The term $k_5 \ln(k_6 z)$ is derived from the gamma absorption cross section over the bremsstrahlung spectrum, the energy at which the cross section reaches its maximum and the gamma ray flux above this threshold. The logarithmic term $\ln(k_6 z)$, accounts for the energy lost by the total muon flux at depth z which causes the production of neutrons by fast muons to decrease more gradually with depth than the production by stopped negative muons. Consequently, this is one of the major production mechanisms of ^{36}Cl below a depth of ~20 metres. The values of k_5 and k_6 are composition dependent and can be calculated using the formula given in Fabryka-Martin [Fab88] and Hayakawa [Hay69]. However, as this is a minor source of secondary neutrons in the depths considered in this work, and variation in the values of k_5 and k_6 is <1% from sample to sample, values of 7.75×10^{-6} and 0.1065 are used for k_5 and k_6 respectively for all the samples.

The surface samples can be corrected for the air/ground boundary effect in the same manner as the thermal neutrons produced by negative muon capture reactions, i.e. multiplying Equation 2.20 by $(k_1 + k_2)/k_1$.

2.3.3E Thermal Neutrons Produced by the Radioactive Decay of U and Th

Finally, neutrons are produced from spontaneous fission of ^{238}U , and (α, n) reactions due to α -particles from the U and Th α -decay series. This production of neutrons is dependent on the uranium and thorium contents of the rock, and therefore produces a background of non-cosmogenic ^{36}Cl concentration that must be subtracted.

$$P_{n,U+Th} = (\mathcal{P}_\alpha + \mathcal{P}_{sf})(f_{35} + f_{39}) \quad (2.22)$$

where the subscripts α and sf denote neutron production by reaction due to α -particles and spontaneous fission respectively. The term \mathcal{P}_α is expressed by:

$$\mathcal{P}_\alpha = \left(\frac{\sum_i S_i F_i Y_n(U)}{\sum_i S_i F_i} \right) \times [U] + \left(\frac{\sum_i S_i F_i Y_n(Th)}{\sum_i S_i F_i} \right) \times [Th] \quad (2.23)$$

where S_i is the mass stopping power of the element i for α -particles,

F_i is the fractional abundance (ppm) of element i ,

$Y_n(U)$ is the neutron yield of element i per ppm U,

$Y_n(Th)$ is the neutron yield of element i per ppm Th,

$[U]$ is the uranium concentration in ppm,

$[Th]$ is the thorium concentration in ppm.

Values for the elemental neutron yields are given by Vandenbosch and Huizenga [Van73].

The term \mathcal{P}_{sf} is expressed by:

$$\begin{aligned} \mathcal{P}_{sf} &= N_{238} \lambda_{238} \Gamma_{238} \nu_n \\ &= 0.429 [U] \end{aligned} \quad (2.24)$$

where: N_{238} is the atomic concentration of ^{238}U in the sample,

λ_{238} is the decay constant for $^{238}\text{U} = 1.5513 \times 10^{-10} \text{ yr}^{-1}$,

Γ_{238} is the branching ratio for spontaneous fission = 5.45×10^{-7} ,

ν_n is the number of neutron emitted per spontaneous fission of $^{238}\text{U} = 2.00 \pm 0.03$ [Van73], and

[U] is the uranium concentration in ppm.

2.4 The Importance of AMS

The technique of accelerator mass spectrometry (AMS) is crucial to the feasibility of studying cosmogenic nuclides. The number of *in-situ* cosmogenic atoms in a natural sample is very small, typically $10^4 - 10^7 \text{ atom g}^{-1}$, or $10^{-18} - 10^{-15}$ of the total atoms in a rock sample. In addition, their half lives are extremely long compared to the available measuring time. As a result they have a very low decay rate which makes decay counting almost impossible. In most cases the ratio of the cosmogenic nuclide to the stable nuclide/s is very low ($10^{-15} - 10^{-12}$ for typical $^{36}\text{Cl}/\text{Cl}$ ratios) which also rules out the use of conventional mass spectrometry as a feasible measurement technique.

As an example, consider a ^{36}Cl measurement made on a typical sample with a chloride concentration of 100 ppm and a $^{36}\text{Cl}/\text{Cl}$ ratio of 100×10^{-15} . For a practical measurement by decay counting, a minimum decay rate of ~ 0.1 decays/min is required. This would require 2.28×10^{11} atoms of ^{36}Cl , or 136g of chloride, necessitating 1.36 tonnes of sample. Measurement by AMS, on the other hand, provides the sensitivity to measure the 1.7×10^6 atoms of ^{36}Cl in a 10 g sample from which 1 mg of chloride would be obtained. Since AMS involves physical counting of the individual atoms, rather than decays, this sample could be measured with a precision of $\leq 5\%$, detecting ≥ 400 ^{36}Cl ions in less than 30 minutes.

Accelerator mass spectrometry is an extension of normal mass spectrometry (see Figure 2.4), with the ability to measure nuclide ratios being extended from 10^9 to 10^{-15} [Lit87]. Both systems have the sample placed in an ion source from which

ions are emitted, before being accelerated by an electric potential and mass-analysed by a magnet. A conventional mass spectrometer then measures the number of ions as a current in a Faraday cup or as individual ions using an electron multiplier (or Daly detector). AMS, however, further accelerates the ions to a terminal at high electric potential, where they pass through an electron stripping foil or gas which removes some or all of the electrons. The now highly positively charged ions are further accelerated to a second magnet. This selects the mass and charge state of the ions, which are then measured by counting them individually in a particle detector. (Details of AMS measurements will be discussed in chapter 4).

Given the small numbers of atoms and the extremely low nuclide ratios to be measured, AMS has certain advantages over conventional mass spectrometry:

1. Mass spectrometry measurements are limited by abundance sensitivity, the background count rates at masses adjacent to the nuclide of interest. The abundance sensitivity for a typical mass spectrometer is $\sim 10^{-5}$, or $\sim 10^{-10}$ for large multi sector instruments. With $^{36}\text{Cl}/^{37}\text{Cl}$ ratios as low as 10^{-14} , the ^{37}Cl tail would swamp the ^{36}Cl peak*. AMS, however, recognises the ions by exploiting the difference in rates of energy loss of the ions individually at high energy (~ 150 MeV).

2. A second challenge for the detection of small numbers of atoms of ^{36}Cl is the presence of interfering ion beams from the isobar, ^{36}S , and molecules such as, $^{18}\text{O}_2$ and $^{12}\text{C}_3$. In a conventional mass spectrometer these must be distinguished on the basis of their small difference in mass (see Table 2.6). To obtain the resolution required to separate isobars and interfering molecules from the nuclide of interest, conventional mass spectrometry typically works with ion beams in the nA range to maximise the focus of the beam and reduce the width of the peaks. This, however, also reduces their intensity, so that for nuclides with extremely low abundances (such as ^{36}Cl) this would result in prohibitively low count rates.

* As an ion is more likely to lose energy than gain energy, there is a tail on the low energy side of the peak.

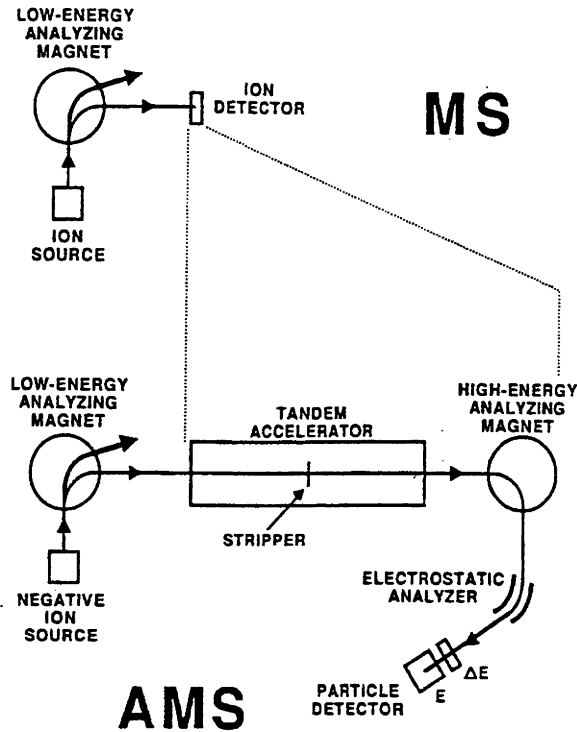


Figure 2.4 Schematic comparison of Accelerator Mass Spectrometry to normal Mass Spectrometry.

In contrast, AMS totally removes molecular interferences when the ions are stripped, as molecules dissociate when they become highly positively charged, while the isobar, ^{36}S , is separated from ^{36}Cl by the different rates of energy loss, which depends on the atomic Z number (see §4.3), rather than by their mass difference.

Table 2.6. The atomic mass of isobars and molecules that can smother the ^{36}Cl peak during conventional mass spectrometry.

Isobar or Molecule	Atomic Mass	Difference from ^{36}Cl
^{36}Cl	35.9683009	-
^{36}S	35.9670808	0.0034%
$^{18}\text{O}_2$	35.99832	0.083%
$^{12}\text{C}_3$	36.00000	0.088%

Chapter Three

CALIBRATION OF THE PRODUCTION OF ^{36}Cl FROM POTASSIUM: BACKGROUND AND STRATEGY

There are several production channels that lead to the production *in-situ* of ^{36}Cl , hence, the calibration is complicated by the need to determine separately the rate of each mechanism. While this makes the calibration challenging, the variety of production mechanisms will allow ^{36}Cl to be used to study a wide range of rock compositions and sample depths in the future.

The previous calibrations of the production of *in-situ* ^{36}Cl from potassium are described in Section 3.1, while Section 3.2 describes several recent studies on the low-energy neutron flux at the air/ground boundary. Finally, Section 3.3 outlines the calibration strategy implemented in this work.

3.1 Previous Work

Three previous attempts to calibrate the *in-situ* production rate of ^{36}Cl have been reported. The basic approaches of each of these studies were very similar; ^{36}Cl measurements were made on surface rock samples collected from areas that were believed to have a negligible erosion rate and an accurate exposure age determined by an independent method.

The previous authors [Zre91, Swa94, Phi96] determined only a single production rate for potassium which they termed "potassium spallation". Although spallation is the dominant source of ^{36}Cl from potassium at shallow depths, it is also produced by negative muon capture and by low-energy

neutron capture. To avoid confusion, the symbols P_K and P_{Ca} will be used when discussing the quantities calibrated by the previous authors.

The evolution of the ^{36}Cl production rate due to potassium calibration is described below.

3.1.1 The Calibration by Zreda *et al.* (1991)

The first study to determine experimentally the surface production rates of ^{36}Cl from potassium, calcium, and chloride was performed by Zreda *et al.* [Zre91]. The results of this calibration can be seen below in Table 3.1. The P_K production rate and low-energy neutron capture on ^{35}Cl were constrained by three rock samples collected from glacial moraine boulders from the Chiatovitch Creek in the White Mountains in eastern California, whose age has been determined by ^{14}C measurements on rock varnish. The ^{14}C age* was used in the calibration rather than being converted to a calendar age, as the ^{14}C calibration curve for this time period had not been confirmed and Zreda *et al.* believed the ^{14}C age would underestimate the real age by only 2-3 ka.

Table 3.1 Results of the previous three calibrations.

Reference	P_K^a atom (gK) $^{-1}$ yr $^{-1}$	$P_{Ca}^{a,b}$ atom (gCa) $^{-1}$ yr $^{-1}$	Low-energy neutron capture on $^{35}\text{Cl}^a$
Zreda et a. (1991)	107 (8)	73 (5)	ϕ_n^c : $3.07 (0.24) \times 10^5$ n kg $^{-1}$ yr $^{-1}$
Swanson <i>et al.</i> (1994)	225 (28)	90 (5)	ϕ_n^c : $3.62 (0.13) \times 10^5$ n kg $^{-1}$ yr $^{-1}$
Phillips <i>et al.</i> (1996)	154 (10)	73 (5)	$\mathcal{P}_f(0)^d$: 586 (40) fast n (g air) $^{-1}$ yr $^{-1}$

^a At sea level and high latitude.

^b Additional calibration of the production rates of spallation and negative muon capture on calcium has been made, and is used in this work [Sto96, Sto98]. Combined, they give a value for P_{Ca} of 64.2 (4.5) atom (gCa) $^{-1}$ yr $^{-1}$.

^c The thermal neutron stopping rate, defined below in Equation 3.1.

^d The production rate of spallogenic secondary neutrons (i.e. prior to thermalisation) in the air directly above the ground, discussed in Section 2.3.1C.

* Radiocarbon dating was originally based on the assumption that the total amount of ^{14}C in the atmosphere was constant with time. It was later shown that atmospheric ^{14}C concentrations have varied significantly and as a result, a ^{14}C calibration curve has been built up from ^{14}C measurements made on samples whose age can be independently verified. As this curve is continuously being extended and refined, ^{14}C measurements are often expressed in “ ^{14}C years BP”, so the reader can use the latest calibration curve to determine a “calibrated” or “cal.” age.

From the three rock samples, seven mineral fractions (bulk and/or quartz and/or microcline*) were prepared for ^{36}Cl analysis. From these, the four with the highest potassium content (4.51 – 7.20% K) were chosen to determine the value of P_K . For each of these, ^{36}Cl production from potassium accounted for almost half the total ^{36}Cl production, with the bulk of the remainder coming from 130-160 ppm Cl.

Five of the seven mineral fractions from the Chiatovitch Creek samples (including two that were used for the calibration of P_K) were used to determine the value for the production rate due to thermal neutron capture on ^{35}Cl . The Ca, K, and Cl concentrations were < 0.35% Ca, 0.31-4.51 %K and 101-160 ppm Cl. For this first attempt at a calibration, thermal neutrons were treated by assuming a linear relationship between thermal neutron production and thermal neutron capture for all rocks:

$$\Psi_n = \phi_n f_{35} \quad (3.1)$$

where Ψ_n is the thermal neutron capture rate on ^{35}Cl , ϕ_n is the thermal neutron production rate at sea level and high latitude, and f_{35} is the fraction of thermal neutrons which are captured by ^{35}Cl (see Equation 2.11).

The P_{Ca} production rate was constrained by samples from the Tabernacle Hill basalt flow in Utah, the age of which is based on bracketed ^{14}C dates. The ^{36}Cl in these samples was dominated by production from calcium, with concentrations for calcium > 7.6 % Ca, potassium < 0.71%K and chloride 94-111 ppm Cl.

The production rates determined by Zreda *et al.* were supported by ^{36}Cl measurements made on 5 dolomite samples from Meteor Crater, Arizona and 4 samples from Tioga-age moraines in Bloody Canyon in the Sierra Nevada. The Meteor Crater samples were chiefly a test of the P_{Ca} production rate as dolomite, a carbonate mineral, is ~21%Ca. The mean age determined for these samples, 49.7 (0.85) ka is in good agreement with ages of 49.0 (3.0) ka obtained by thermoluminescence studies [Sut85], and 49.2 (1.7) ka obtained from cosmogenic $^{26}\text{Al}/^{10}\text{Be}$ measurements [Nis91b].

The Bloody Canyon samples were not strictly independent tests of P_K , as both they and the Chiatovitch Creek samples were deposited by the same glacial event and were dated by the same rock-varnish ^{14}C technique. However, exposure ages of three of the four samples, with an average of 21.2 (1.6) ka, are

* A type of K-feldspar that was formed at low temperature.

in agreement with the ^{14}C varnish age of 18.9 ka. This not only gave support to the calibration, but also demonstrated the reproducibility of the ^{36}Cl measurements from geological samples.

As well as calibrating the production rates, Zreda *et al.* [Zre91] reported a test of the altitude/latitude scaling parameters. Prior to their work there were several published altitude/latitude scaling parameters that differed by as much as 100% [Lin63, Yok77, Lal91]. The latitude test was performed on 4 basaltic and hawaiitic boulders from late Pleistocene moraines at similar elevation to the calibration sites, but different geomagnetic latitudes. The ^{36}Cl ages calculated using Lal's scaling parameter [Lal91] were in very good agreement with the ^{14}C varnish ages, as opposed to the other scaling parameters which were as much as 50% higher. The altitude test was performed by measuring the ^{36}Cl concentration in eleven Hawaiian samples ranging in altitude from 0.4 km to 4.05 km and with constant latitude. Once again Lal's scaling parameters fitted the measurements better, with an average difference of 8%, which was within the measurement uncertainty.

3.1.2 The Calibration by Swanson (1994)

An early indication that there was a problem with the calibration of Zreda *et al.* [Zre91], came from measurements by Swanson [Swa94]. He determined ^{36}Cl concentrations in 15 till* boulders deposited on the Whidbey and Fidalgo Islands by the Puget Lobe of the Cordilleran Ice Sheet during the Vashon Stade of the Fraser Glaciation. The age of deposition and initial exposure of these samples is closely bracketed by ^{14}C measurements to between ca. 14,600 and 13,500 ^{14}C yr B.P [Swa94 and references therein]. When the ages were calculated with Zreda's production rates and Lal's scaling parameters the ^{36}Cl ages were clearly inconsistent with the ^{14}C ages, with the discrepancy being greatest for potassium-rich samples.

Consequently, Swanson attempted to recalibrate the production rates based on a new set of thirty-four carefully chosen whole rock samples from the Whidbey and Fidalgo Islands with very good ^{14}C age control. From this they determined the value of P_k to be more than twice that of Zreda *et al.* (Table 3.1).

The calibration was performed in three steps;

* Material deposited by glaciers and ice sheets.

Step 1: By adopting the treatment of thermal neutrons used by Zreda, Swanson determined ϕ_n from a group of 11 bedrock samples with mostly high chloride concentrations (14-290 ppm Cl) and low calcium and potassium concentrations.

Step 2: By using the average value of ϕ_n derived in step 1, he determined P_{Ca} from 13 samples with high Ca (4.4-11.8 %Ca), variable chloride (19-102 ppm Cl), and low potassium (0.02 – 0.33 %K).

Step 3: P_{K} was determined from a third group of 10 samples using the average values derived in step 1 and 2. The samples contained similar potassium and calcium concentrations (0.70-3.83%K and 0.29-4.40%Ca) and variable chloride concentrations (10-278 ppm Cl). While none of the samples in the calibration had very high potassium concentrations, six of the ten samples in the final group had more than 65% of their total ^{36}Cl production due to potassium.

As a result of this method, the value determined for P_{K} in Swanson's study is sensitive to uncertainties in the determination of ϕ_n and P_{Ca} , with any error in the calibration of the latter rates producing a compensating error, of an opposite sign, in the value of P_{K} .

3.1.3 The Calibration by Phillips *et al.* (1996)

Following the study by Swanson, there was some debate as to the source of error in the original calibration by Zreda *et al.* [Zre91], with general agreement that the problem lay in some aspect of the assumed exposure history of the Chiatovitch Creek moraine boulders [Swa94, Phi96]. It also became apparent around this time that the treatment of low-energy neutrons that had been used in the first two calibrations was too simplistic and there was a large air/ground boundary effect on the low-energy neutron flux that was highly dependent on the rock composition ([Dep94, Liu94] discussed below). When a better treatment of low-energy neutrons was developed by Liu *et al.* [Liu94], Phillips *et al.* were able to incorporate this to re-analyze the ^{36}Cl production rates. Discarding the samples from the Chiatovitch Creek moraine boulders, Phillips *et al.* added to the two Tabernacle Hill basalt samples, another 33 samples from 18 locations. The samples were predominantly lava flows (typically Ca-rich and K-poor) and had independently measured ages ranging from 2 ka to 55 ka.

In the new treatment of low-energy neutrons, rather than calibrating the thermal neutron capture rate in rock (Equation 3.1), Phillips *et al.* [Phi96]

determined the value of the production rate of secondary neutrons in air at sea level and high latitude, $\mathcal{P}_f(0)$ as described by Liu *et al.* [Liu94] and outlined in Equation 2.10. Epithermal neutrons were also treated in an analogous manner [Phi95], as outlined in Equation 2.14.

The third calibration was performed in two steps. First, three sets of samples were used to determine the ratios of the production rates. Each set contained samples with identical exposure histories but widely varying chemical compositions, principally achieved by measuring different mineral separates from the same rock sample (see Table 3.2). The ratio $\mathcal{P}_f(0)/P_{Ca}$ was determined to be 1.20×10^{23} (fast n (g air) $^{-1}$ yr $^{-1}$)/(atom ^{36}Cl (atom Ca) $^{-1}$ yr $^{-1}$). The ratio P_K/P_{Ca} was determined to be 2.05. For comparison, by taking the final values from the calibration performed by Swanson, a value of 2.50 for the P_K/P_{Ca} ratio is obtained.

Table 3.2 Samples used by Phillips *et al.* to determine the ratios of the ^{36}Cl production [Phi96].

Sample Name	Location and Type	Cl ppm	K %wt	Ca %wt
RC95-1A	Glacially polished metamorphic outcrop, Reverse Creek, eastern Sierra Nevada	52.7	1.51	6.18
RC95-1B		127	0.05	18.46
RC95-1C		117	3.87	6.21
BPCR95B-5A	Glacially polished granodiorite and mafic xenolith, Bishop Creek, eastern Sierra Nevada	67.9	2.32	3.89
BPCR95B-5A		212	1.18	6.62
MC1-1 Qtz	Quartz separate and bulk siliceous dolomite, ejecta boulder,	17.0	0.0	0.0
MC1-1 Bulk	Meteor Crator, Arizona (from [Dep95]).	70.0	0.33	7.18

The second step in the calibration used these ratios of production rates to obtain an equation for ^{36}Cl accumulation with only the term P_{Ca} as an unknown. This equation was then applied to 33 whole rock samples and the best fit value of P_{Ca} was obtained. The values for the other production rate were then calculated (see Table 3.1). The deduced production rate due to potassium was particularly vulnerable to errors from the other production rates as only a small fraction of the total ^{36}Cl production was due to potassium in almost all of the samples (as demonstrated in Figure 1.1). Of the 33 samples in the second step, only three had more than a quarter of the ^{36}Cl concentration produced by potassium, and for those three samples it was because they had very low calcium and chloride concentration, rather than high potassium concentrations.

In their analysis, Phillips *et al.* did not evaluate the uncertainty in the ratios of production rates. Consequently, the real uncertainty in value of P_K determined by Phillips *et al.* will be larger than the 6.5% error stated.

3.2 Low-Energy Neutrons at the Air/Ground Boundary

Secondary cosmic ray neutrons are produced by many reactions (see Chapter 2) but at the air/ground boundary they are predominantly produced by spallation reactions. These neutrons are produced with an average energy of 1 MeV, and to reach the low-energy region (≤ 1 keV) they must lose kinetic energy through collisions with surrounding nuclei. This transfer of energy is much more effective with light nuclei, particularly hydrogen. In addition, the probability of the neutron being absorbed into the nucleus of an atom that it collides with generally increases as the neutron energy decreases.

The epithermal neutron flux is most affected by the moderating properties of the air and ground. Air is a better moderator than dry rock by about an order of magnitude. However, small amounts of water (containing hydrogen) greatly increase the ground's bulk moderating ability, so that saturated soil is about five times more effective at moderating the neutrons than air. As a result, dry soil usually has a much higher epithermal neutron flux than the atmosphere, but wet soil has a lower epithermal flux [Phi01].

In contrast, the thermal neutron flux is dominated by the absorption properties of the air and ground. As nitrogen has a comparatively large thermal neutron absorption cross section, the atmosphere typically has a macroscopic thermal neutron capture cross section about an order of magnitude larger than that of most rock types. The thermal neutron flux is therefore typically higher in rock or soil than it is in the atmosphere.

The result of these differences is a discontinuity in neutron production, thermalisation and absorption properties at the air-ground boundary. However, because the mean-free-path of neutrons in both media is long (between a few g cm^{-2} and tens of g cm^{-2} , depending on energy), neutrons can diffuse across the boundary from the medium of high neutron density to the medium of low neutron density. This results in smooth thermal and epithermal neutron fluxes and ^{36}Cl production rates across the boundary, with (usually) a deficiency in the rate of ^{36}Cl production relative to spallogenic neutron production in the rock immediately below the surface, and a corresponding

excess in the air above. The deficiency in ^{36}Cl production extends to depths a few times the thermal neutron diffusion length - typically $\sim 50 \text{ g cm}^{-2}$. Because of the large dependence on the chemical composition of the ground, the treatment of low-energy neutrons can have a large impact on the calibration of the ^{36}Cl production rates due to potassium.

The air/ground boundary effect for thermal neutrons was first investigated theoretically in 1940 by Bethe *et al.* [Bet40] for the case of air over water. These predictions were then experimentally confirmed by Swetnick in 1954 [Swe54]. Over the following several decades the boundary effect was investigated for other situations, such as air over dry soil, iron and aluminium [Yam66, O'Br78].

In the last decade there have been several air/ground boundary studies focused principally on how thermal neutrons should be treated for *in-situ* cosmogenic nuclide studies. Three different approaches to these investigations include:

1. simulations of the top metre of the earth's crust
2. computational models
3. isolation and measurement of the $^{35}\text{Cl}(n,\gamma)^{36}\text{Cl}$ channel in rock samples

Some of the key results of each method are described below.

In all the simulations and computational modeling, the only source of low-energy neutrons considered was spallation reactions, which are the dominant source of secondary neutrons in the uppermost few metres of the lithosphere. As additional sources of low-energy neutrons are included in this study, the values obtained in the previous studies must be adjusted to enable a comparison to be made with the values obtained in this work.

3.2.1 Simulations of the Earth's Crust

Liu *et al.*, [Liu94] reported the results of thermal neutron flux measurements made in a cement block (3.7m x 3.7m x 0.9m) designed to simulate the uppermost metre of the earth's surface. One of the chief motivations for this work was to provide data that could be used to develop and test models for predicting neutron fluxes and nuclide production rates in geological systems.

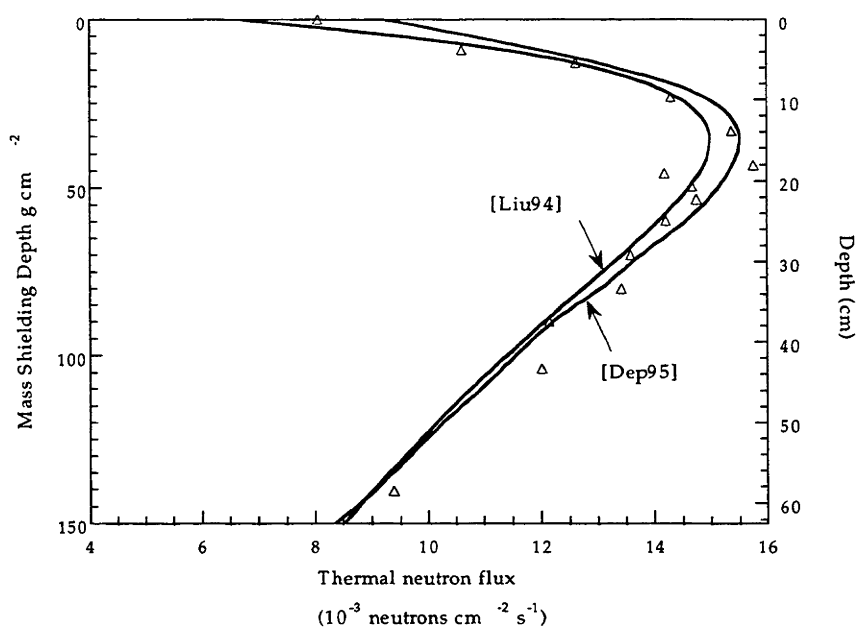


Figure 3.1 Comparison of the results for the thermal neutron flux as a function of depth. Measured data obtained in the cement block simulation are shown by the triangles, Liu *et al.*'s model of the cement block experiment, and Dep's model of the cement block experiment are also shown as indicated. Adapted from figures in Dep (1995) and Liu *et al.* (1994).

The influence which the air/ground boundary in the cement block (see [Liu94] for elemental composition) has on the thermal neutrons becomes minimal at 50 g cm⁻². At the surface the thermal neutron flux was almost 50% less than the flux at 50 g cm⁻² depth due to the loss of low-energy neutrons from the concrete into the atmosphere.

3.2.2 Computational Models

The results of the cement block simulation were used by both Liu *et al.* [Liu94] and Dep [Dep95] to compare very different computational modeling. Dep used Monte Carlo methods to simulate the secondary cosmic ray cascade in the atmosphere and the transport of neutrons near the air/ground boundary. This requires tremendous computer power and access to large neutron cross section libraries. Figure 3.1 compares the measurements obtained from the cement block simulation to theoretical results obtained by Dep for this situation.

Dep investigated the effect of both water content and the bulk composition of the rock on the low-energy neutron flux and the relative production of ^{36}Cl from neutron capture on ^{35}Cl at the air/ground boundary. He

demonstrated that the thermal neutron flux can vary by a factor of two depending on the water content and the elemental composition of the rock (see Table 3.3). These calculations highlight the importance of water content in determining the thermal neutron flux. Unfortunately water content is very difficult to measure accurately and has the potential to vary over time. However, the ^{36}Cl production from low-energy neutron capture on ^{35}Cl isn't as dependent on water content as the thermal neutron flux since a significant proportion of the production occurs at epithermal energies [Dep95] (see Table 3.3). For low porosity rocks such as granite, uncertainties in the water content could result in a 15% uncertainty in the calculated low-energy neutron capture on ^{35}Cl production rate [Dep95]. For porous rock-types, with possible large changes in water content, there are correspondingly much higher uncertainties in the calculated production rate [Dep95].

Table 3.3 Surface thermal neutron fluxes and ^{36}Cl production by neutron capture for different rock types and water content, calculated by the Monte Carlo method [Dep95].

Rock Type	Granite			Basalt	Dolomite
	1.0 wt % water	2.0 wt % Water	4.0 wt % water		
Thermal Neutron Flux ^a (Relative to 1.0 wt % water)	1.00	1.20	1.43	0.78	1.36
^{36}Cl Production ^b (Relative to 1.0 wt % water)	1.00	1.07	1.18	0.84	1.24
Proportion of Neutron-Capture ^{36}Cl Produced at Energies ≤ 0.1 eV	59%	67%	75%	54%	66%

^a Calculated using a standard elemental composition for that rock type, see table in [Dep95].

^b The average production for the top 5 g cm⁻². Assuming a potassium concentration of 4.53%, 0.79% and 0.47%, and a calcium concentration of 0.95%, 7.68% and 17.3% and a macroscopic thermal neutron capture cross section of 0.0057 cm² g⁻¹, 0.0076 cm² g⁻¹ and 0.0038 cm² g⁻¹ in granite, basalt and dolomite respectively.

In comparison to Dep's computational modeling, Liu *et al.*, [Liu94], attempted to develop a simple but physically based model for the thermal neutron flux as a function of depth that could be readily used to extract geological information from *in-situ* cosmogenic nuclide measurements. Their model takes the high energy neutron flux in air directly above the ground, $\mathcal{P}_f(0)$, as input, and solves a simple diffusion-type equation that balances thermal neutron production and absorption. The solution to these equations is shown in Section 2.3.3A and is used in this work. Figure 3.1 gives a comparison of the measurements obtained from the cement block simulation (discussed above) to the theoretical results obtained by Liu *et al.* for this situation. In addition, Figure 3.2 compares the thermal neutron flux with depth obtained by Liu *et al.*'s

model with those obtained by Dep's Monte Carlo model for various rock types. The two models are in good general agreement.

The major limitation of the model obtained by Liu *et al.*, is that it neglects intermediate energy interactions, and therefore doesn't include epithermal neutron capture. Phillips *et al.* [Phi96] overcame this by including epithermal neutrons in an analogous, but separate, manner to Liu's treatment of thermal neutrons (see § 2.3.3B), which is the method used in this work. In their calibration, Phillips *et al.*, [Phi96] deduced the value of $\mathcal{P}_t(0)$ as 586 ± 40 neutrons $(\text{g air})^{-1} \text{yr}^{-1}$.

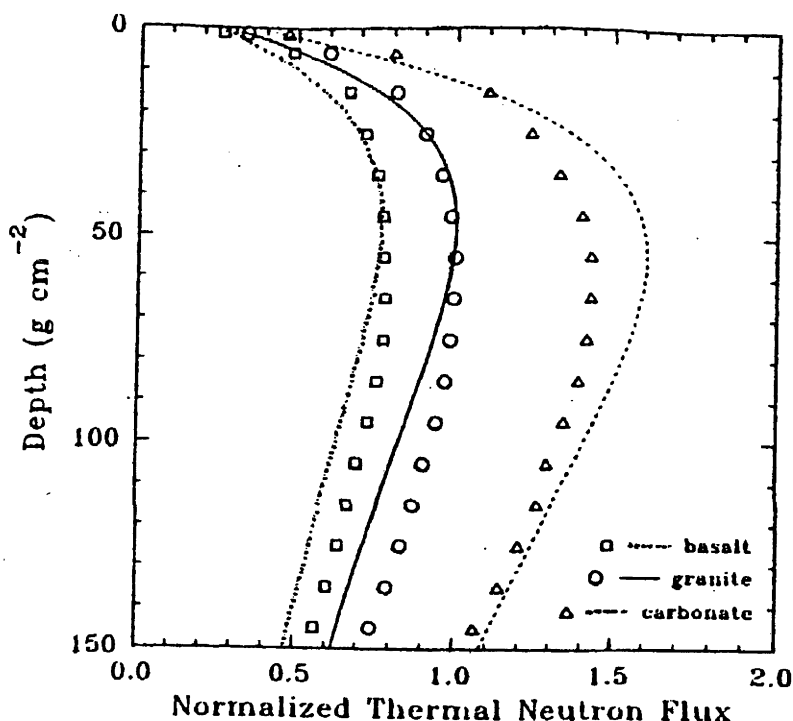


Figure 3.2 Comparison of the thermal neutron flux with depth as calculated by Liu's model (given by labeled lines) and Dep's model (given by labeled symbols) for basalt, granite and carbonate rock. From Liu *et al.*, [Liu94].

In addition to the computational modeling summarized above, a new model of low-energy neutrons by Phillips *et al.* [Phi01] promises to overcome many of the problems of the treatment of Liu *et al.* [Liu94], while still having the practical advantages of being analytical rather than requiring the time consuming Monte Carlo approach. This new model takes a similar approach to Liu *et al.*, however, instead of deriving the thermal neutron flux directly from the high-energy neutron flux, first the epithermal neutron flux is derived from

the high-energy flux (by solving a similar diffusion-type equation). The results of this are then used to derive the thermal neutron flux.

3.2.3 Physically Isolating the $^{35}\text{Cl}(n,\gamma)^{36}\text{Cl}$ Channel

The third method of investigating the low-energy neutron flux at the air/ground boundary is to isolate the $^{35}\text{Cl}(n,\gamma)^{36}\text{Cl}$ production channel in rock samples, see for example Bierman *et al.*, [Bie95] and Dep [Dep95] and the discussion below.

Bierman *et al.*, [Bie95], presented a study in which they attempted to estimate the relative ages of debris-flow fan surfaces and erosion rates of bedrock by isolating the $^{35}\text{Cl}(n,\gamma)^{36}\text{Cl}$ production pathway. Their assumption was that the fluid inclusions in his granitic samples contained a large portion of the chloride in the rock, and very little potassium or calcium (although no potassium, calcium or chloride measurements were made to confirm this assumption). So by crushing the whole rock samples very finely, at least the largest fluid inclusions would break open to release the chloride. Due to the hydrophilic nature of chloride, it could be collected by soaking the sample in distilled water, centrifuging the sample, and pouring off the solution. Chloride was then extracted from the solution by precipitating AgCl and the $^{36}\text{Cl}/\text{Cl}$ ratio measured by AMS.

Bierman *et al.* assumed that ^{36}Cl was produced solely by $^{35}\text{Cl}(n,\gamma)^{36}\text{Cl}$, so they used the $^{36}\text{Cl}/\text{Cl}$ ratio, rather than convert this into a ^{36}Cl concentration. In order to obtain estimates of erosion rates and relative exposure ages from their measurements, Bierman *et al.* derived a neutron stopping rate as a function of depth, including neutrons that were produced by spallation reactions, from fast and slow muon reactions, and radioactive decay of U and Th. The loss of spallogenic and mu-genic neutrons at shallow depths due to the air/ground boundary effect was taken into consideration. While this low-energy neutron flux depth profile wasn't quantitative, the air/ground boundary effect was the same order of magnitude as Liu *et al.* [Liu94].

Bierman *et al.*'s $^{36}\text{Cl}/\text{Cl}$ measurements were reproducible and appeared to be representative of the samples' exposure history. However, because of the complex nature of the $^{35}\text{Cl}(n,\gamma)^{36}\text{Cl}$ production channel near the earth's surface, combined with a complicated geological setting, it was impossible for Bierman *et al.* to determine whether boulder to boulder variability was due to the extraction procedure or the geological nature of the debris-flow fan.

Dep (1995) attempted to isolate the $^{35}\text{Cl}(n,\gamma)^{36}\text{Cl}$ production channel by a different method. He prepared quartz mineral separates which he assumed contained virtually no potassium or calcium, but contained chloride in the fluid inclusions. The quartz mineral separate could then be dissolved and prepared as AgCl , similar to normal ^{36}Cl measurements.

Dep measured a $^{36}\text{Cl}/\text{Cl}$ depth profile in quartz mineral separates prepared from a 60cm drill core from a siliceous dolomite ejecta boulder collected from the Meteor Crater, Arizona. The depth profile is shown in Figure 3.3, with the solid line indicating results from the Monte Carlo model (discussed above), and the dotted line the predicted profile from the concrete block simulation (also discussed above). The measured depth profile is in general agreement with the two models, however, it should be noted that there is a log scale (unlike Figure 3.1) so there is a significant amount of scatter in the results.

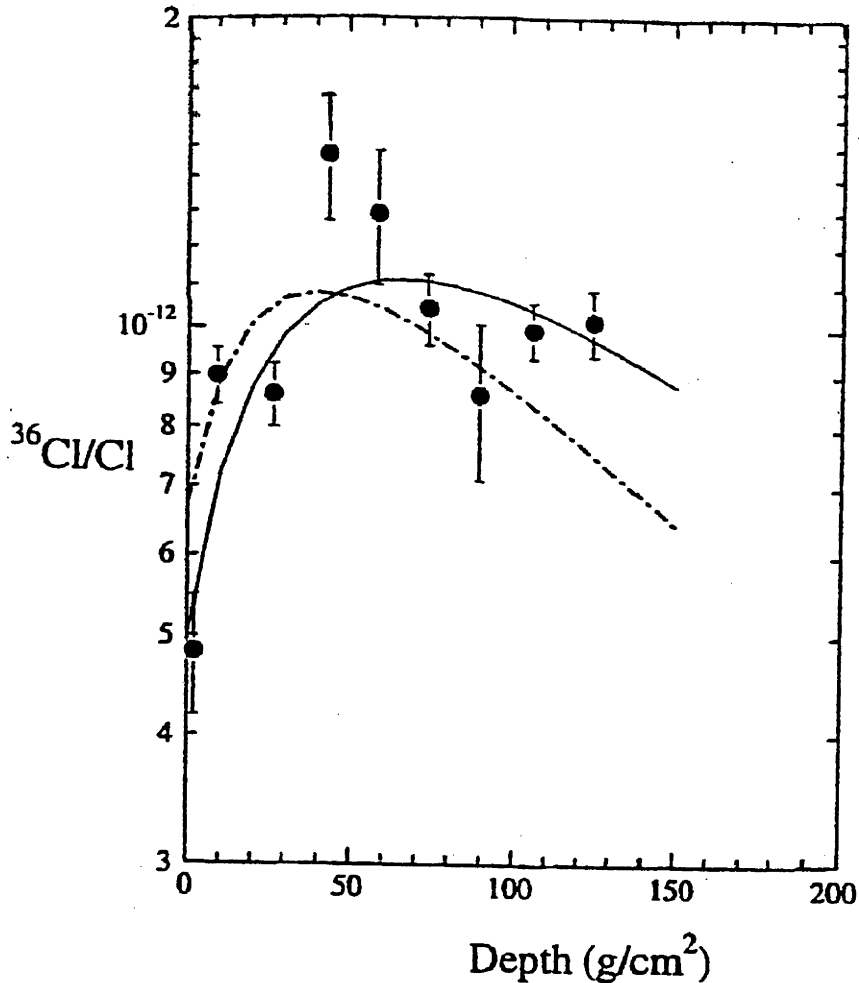


Figure 3.3 Measured and predicted depth dependence of $^{36}\text{Cl}/\text{Cl}$ in quartz mineral separates. The solid line is the predicted profile from a Monte Carlo model and the dotted line is the predicted profile from the concrete block simulation. Adapted from a figure in [Dep95].

While attempts to isolate the $^{35}\text{Cl}(n,\gamma)^{36}\text{Cl}$ production channel by both Bierman *et al* [Bie96] and Dep [Dep95] were not definitive, their work suggests that if the method were refined it would be a very useful way to investigate the ^{36}Cl concentration due solely to the $^{35}\text{Cl}(n,\gamma)^{36}\text{Cl}$ production channel in a particular sample. Comparing results from different samples in a simpler geological setting could provide a very interesting insight into the geological, as well as chemical, dependence of low-energy neutron capture by ^{35}Cl , without these effects being diluted by ^{36}Cl production from potassium or calcium.

3.3 Calibration Strategy adopted in this Study

This section discusses the approach used in this study to improve on the methods used previously.

3.3.1 Well-Constrained Exposure History

A geological calibration of cosmogenic nuclide production rates must be based on samples with well-constrained exposure histories. Samples from two locations were used in this study: 1) surface samples from western Scotland, and 2) a depth profile from Wyangala, south eastern Australia. The exposure history of both locations are discussed below.

Scottish Samples

The glacial histories of Great Britain and North Europe have been extensively studied [Bal94, Sut84]. Many glacial episodes have been recognised during the Quaternary period*, but as later glaciations tend to obliterate evidence of earlier glacial and interglacial periods, the most well constrained episodes are the Loch Lomond Stadial† and the Dimlington Stadial shown in Figure 3.4.

The Dimlington ice sheet covered two thirds of the present land area of Great Britain when it reached its maximum extent between 18,000 and 17,000 ^{14}C year BP. It was the greatest expansion of glacier ice since the Anglian

* The most recent period in geological time, extending from 1.8 million years ago to the present.

† Stadial is the term used for a period when the climate is colder and Interstadial is the term used for a period when the climate is warmer.

Glacial stage that covered most of Great Britain and Northern Europe between c. 480,000 and 430,000 years ago [Ros87].

Following the Dimlington Stadial there was a relatively brief warmer climate (the Windermere Interstadial) before the last glacial episode in Great Britain, the Loch Lomond Stadial, which is the equivalent of the Scandinavian Younger Dryas*. Glaciers re-occupied cirques in the Scottish highlands and a small icecap formed over Rannoch Moor southeast of Ben Nevis.

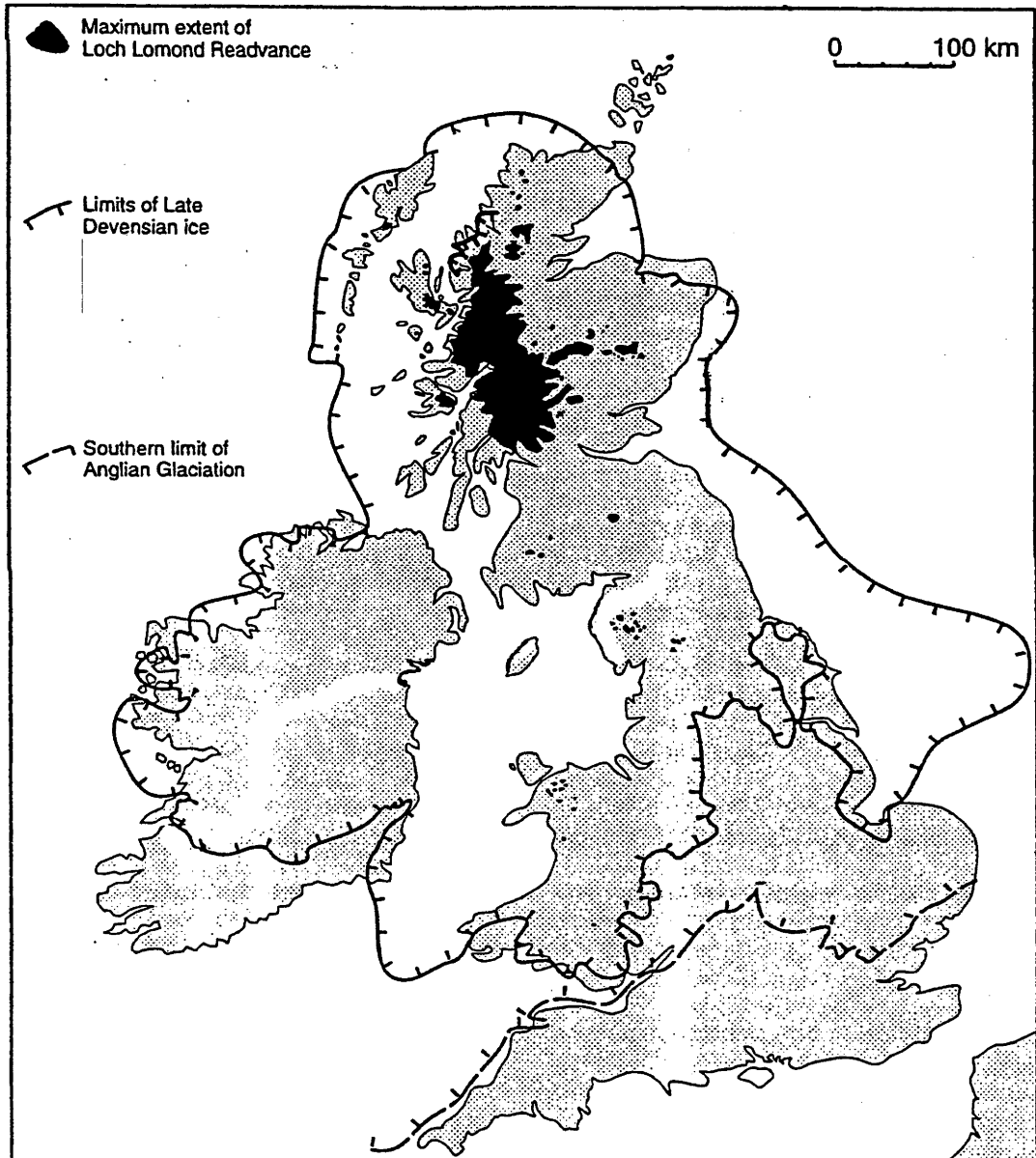


Figure 3.4 Extent of glacial limits in Great Britain and Ireland.

*"Dryas" is a genus of plants whose pollen is found in cores from lakes and bogs during glacial periods. Hence the "Older Dryas" and "Younger Dryas" refer to periods when tundra plants were the dominant vegetation in Scandinavia.

The Loch Lomond Stadial is believed to have been the result of movement of the Atlantic oceanic polar front, which reached its southernmost position off the coast of SW Ireland around 10,200 ^{14}C years BP (11,960 cal. yr BP, [Rud77]). Carbon-14 dates on pre-glacial material underlying and incorporated into Loch Lomond Re-advance till indicate that glaciers reached their maximum extent after 10,900-10,560 ^{14}C yr B.P. (12,940-12,640 cal yr B.P.; [Ros88, Pea89]). The age of deglaciation is loosely constrained by ^{14}C dates from basal organic sediment in peat bogs within the area occupied by Loch Lomond Re-advance glaciers, the oldest of which are ~10,200 ^{14}C yr B.P. (11,960 cal yr [Gra91]). These limits place the re-advance within the Younger Dryas period (13,000-11,600 cal yr B.P.) as defined by ^{14}C dates from Scandinavia, and counted annual layers in the Greenland ice cores. The sample sites were most likely exposed at the end of this period, when mean annual temperatures in Scotland rose from sub-zero to positive values at a rate as high as 1°C per decade [Atk86]. Such abrupt climatic warming would have rapidly melted small cirque and valley glaciers. Another possibility that must be borne in mind, however, is that glaciers withdrew from some sites before the end of the stadial, due to decreased snowfall under the prevailing cold arid conditions [Ben92]. Thus although the age of deglaciation is not independently dated at any of the sites sampled, it is reasonable to assign a value of $11,600 \pm 500$ yr, corresponding to the onset of abrupt warming but allowing latitude for melting and the possibility of early withdrawal.

Two types of surface samples from Scotland were included in the calibration - bedrock samples that would have been first exposed during glacial retreat, and large boulders that fell onto the surface of glaciers just prior to deglaciation.

Bedrock samples were collected where possible; however, many samples were also collected from several glacially transported boulders. Bedrock samples were taken from the downstream side of roches moutonnées[†] to ensure

* From 1989 to 1994 an extensive paleoclimate record for the Northern Hemisphere, termed the Greenland Ice Core Project (GRIP) and Greenland Ice Sheet Project Two (GISP2), was acquired from deep ice cores from on and near the Greenland summit. A wide range of environmental and physical parameters were measured in each of the cores. It has been possible to count annual layers in the GRIP core to obtain excellent dating, particularly back to the Younger Dryas [Gre97].

† A roche moutonnée is a rock mass forming a hillock, which is smooth and rounded, often with striations on the upstream side, and steeper and rougher on the down stream side. It is the product of a glacier going over a hill in the bedrock. As the glacier is pushed up, the pressure on the ice increases, causing the bottom of the glacier to melt. Once the glacier passes the summit of the hill the pressure decreases and the melt water freezes the bedrock to the glacier. The movement of the glacier can then "pluck" large boulders from the bedrock.

that sufficient rock was removed during the glacial episode so that the risk of pre-exposure was minimised. As rock would have been removed by “plucking” rather than “scouring”, glacial striation wouldn’t be expected to be found on the samples themselves. Nevertheless, striations were observed on nearby rock surfaces at many sample locations, implying a negligible erosion rate.

The glacially transported boulders were carefully selected. Only boulders that were located within the limits of the Loch Lomond Readvance were sampled. The fact that they hadn’t reached a moraine implies that the glacier retreated after the boulder fell on it (and cosmic ray exposure began) but before the boulder could reach the moraine. For smaller glaciers a few km in length, as was common in the Loch Lomond glacial period, it would probably take the boulder 100-200 years to travel from the head of the valley to the moraine, given a conservative travelling speed of $\sim 30\text{m/yr}$ [Bou79,Ste83]. Given that the Loch Lomond Readvance ended very rapidly, it can be assumed that the boulders were delivered onto the ice surface <200 years before the end of the Loch Lomond Readvance, so assigning an exposure age of 11,600 years to the samples is quite secure.

Several features were looked for when choosing a glacially transported boulder from which to collect samples.

1. The boulders had to be large (1.5m x 1.5m x 1.5m at a minimum) so that the side of the boulder that was sampled didn’t contain ^{36}Cl from pre-exposure. Large boulders are also less likely to be covered by snow during the winter.
2. The boulders needed to be non-rounded, implying that they weren’t old boulders that were overridden by a Loch Lomond glacier. A rounded boulder would also indicate a higher likelihood of erosion.
3. The boulders needed to be located in a position to which they could not have rolled down from a surrounding hill, in which case they might not be associated with glaciation.
4. The boulders needed to have been overturned when they fell. Dilation joints* on the lower surfaces were sought as evidence of this.

Wyangala Samples

The depth profile was measured in a granite quarry at Wyangala, south eastern Australia ($34^{\circ} 02' \text{ S}$ and $148^{\circ} 55' \text{ E}$, see Figure 3.5). Wyangala is situated

* When an overlying weight is removed, the release of pressure causes the rock to expand and split along expansion or dilation joints in concentric layers at right angles to the direction of pressure release.

in the Lachlan foldbelt which formed along a convergent margin about 400 to 300 Myr ago [Twi00, O'Su00]. The area has undergone a period of weathering and landscape stability for the last ~50 Myr [O'Su00], and this is reflected in the present day landscape which is relatively flat, with little expression of underlying rock.

Using a generous constant erosion rate of $10 \mu\text{m yr}^{-1}$, the spallation portion of the ^{36}Cl concentration would reach steady state in the whole profile in ~0.2 Myr. As the negative muon capture portion has a lower production rate, it would take ~1 Myr. Consequently, it can be very safely assumed that the region has been stable for a sufficient amount of time. However, it is harder to provide evidence that the erosion rate has remained constant over such a long period. The Wyangala area is eroding by exfoliation, where the surface is lowered by the removal of successive slabs, which is a common characteristic of granite weathering*. For this present work, it can only be said that there is no evidence that the erosion rate has changed significantly in the last ~1 Myr, and a continuous long term erosion rate is assumed.

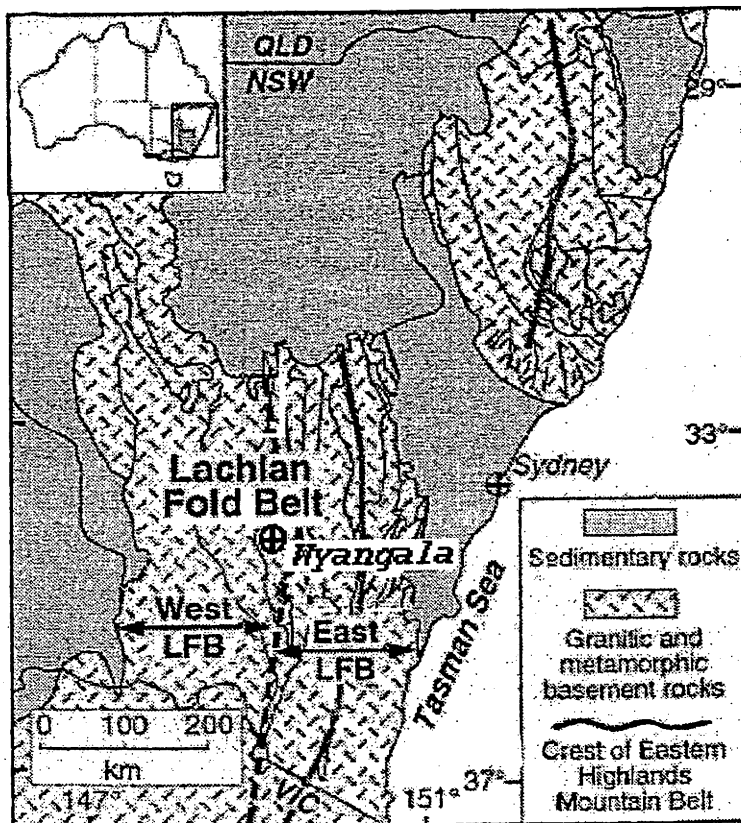


Figure 3.5 The location of Wyangala.

* A continuous long term erosion can be assumed as long as the thickness of the slabs being removed is significantly less than the fast neutron attenuation length, Λ_{sp} , or ~60 cm in granite [Lal91].

3.3.2 Potassium Concentration

Chlorine-36 measurements were performed on pure K-feldspar mineral separates with potassium concentrations of typically ~11 %K. These were low in calcium (0.03-2.00 %Ca) minimising its contribution to production of ^{36}Cl . Chloride concentrations varied from 17.5 ppm up to 275 ppm. In the case of low-Cl samples, neutron-capture production is also minimal compared to production from potassium. In the high-Cl samples, which included most of the K-feldspar derived from Torridon Sandstone in Scotland, neutron capture production was high enough to warrant a separate calibration (Chapter 5).

Previous calibrations have assimilated ^{36}Cl production from spallation of Ti and Fe into the production rates assigned to Ca, K and ^{35}Cl reactions. Although contributions from Ti and Fe are expected to be small, calibration based on pure minerals such as K-feldspar, that contain virtually no Fe or Ti, avoids this problem. Contributions from these elements have most likely been attributed to Ca in previous calibrations based on whole-rock samples, which relied largely on Fe-, Ti-rich basalt samples to determine the production rate from Ca [Zre91, Swa94, Phi96]. This may partly explain discrepancies between existing estimates of the production rate from Ca reactions (see Table 3.1).

3.3.3 Analysis Strategy

The calibration was approached from three perspectives:

1) The ^{36}Cl concentration in 18 surface K-feldspar mineral separates from Scotland were measured to constrain the value of the potassium spallation production rate, $P_{\text{sp,K}}(0)$.

2) The ^{36}Cl concentration in 8 surface quartz mineral separates from Scotland were measured to constrain the value of the production rate of spallogenic secondary neutrons in the air directly above the ground, $\mathcal{P}_i(0)$.

3) The ^{36}Cl concentration was measured in 16 K-feldspar mineral separates in a depth profile from Wyangala, Australia. These samples were used to constrain the ^{36}Cl yield per stopped negative muon, Y_{μ^-} . As even small erosion rates can have a large effect on steady state concentrations, it was necessary to also allow the erosion rate, ϵ , to be a free parameter in the fit to the depth profile.

It was assumed that the Scottish samples were unaffected by erosion (see Appendix C for a discussion on this assumption). Therefore their ^{36}Cl

concentration is described by the general Equation 2.2, for the accumulation of ^{36}Cl in a static surface. By substituting for all the ^{36}Cl production channels, the ^{36}Cl concentration in a static surface as a function of time is given by the following:

$$\begin{aligned}
 N_{\text{total}}(0) = & \frac{(1 - e^{-\lambda t})}{\lambda} \times \{ P_{K,sp}(0) \times [K] + P_{Ca,sp}(0) \times [Ca] && \text{spallation} \\
 & + (Y_K \times [K] + Y_{Ca} \times [Ca]) \times \Psi_{\mu^-}(0) && \text{negative muon capture} \\
 & + (f_{35} + f_{39}) \times \mathcal{P}_f(0) \times (k_1 + k_2) && \text{spallogenic thermal neutrons} \\
 & + (f_{epi,35} + f_{epi,39}) \times \mathcal{P}_f(0) \times (k_1 + k_2) && \text{spallogenic epithermal neutrons} \\
 & + (f_{35} + f_{39}) \times Y_s \times \Psi_{\mu^-}(0) && \text{mu-genic neutrons} \\
 & + (f_{35} + f_{39}) \times 7.75 \times 10^{-6} \times Y_f \times \Phi_{\mu^\pm} \} && \text{photonuclear neutrons} \\
 & + (f_{35} + f_{39}) \frac{P_{n,U+Th}}{\lambda} && \text{radiogenic neutrons}
 \end{aligned}
 \tag{3.2}$$

The Wyangala samples with a long exposure time are affected by erosion, so their ^{36}Cl concentration is described by Equation 2.4, which is the general differential equation appropriate for the accumulation of an *in-situ* cosmogenic nuclide over time at depth z with a surface erosion rate of ϵ . By solving Equation 2.4 and summing over all the ^{36}Cl production channels, the ^{36}Cl concentration as a function of erosion, depth and exposure time can be determined, giving the following result:

$$\begin{aligned}
 N_{\text{total}}(z, \epsilon) = & \frac{(P_{K,sp}(0) \times [K] + P_{Ca,sp}(0) \times [Ca]) e^{-z/\Lambda_w}}{(\lambda + \rho\epsilon / \Lambda_{sp})} && \text{spallation} \\
 & + (Y_K \times [K] + Y_{Ca} \times [Ca]) \times \int_0^{\infty} \Psi_{\mu^-}(z + \epsilon t) e^{-\lambda t} dt && \text{negative muon capture} \\
 & + (f_{35} + f_{39}) \times \mathcal{P}_f(0) \times \left(\frac{k_1 e^{-z/\Lambda_w}}{\lambda + \rho\epsilon / \Lambda_{sp}} + \frac{k_2 e^{-z/L_{th}}}{\lambda + \rho\epsilon / L_{th}} \right) && \text{spallogenic thermal neutrons} \\
 & + (f_{epi,35} + f_{epi,39}) \times \mathcal{P}_f(0) \times \left(\frac{k_3 e^{-z/\Lambda_w}}{\lambda + \rho\epsilon / \Lambda_{sp}} + \frac{k_4 e^{-z/L_{epi}}}{\lambda + \rho\epsilon / L_{epi}} \right) && \text{spallogenic epithermal neutrons} \\
 & + (f_{35} + f_{39}) \times Y_s \times \int_0^{\infty} \Psi_{\mu^-}(z + \epsilon t) e^{-\lambda t} dt && \text{mu-genic neutrons} \\
 & + (f_{35} + f_{39}) \times Y_f \times 7.75 \times 10^{-6} \times \int_0^{\infty} \Phi_{\mu^\pm}(z + \epsilon t) \ln(0.1065(z + \epsilon t)) e^{-\lambda t} dt && \text{photonuclear neutrons} \\
 & + (f_{35} + f_{39}) \frac{P_{n,U+Th}}{\lambda} && \text{radiogenic neutrons}
 \end{aligned}
 \tag{3.3}$$

The calibration was approached from three perspectives. First, the quartz samples from Scotland were considered to determine $\mathcal{P}_f(0)$, as they were the least dependent on the other unknown quantities. The minimisation was performed by calculating the ^{36}Cl concentration for the quartz samples using Equation 3.2 and adjusting the value of $\mathcal{P}_f(0)$ to minimise the χ^2 sum over the samples:

$$\chi^2 = \sum \frac{(N_{\text{meas}} - N_{\text{total}})^2}{(\sigma_{\text{meas}})^2} \quad (3.4)$$

where N_{meas} and σ_{meas} are the measured ^{36}Cl concentration and uncertainty respectively.

Knowing the value of $\mathcal{P}_f(0)$ it was then possible to deduce $P_{\text{K,sp}}(0)$ from the Scottish K-feldspar samples. Again using Equation 3.2, $P_{\text{K,sp}}(0)$ was adjusted to minimise the χ^2 sum over the Scottish K-feldspar samples.

Finally, the depth profile was investigated. First, the value for the erosion rate above the profile was constrained by substituting the values for $\mathcal{P}_f(0)$ and $P_{\text{K,sp}}(0)$ and an approximate estimation of Y_{K} into Equation 3.3, with subsequent adjustment of ε to minimise the χ^2 sum over the surface depth profile samples. The values for the ^{36}Cl yield per stopped negative muon were then constrained by substituting the values for $\mathcal{P}_f(0)$, $P_{\text{K,sp}}(0)$ and ε into Equation 3.3, and subsequent adjustment of Y_{K} to minimise the χ^2 sum over the whole depth profile.

To ensure the best possible results, the above procedure was repeated iteratively over the Scottish quartz, the Scottish K-feldspar and the Wyalanga K-feldspar samples, until the values of $\mathcal{P}_f(0)$, $P_{\text{K,sp}}(0)$, Y_{K} and ε remained unchanged. This iterative procedure was used in preference to a global minimisation as the measured ^{36}Cl concentration for the quartz samples had uncertainties of 10-15%, compared to ~5% for the K-feldspar samples. Consequently the K-feldspar samples had an undue effect on the value of $\mathcal{P}_f(0)$.

While the above shows that the values for $\mathcal{P}_f(0)$, $P_{\text{K,sp}}(0)$, Y_{K} and ε are inter-related, they will be discussed separately for simplicity. The value determined for $\mathcal{P}_f(0)$ and the Scottish quartz samples are discussed in Chapter 5. The value determined for $P_{\text{sp,K}}(0)$ and the Scottish K-feldspar samples are discussed in Chapter 6, while the depth profile and the values for Y_{K} and ε are discussed in Chapter 7.

Chapter Four

METHODOLOGY

A comprehensive chemical analysis is required for each *in-situ* ^{36}Cl sample. Determination of the ^{36}Cl contribution from the spallation and negative muon capture reactions requires that the potassium, calcium, chloride and ^{36}Cl concentrations be measured in each mineral separate. The density of the rock must also be measured in order to determine the attenuation rate of the secondary cosmic rays. To calculate the ^{36}Cl production by thermal neutron capture on ^{35}Cl (or ^{39}K) the major elements (SiO_2 , TiO_2 , Al_2O_3 , Fe_2O_3 , MnO , MgO , CaO , Na_2O , K_2O and P_2O_5) and important trace elements for neutron absorption and emission (B, Gd, Sm, U and Th) must also be measured in the whole rock portion of each sample.

4.1 Sample Collection

As AMS measurements become more and more routine, it is often the choice of samples that determines the success of a study. This section discusses some of the important general features required of a sample for a production rate calibration. Much of this also applies to samples collected to determine exposure ages and erosion rates. Detailed discussion of the sample locations from which samples were collected for this study will be provided where appropriate in the following chapters.

4.1.1 Surface Samples

The first requirement of a production rate calibration sample is that the exposure age should not need to be calibrated. There are two types of samples that satisfy this requirement: 1) a sample from a surface that has been exposed by an event whose timing has been precisely determined, and 2) a sample from a surface that is known to be old enough that isotopic steady state can be assumed, negating the need to know the exposure age of the surface. Both types of samples have advantages and disadvantages. The advantages of choosing a young surface include:

- i) A wider range of rock types and geological situations, and
- ii) The likelihood of a simple exposure history, for which erosion, burial or snow cover can be ruled out.

The disadvantages of a young surface are:

- i) The calibration is completely dependent on the reliability of the measurements determining the surface age.
- ii) The sample will be sensitive to pre-exposure. Enough needs to be known about the event that brought the sample to the surface to be confident that it was previously shielded from penetrating cosmic rays (such as muons).
- iii) Finally, the cosmogenic nuclide concentration may be low enough to make for a challenging high precision AMS measurement.

For a sample at steady state, the advantages are:

- i) factors such as surface exposure age and pre-exposure cease to be important.
- ii) Sample will have a very high cosmogenic concentration, so the precision of the AMS measurement can be maximised.

The disadvantages of using a sample at steady state are:

- i) The sensitivity of the calibration to the preservation of the surface. Even a low erosion rate can have a large effect on the accumulation of cosmogenic nuclides in an old surface.
- ii) There is more chance of snow or soil cover, or even vertical tectonic movement (changing the sample's altitude), that may be undetected.
- iii) The main disadvantage of attempting to use samples at steady state is that suitable locations are extremely rare, with rock outcrops in the Antarctic being the most promising candidates [Nis91a].

However, failure to have reached steady state, erosion, burial, snow cover and tectonic uplift all reduce the cosmogenic nuclide accumulation, so that calibrations based on ancient surfaces tend to provide firm lower limits to production rates.

4.1.2 Depth Profile

There are two ways of sampling a depth profile: (1) to drill a core in bedrock, and (2) to make use of a man-made rock profile, such as a road cutting or a rock quarry. In the prior case it is much easier to determine the integrity of the surface (applying all the criteria of a surface sample), but it is more difficult to obtain complete cores greater than a metre in length. Typically the top of the cores are crushed, which adds uncertainty to the depth measurements.

Samples from a road cut or quarry are generally easier to obtain and the distance from the surface is easy to measure. It is, however, much harder to determine if rock or soil has been removed from the original surface as the result of the road works or quarrying. The integrity of the surface, however, can be confirmed by collecting and measuring surface samples from the surrounding area. This was the method adopted in the present work.

4.2 Chemical Preparation of Samples

After noting dimensions and other physical characteristics, samples were thoroughly cleaned and crushed in a jaw crusher, then sieved into grain size fractions between 75 microns and 450 microns. The smaller grain sizes were used for whole-rock chemical measurements, the larger grain sizes were used for mineral separation. Prior to mineral separation the samples were cleaned in an ultrasonic bath and boiled in 10% nitric acid to remove fine grained powder and carbonate and oxide weathering products.

4.2.1 Mineral Separation: K-feldspar and Quartz

K-feldspar was separated from quartz and plagioclase by flotation in an ethylene bromide-acetone solution at a density of 2.58 g cm^{-3} . The purity of the

mineral separates was checked under a polarizing microscope, and in general the heavy liquid separation was sufficient to obtain better than 95% pure K-feldspar.

Quartz samples were obtained by selective etching in dilute HF [Koh92]. Some of the mineral separates required an additional purification by a combination of flotation in an ethylene bromide-acetone solution at a density of 2.68 g cm^{-3} , and use of a Frantz magnetic separator to remove magnetic minerals.

To ensure that there was no meteoric ^{36}Cl left from the original sample or introduced during the mineral separation, the mineral separates were leached twice in hot 10% nitric acid and then rinsed several times in deionised water.

4.2.2 AgCl Preparation

To measure the $^{36}\text{Cl}/\text{Cl}$ ratio by AMS, chloride was extracted from the mineral separates and precipitated as AgCl. This is the preferred chemical form for the AMS ion source. During the preparation, extra steps were included to remove sulfur from the AgCl, as ^{36}S greatly interferes with the ^{36}Cl measurement (see § 4.3). The procedure used was based on Conard *et al.* [Con86] and Zreda *et al.* [Zre91], with adaptations made by Dr John Stone. A brief summary is given below, concentrating on values and noteworthy aspects specific to this work. Except where noted, the procedure is the same for quartz and K-feldspar mineral separates.

The clean mineral separates were weighed and transferred into 500 ml Teflon bottles. Sample sizes were typically 10 g; however, they ranged from 26 g for the depth profile samples, to 6.5 g for repeat measurements of some Scottish samples. Carrier containing ~1 mg of chloride was added to the K-feldspar mineral separates for two reasons; firstly to ensure that there was sufficient AgCl to make a measurement, and secondly to minimise the effect of uncertainty in the chloride measurement. (Since the establishment of the isotope dilution method of measuring chloride, discussed below, the latter reason is largely redundant and in the future the need to add chloride carrier will not be as pronounced.) The carrier was made up from Weeks Island Halite and has a $^{36}\text{Cl}/\text{Cl}$ ratio below the present detection limit of the AMS system which is 4×10^{-16} .

When small amounts of AgCl were precipitated from large volumes of solution (≥ 400 ml) it was found that yields were very poor. Therefore, for some of the quartz mineral separates, which were processed without addition of chloride carrier (see Appendix A), ~ 0.25 ml of NaBr was added so that AgBr would also be precipitated with the AgCl which made collecting the precipitate easier.

It should be noted that while the addition of Br carrier or the Cl carrier is often essential in order to obtain sufficient final precipitate, they both have a slightly negative effect on the AMS measurement. The addition of chloride carrier reduces the $^{36}\text{Cl}/\text{Cl}$ ratio, while the addition of NaBr reduces the chloride concentration, and therefore produces lower ^{35}Cl , ^{36}Cl and ^{37}Cl beams. In general, however, this is only an issue for samples that start with a low ^{36}Cl concentration.

The K-feldspar mineral separates were dissolved in 3.5 ml conc. HF and 6 ml 2N HNO_3 for each gram of sample. Quartz mineral separates were dissolved in 5 ml conc. HF and 10 ml 1N HNO_3 per gram of sample. Once the initial heat of the reaction had subsided the samples were heated gently, for 24 to 48 hours. The bottles were never allowed to boil to avoid possible loss of volatile HCl or Cl_2 .

During dissolution of the K-feldspar mineral separate, a fluoride gel was produced (quartz dissolved completely and the solution was transferred directly). This was centrifuged off and the solution was quantitatively transferred to a Teflon beaker, along with several rinses of the fluoride gel. The solution was then heated and ~ 1 ml of 10% AgNO_3 was added to precipitate AgCl. Ag_2SO_4 also precipitates at this stage. Convection of the hot solution aided precipitation and flocculation. The precipitate was then collected and rinsed.

The separation of sulfur from the chloride was performed by dissolving the precipitate in 2 ml 1:1 NH_3 , transferring to a glass tube, and adding 1 ml of saturated BaNO_3 solution. After diluting to ~ 40 ml, the ammoniacal solution was left for a minimum of 24 hours for BaSO_4 to precipitate. After centrifuging the precipitate, the chloride remaining in solution could be pipetted out.

Additional AgNO_3 was added, the solution was heated and then acidified to precipitate clean AgCl. AgCl was collected by centrifuging, then dried and pressed into sample holders, ready for measurement on the accelerator.

Procedural blanks were prepared with every batch of 7 samples. The average blank $^{36}\text{Cl}/\text{Cl}$ ratio was $(1.7 \pm 1.2) \times 10^{-15}$, which is equivalent to $(2.8 \pm 2.0) \times 10^4$ atoms of ^{36}Cl . The procedural blanks were used to make a ^{36}Cl blank correction

to that batch of samples. In addition, the chloride was measured in the chemicals used in the AgCl preparation so that a chloride correction could also be made to the $^{36}\text{Cl}/\text{Cl}$ value measured for each sample. The principal source of chloride was from the HF, which was measured by isotope dilution to be $0.094 \mu\text{g Cl}^- (\text{ml HF})^{-1}$. Given that 5 ml of conc. HF per gram sample was used in the dissolution, the chloride correction was typically of the order of $5 \mu\text{g Cl}^-$.

The AgCl sample sizes ranged from ~3 mg to 18.5 mg. The average yield, determined by weighing the final AgCl precipitate, was 84% for the high chloride samples and 59% for the low chloride samples.

4.2.3 Major Element and Trace Element Composition

Potassium concentration measurements were performed by flame photometry using methods developed at ANU for K-Ar dating [Coo66], with accuracy and precision better than $\pm 1\%$.

To determine the percentage of ^{36}Cl produced from calcium (which should be minimal if the mineral separation is good), the calcium concentration in the Wyangala K-feldspar mineral separates was measured by Inductively Coupled Plasma-Optical Emission Spectroscopy (ICP OES). As the calcium concentrations were very low ($<0.3\%$ Ca), the measurement uncertainty was high, $\sim 20\%$. However, as the ^{36}Cl contribution from calcium was $<1\%$ of the total ^{36}Cl concentration, this had a negligible effect on the calibration.

The major element composition (SiO_2 , TiO_2 , Al_2O_3 , Fe_2O_3 , MnO , MgO , CaO , Na_2O , K_2O and P_2O_5) of all samples was measured by X-ray fluorescence (XRF).

Finally, the abundance of trace elements important in low-energy neutron production and absorption (B, Gd, Sm, U and Th) were measured by Inductively Coupled Plasma - Mass Spectrometry (ICP-MS) and neutron-induced prompt gamma spectroscopy. Prompt gamma analyses were used to check inexplicably high B concentrations in one set of Scottish samples. After confirming that the prompt gamma method gave results in acceptable agreement with ICP-MS analyses for Gd, and for B in selected Wyangala samples, it was noted that prompt gamma results for the Scottish samples were almost exactly half the values obtained by ICP-MS. It appears that a standardisation error in the ICP-MS B

analyses (either a typographical error or loss of boron from the rock standard preparation) caused the problem. Boron analyses from this run were reduced by a factor of 2.

Initial ICP-MS values for uranium and thorium in the Wyangala samples were also high and erratic, which was attributed to either a “nugget” effect involving U-Th bearing minerals in the granite, or incomplete dissolution of these minerals in some of the samples and standards. As a result, all the different grainsize fractions for a sample were re-combined and a 30g sample was then taken as a representative sample of the whole rock. This was then crushed down to a fine powder in a Tema Mill and analysed for uranium and thorium by XRF. This greatly reduced the scatter in the uranium and thorium numbers, and brought them into good agreement with other uranium and thorium analyses of rocks from the Wyangala Pluton [Cha97]. Three Scottish samples were also re-analysed for uranium and thorium by XRF, and gave results in good agreement with the ICP-MS values.

4.3 Accelerator Mass Spectrometry

Accelerator Mass Spectrometry (AMS) is a process that uses nuclear techniques to measure extremely low isotope ratios. The techniques used by AMS have evolved over the last two decades, as the number of measurable isotopes and fields of application, have increased. In addition to earth sciences, applications include archeology hydrology, meteorology, biochemistry, medicine and radioactive waste management.

AMS is not a single technique. Every isotope has different problems that need to be resolved, and the solutions often vary from lab to lab [Fif99]. A complete discussion of AMS techniques is far beyond the scope of this dissertation. Instead, the discussion will be limited to the measurement of ^{36}Cl at the Australian National University prior to 1999, during which time all measurements for this work were made. (From 1999 onwards a new ion source was used routinely for ^{36}Cl measurements, which increased beam currents and as a result changed many of the parameters mentioned below.)

The ANU tandem accelerator, shown in Figure 4.1, is one of the highest energy accelerators used for AMS, and one of the few that is still also used extensively for nuclear physics research. The high energies obtainable make it ideal for isotopes that require separation from an interfering isobar, such as ^{36}S in the case of ^{36}Cl analyses.

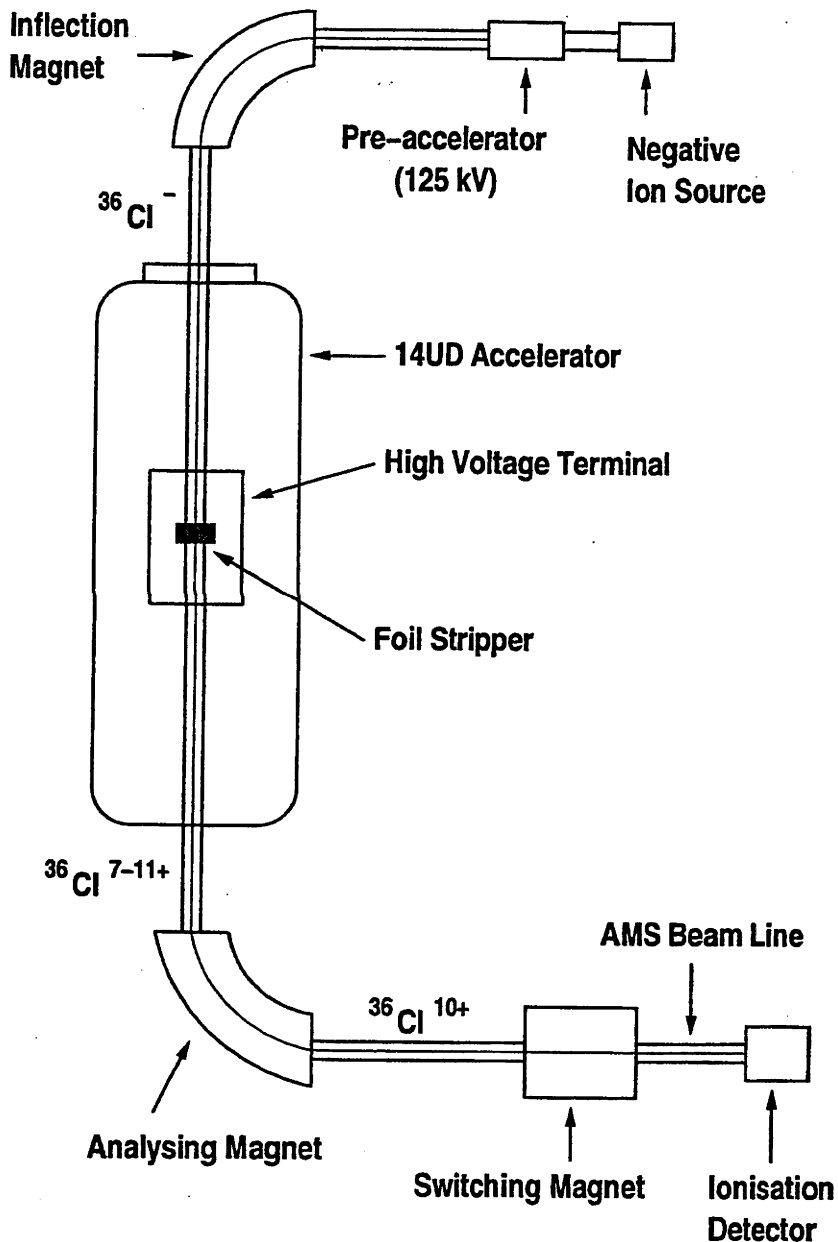


Figure 4.1 Schematic diagram of the ANU 14UD tandem accelerator.

The prepared AgCl samples were pressed into a AgBr substrate which was in turn pressed into a copper sample holder. The role of the AgBr was to reduce the interference of ^{36}S ions, as commercial copper has been found to contain much higher levels of sulfur than AgBr. The sample holder was placed into the ion source and a Cl^- ion beam was produced by cesium sputtering. The ions were accelerated by a 128 kV potential to the inflection magnet which selected the mass/charge ratio of the ions. For the measurement of ^{36}Cl , a mass of 36 and a charge of -1 were selected. This also transported $^{36}\text{S}^-$, $^{12}\text{C}_3^-$, and $^{18}\text{O}_2^-$.

The negative ions were accelerated toward the positive terminal of the accelerator where electrons were stripped off the ions as they passed through a carbon foil. Passage through the foil also dissociated molecular ions into their component atoms, effectively eliminating interference from $^{12}\text{C}_3^-$, and $^{18}\text{O}_2^-$.

From the terminal, the ions (in charge states between predominantly +6 and +11) were further accelerated to the larger analysing magnet at the base of the accelerator which is set to select $^{36}\text{Cl}^{10+}$ ions with an energy of 154 MeV. This magnet is kept at a constant magnetic field. Periodically (approximately every 10 min), ^{35}Cl and ^{37}Cl ions are sent through the accelerator to a Faraday cup in front of the heavy ion detector. This is accomplished by varying the inflection magnet and terminal voltage. To measure ^{36}Cl the terminal voltage is set to 14.00 MV. To measure ^{35}Cl and ^{37}Cl , the terminal voltage is set to 14.40 MV and 13.63 MV respectively.

Chlorine-36 is measured in the heavy ion detector (see Figure 4.2) which separates the isobars by measuring the energy lost by the ions during collisions with propane molecules [Lit87, Fif94, Fif99]. The propane gas is ionised by the collisions with the high energy heavy ions and an electric potential inside the detector causes the electrons to drift to the upper (anode) plate and the positive propane ions to the bottom (cathode) plate. There are several anode plates and the electrons are light enough to move to the plate directly above where they were produced. It is therefore possible to measure the energy lost by the high energy ion under that plate. The cathode measures the total energy of the high energy ions. Isobars with the same ionic charge state have the same total energy, but the rate they lose energy is dependent on the atomic number Z. The isobar with the

higher Z travels a shorter distance through the detector and loses more energy under the first plates and less under the later ones.

The energy signals are recorded to disk for each ion entering the detector. Subsequent off-line sorting of the data is performed by comparing histograms of one parameter versus another (see for example, Figure 4.3). Specific ions are grouped together in these spectra and gates are placed around groups of ions to discriminate between the ions. A contaminating ion with a wayward path through the detector may have the right energies to appear in the ^{36}Cl gate in one of the spectra, however, it will fall outside the ^{36}Cl gates in the others. Only those ions which fall in all three gates will be included in the ^{36}Cl count. By this processes, ^{36}Cl can be completely separated from ^{36}S as long as the ^{36}S count rate is less than ~5 kHz (see Figure 4.3). The ^{36}S count rate for samples used in this work, however, were typically less than 200 Hz, allowing ^{36}S to be easily separated out.

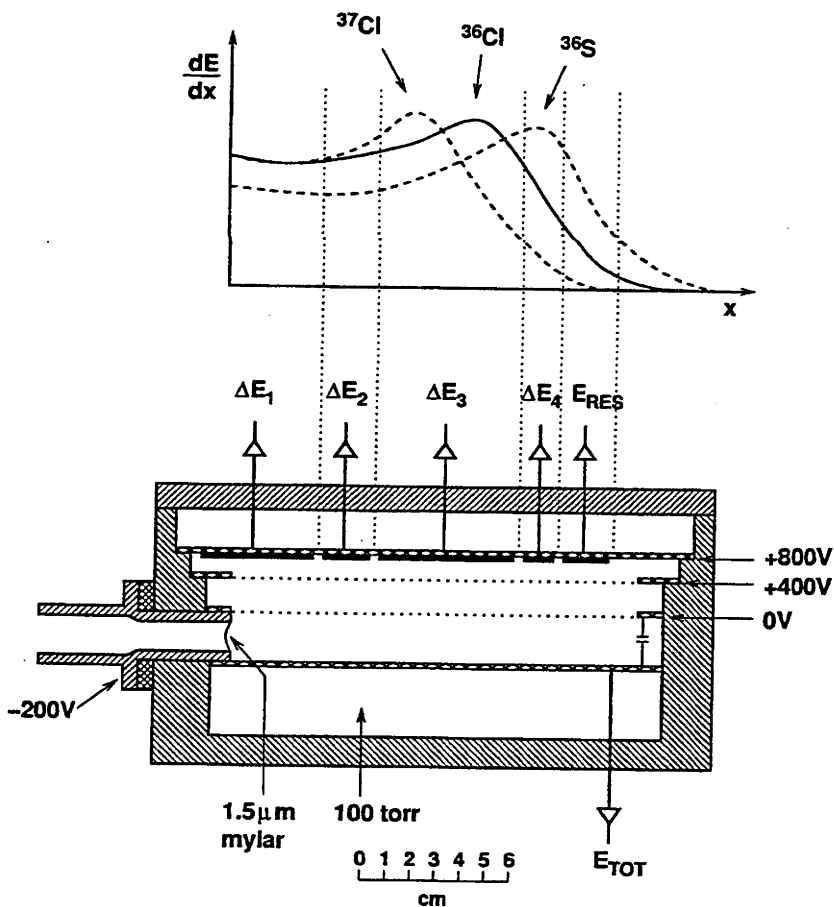


Figure 4.2 Schematic diagram of the heavy ion detector used for $^{36}\text{Cl}/\text{Cl}$ measurements at ANU.

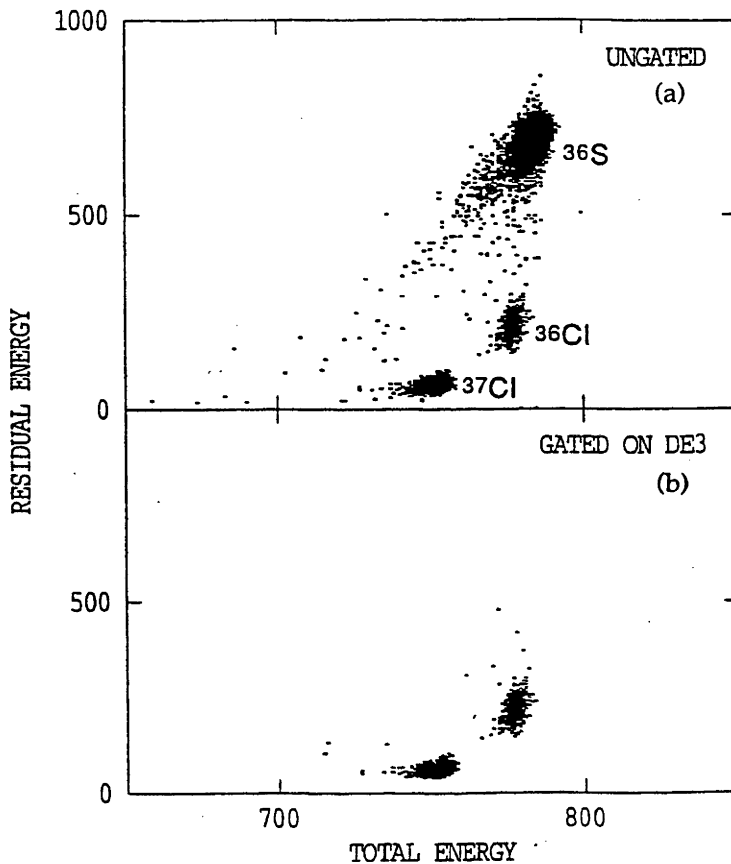


Figure 4.3 The ungated spectra (a) and the gated spectra (b) of the Residual Energy vs Total Energy measured in the heavy ion detector.

Twelve sample holders could be loaded into the ion source at one time. These typically comprised 11 samples and one in-house standard. The overall measurement uncertainty (excluding counting statistics) is <3% from the long term reproducibility of the in-house standard. However for samples with $^{36}\text{Cl}/\text{Cl}$ ratios less than $\sim 2 \times 10^{-13}$, the counting statistics dominate the measurement uncertainty.

4.4 Chloride Measurements

Chloride is an intrinsically difficult element to measure accurately in silicate rocks. An accurate chloride measurement, however, is crucial to distinguish between the production of ^{36}Cl from potassium and the production due to low-energy neutron capture on ^{35}Cl . In addition, the chloride concentration is needed

to determine the ^{36}Cl concentrations from the $^{36}\text{Cl}/\text{Cl}$ ratio obtained by the AMS measurement. Originally pyrohydrolysis was investigated as a method for determining the chloride concentration. This was found to give unreliable results and was replaced by isotope dilution.

4.4.1 Pyrohydrolysis

Chloride measurements in silicate rocks by pyrohydrolysis is described by Evans *et al.* [Eva80, Eva81]. The sample is placed in a ceramic crucible with copper accelerator, iron accelerator and V_2O_5 , and then heated in an induction furnace to greater than 1000°C . At these temperatures, the sample melts and the chloride is released with the other volatile gases. These were transported by oxygen saturated with steam into a container filled with a basic solution ($\text{NaHCO}_3/\text{Na}_2\text{CO}_3$). This was then analysed for chloride by ion chromatography. After each sample was run an empty graphite crucible was heated in the furnace to purge the collection system for 10 min into the collection bottle. To test the effectiveness of the purges, a second purge was often performed into a new collection bottle to measure any residual chloride.

Evans *et al.* [Eva80] reported a one standard-deviation precision of $\pm 5\%$. We were not able to obtaine such a good reproducibility for our results. One sample was measured nine times by pyrohydrolysis (see Figure 4.4). The values obtained ranged from 185 ppm to 368 ppm but tended to clump around 315 ppm. This was believed to be the chloride concentration prior to an isotope dilution measurement, which showed the chloride concentration was indeed 365 ppm. Therefore all but one of the 9 measurements produced yields that were significantly less than 100%. This makes pyrohydrolysis unsuitable for anything but determining a lower limit on the chloride concentration, which was not sufficient for this work.

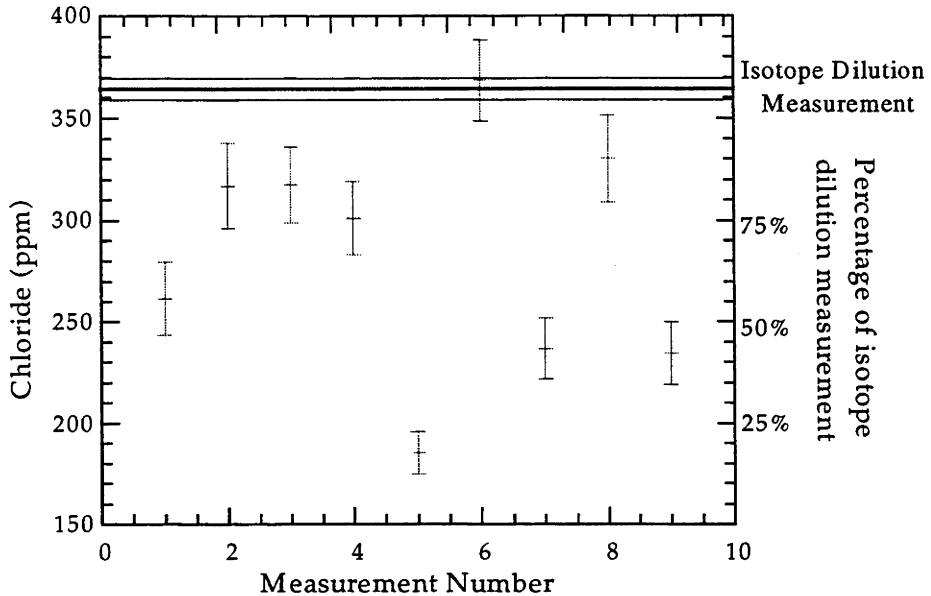


Figure 4.4 Sample ML-1 was measured nine times by pyrohydrolysis, giving a range of values from 185 to 368 ppm. An isotope dilution measurement showed that the concentration was indeed 365 ppm. This demonstrates the degree to which our pyrohydrolysis results were non-reproducible.

4.4.2 Isotope Dilution

The principle of isotope dilution is the determination of the chloride concentration by measuring the change in the natural $^{35}\text{Cl}/^{37}\text{Cl}$ ratio induced by adding a known amount of ^{37}Cl spike. After spiking, the method is insensitive to variations in chemical yield. Up to 1 g of sample was prepared as AgCl, as described in Section 4.2.2, with the exception that it was spiked with a mixture of 30-40 micrograms of ^{37}Cl tracer (either 94.0% or 98.0% enrichment) and 0.5 mg of Br (as NaBr), and the sulfur clean up steps were left out.

The chloride isotope ratio of the final AgCl + AgBr sample was then measured accurately at a Faraday Cup at the low energy (LE) end of the accelerator. Negative Cl beams from the mixed Cl-Br samples are typically 0.2-1.0 microamp, measured at the LE faraday cup after magnetic separation by the inflection magnet. Analyses of normal Cl give $^{35}\text{Cl}/^{37}\text{Cl} = 3.07\text{-}3.17$ (compared to the accepted value of 3.127), but are stable to better than $\pm 1\%$ on a given day. The procedural blank is 1.9 ± 0.2 microgram of Cl (0.6 from HF, 1.3 from added NaBr). The concentration of the ^{37}Cl spike solution was established to better than $\pm 1\%$ by

analysis of gravimetric NaCl solutions. Overall external precision is ± 1 ppm Cl for samples with concentrations < 20 - 30 ppm Cl, and ± 1 - 2% for samples with higher concentrations, based on propagated errors and duplicate analysis of samples with $5 - 300$ ppm Cl. In the course of this work, 11 chloride measurements were made on sample with chloride concentrations ranging from 17 ppm to 267 ppm. As shown in Figure 4.5 the reproducibility of these measurements is excellent.

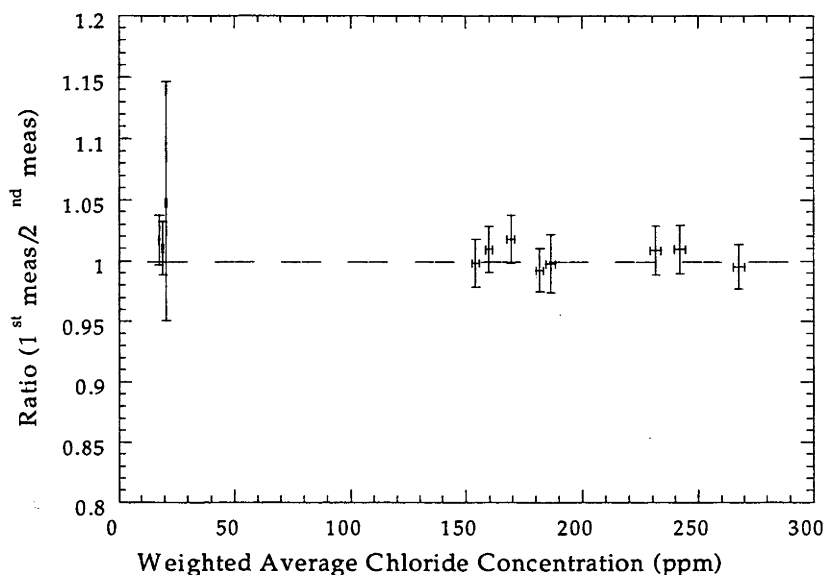


Figure 4.5 Repeat isotope dilution measurements. The chloride concentrations ranged from 17 ppm to 267 ppm. Included on the plot is the errors for each measurement. The $1:1$ agreement between the measurements can clearly be seen.

Chapter Five

^{36}Cl PRODUCTION DUE TO LOW-ENERGY NEUTRON CAPTURE: SCOTTISH QUARTZ MINERAL SEPARATES

The chief aim of this work was to calibrate the production of ^{36}Cl due to potassium. Ideal samples would have high potassium concentrations and low calcium and chloride concentrations. A low calcium concentration can almost always be achieved by sampling a suitable rock type and extracting a particular mineral. However, the chloride concentration is often a characteristic of a rock outcrop, rather than a steadfast trait of a type of rock or mineral. This was the case for the Scottish Torridon Sandstone samples, and as a result, high K/Cl ratios could not be obtained by selection in the field or mineral separation in the lab and it became necessary to find a way to calibrate or correct for the neutron-produced ^{36}Cl . This chapter will discuss how the low-energy neutron capture reaction on ^{35}Cl is accounted for in this study. This is one of the largest challenges in determining the ^{36}Cl production rate from potassium.

5.1 Isolating the ^{36}Cl Produced by Low-Energy Neutron Capture on ^{35}Cl

The work by Bierman *et al.* [Bie94] and Dep [Dep95] (see §3.2.3) demonstrated that ^{36}Cl produced by low-energy neutron capture on ^{35}Cl can be

physically isolated from the spallogenic or muon-produced ^{36}Cl by removing the chloride in the rock sample either by crushing the sample, or by mineral separation. The fraction of ^{36}Cl produced by low-energy neutron capture on ^{35}Cl can then be determined by measuring the $^{36}\text{Cl}/\text{Cl}$ ratio of the chloride (with minor corrections for blank, and any Ca- and K-derived ^{36}Cl extracted with the chloride). This corrected $^{36}\text{Cl}_{n,\gamma}/\text{Cl}$ ratio is the amount of ^{36}Cl produced by the $^{35}\text{Cl}(n,\gamma)^{36}\text{Cl}$ reaction per ppm Cl in that sample. Because the low-energy neutron diffusion lengths are large (~4-10 cm depending on composition) compared to the grain size of the sample (typically <1cm), the low-energy neutron flux, and therefore the $^{36}\text{Cl}_{n,\gamma}/\text{Cl}$ ratio, is homogenous over the rock sample. Consequently, the $^{36}\text{Cl}_{n,\gamma}/\text{Cl}$ ratio is the same for a whole rock sample or a mineral separate of that sample.

The $^{36}\text{Cl}_{n,\gamma}/\text{Cl}$ ratio results from capture of thermal and epithermal neutrons from all sources (including radiogenic neutrons), integrated over the sample's complete exposure history. Thus it includes effects such as changes in water content, snow cover and outcrop geometry, that may have affected neutron capture but are not included when n-produced ^{36}Cl is calculated. Subtracting a measured $^{36}\text{Cl}_{n,\gamma}/\text{Cl}$ value from the total $^{36}\text{Cl}/\text{Cl}$ ratio in K-feldspar is therefore preferable to subtracting a calculated correction for n-produced ^{36}Cl in the K calibration. The approach taken in this study was to compare measured and calculated $^{36}\text{Cl}_{n,\gamma}/\text{Cl}$ ratios, using the data both to calibrate $\mathcal{P}_i(0)$ and to investigate possible causes of variability in neutron fluxes at the sample sites.

Similar techniques to those used by Bierman *et al.* [Bie94] and Dep [Dep95] were investigated as methods for isolating the ^{36}Cl produced by low-energy neutron capture on ^{35}Cl . In the end, ^{36}Cl measurements on pure quartz samples were used to produce the final results discussed in this chapter. However, a description of the early attempts and a discussion of possible future improvements are given in Appendix A.

5.2 The Scottish Quartz Samples

Quartz mineral separates were prepared for eight Scottish samples. These eight were chosen because the corresponding K-feldspar mineral separate contained high chloride concentrations, ranging from 207-275 ppm (discussed in Chapter 6).

The results of the AMS measurements are given in Table 5.1.

Table 5.1 Measurements on Scottish Quartz Samples

Sample Name	Chloride ^a (ppm)	Potassium (%wt)	$[\text{}^{36}\text{Cl}_{n,\gamma}/\text{Cl}]_{\text{meas}}^b \times 10^{15}$	$[\text{}^{36}\text{Cl}_{n,\gamma}/\text{Cl}]_{\text{cosmo}}^{b,c} \times 10^{15}$	$[\text{}^{36}\text{Cl}_{n,\gamma}/\text{Cl}]_{\text{scaled}}^{b,c,d} \times 10^{15}$
At-12 Qtz	63	0.025 (0.008) ^e	50.8 (4.7)	43.2 (5.1)	25.7 (3.4)
At-13 Qtz	25	0.002 (0.006)	55.4 (5.8)	50.1 (6.2)	29.0 (3.9)
95Scot004 Qtz	58	0.025 (0.008) ^e	45.3 (4.7)	28.9 (6.0)	18.9 (5.5)
95Scot018 Qtz	55	0.118 (0.035)	43.6 (2.1)	30.2 (2.9)	23.8 (4.2)
95Scot020 Qtz	38	0.003 (0.001)	47.4 (4.1)	40.7 (4.5)	30.2 (4.0)
95Scot021 Qtz	54	0.004 (0.001)	37.4 (2.7)	28.7 (3.0)	24.0 (4.0)
95Scot041 Qtz	56	0.010 (0.003)	44.8 (3.2)	36.4 (3.6)	26.1 (3.6)
95Scot042 Qtz	59	0.014 (0.004)	38.1 (2.8)	25.5 (3.4)	17.4 (4.2)

^a Estimated from the final AgCl weight and approximating the yield based on previous experience.

^b Including a measured ^{36}Cl and Cl blank correction of 0.9 – 1.3% (§ 4.2.2).

^c Chlorine-36 produced by cosmogenic low-energy neutron, i.e. corrected for potassium produced ^{36}Cl and radiogenic ^{36}Cl .

^d Scaled for a 2π horizon at sea level and high latitude (scaling factors in Appendix B).

^e Average of the K measurements for the other samples. No measurement made.

The chloride concentrations were calculated from the final AgCl weight and an approximate yield, based on previous experience. However, since carrier wasn't added to these samples the uncertainty in the chloride concentrations has negligible impact on the values or uncertainty of the $^{36}\text{Cl}_{n,\gamma}/\text{Cl}$ ratios. (The non-zero potassium concentrations do introduce a very weak dependence on the chloride concentration).

The potassium concentration in the quartz mineral separates was measured by flame photometry (see § 4.2.3). All the samples contained only minor concentrations (see Table 5.1), except for 95SCOT018-Qtz, which contained 0.118%K. Consequently, this sample required a 6% correction to the AMS measurement (see Table 5.2). This, however, is trivial compared to the radiogenic ^{36}Cl in the quartz samples, which accounts for between 17 - 33% of the measured $^{36}\text{Cl}_{n,\gamma}/\text{Cl}$ ratio.

Calcium measurements were not made on quartz mineral separates as the whole rock samples contained very low calcium concentrations (all but one was $\leq 0.11\%$ Ca). Therefore, it was assumed that the calcium concentrations in the quartz samples would be negligible.

The original idea for utilising the quartz sample was to multiply the measured $^{36}\text{Cl}_{n,\gamma}/\text{Cl}$ ratio by the chloride concentration of the K-feldspar mineral separate, to obtain a correction for all the ^{36}Cl concentration due to low-energy neutron capture on ^{35}Cl in the K-feldspar, including radiogenic. Subtracting this

from the total ^{36}Cl concentration measured in the K-feldspar sample would give the ^{36}Cl concentration due solely to one of the potassium (or calcium if its concentration was not assumed to be negligible) production channels. However, it proved practicable to extract quartz separates from only eight of the eighteen samples. The possibility of using the weighted average value of cosmogenic $^{36}\text{Cl}_{n,\gamma}/\text{Cl}$ (corrected for potassium and radiogenic produced ^{36}Cl , and scaled to a 2π horizon at sea level and high latitude) was considered as a compatible correction for the remaining ten K-feldspar samples. This would be justifiable as all the high chloride K-feldspar samples were Torridon Sandstone, for which the composition variation would be fairly small. However the sample to sample variation of the scaled, potassium- and radiogenic-corrected $^{36}\text{Cl}_{n,\gamma}/\text{Cl}$ was significant, as seen in the last column of Table 5.1. Nevertheless, in the final analysis, this was not chosen as the optimal method. However, this method is used in Section 6.3 to show that the results obtained by this method are consistent with the final results.

It was decided that instead of using the $^{36}\text{Cl}_{n,\gamma}/\text{Cl}$ ratio to make a measured correction for the ^{36}Cl produced by low-energy neutrons, a more consistent approach to the analysis would be to use the $^{36}\text{Cl}_{n,\gamma}/\text{Cl}$ ratios to determine the value of $\mathcal{P}_f(0)$. The deduced value of $\mathcal{P}_f(0)$ could then be used to correct for the ^{36}Cl produced by low-energy neutrons in all the K-feldspar samples. To determine the value of $\mathcal{P}_f(0)$ the equations for the spallogenic thermal and epithermal neutrons (equations 2.10 and 2.14) and neutrons produced by negative muon capture and photonuclear reactions (equations 2.18 and 2.20) were used to calculate the $^{36}\text{Cl}/\text{Cl}$ ratio in the quartz samples as a function of $\mathcal{P}_f(0)$. This was compared to the measured $^{36}\text{Cl}/\text{Cl}$ ratio in the form of a χ^2 . By minimising the χ^2 over all the quartz samples the best fit value of $\mathcal{P}_f(0)$ was determined, as described in § 3.3.3.

* All the whole rock values and quantities derived from them that are required in these equations are given in Appendix B.

5.2.1 Evaluation of $\mathcal{P}_f(0)$

The value of $\mathcal{P}_f(0)$ was determined from the eight Scottish quartz mineral separates to be 740 ± 54 fast n (g air) $^{-1}$ yr $^{-1}$, with a reduced χ^2 of 1.13. Figure 5.1 plots the χ^2 surface for $\mathcal{P}_f(0)$.

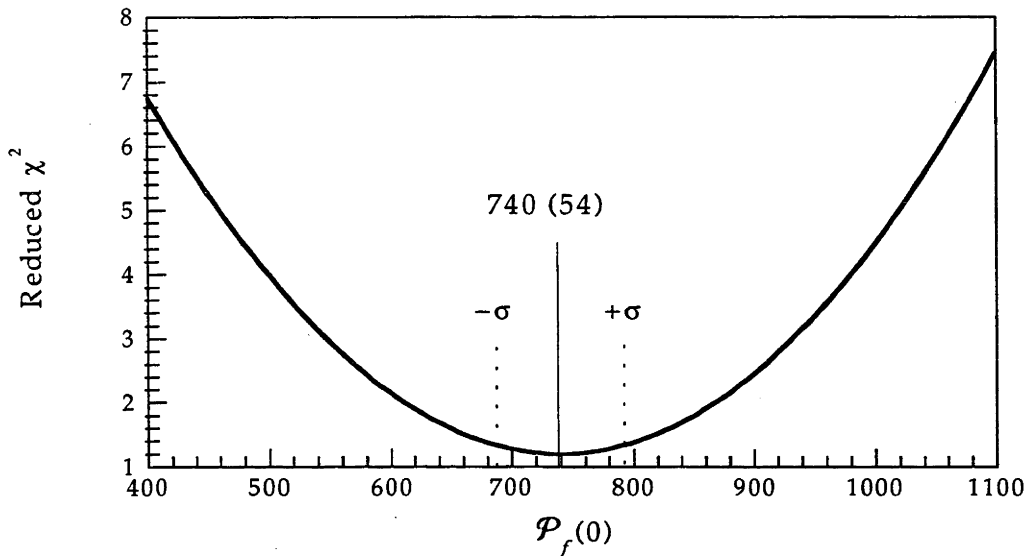


Figure 5.1 $\mathcal{P}_f(0)$ versus χ^2 for the eight Scottish quartz mineral separates.

Table 5.2 shows a breakdown of the calculated ^{36}Cl components in the quartz samples. The spallogenic thermal and epithermal neutrons make up ~70% of the total ^{36}Cl produced in the quartz, with radiogenic ^{36}Cl responsible for a significant proportion of the remaining ^{36}Cl . The amount of ^{36}Cl from low-energy neutrons produced by fast and slow muons, which are not a function of $\mathcal{P}_f(0)$, are an order of magnitude less than spallogenic low-energy neutrons.

Table 5.2 Breakdown of the components making up the measured $^{36}\text{Cl}/\text{Cl}$ ratio.

Sample Name	$[^{36}\text{Cl}_{n,\gamma}/\text{Cl}]_{\text{meas}}$ $\times 10^{15}$	K Spallation	μ^- Capture	Radiogenic Fraction	Cosmogenic Low-energy Neutrons			
					Thermal	Epi-thermal	μ^- capture	Fast muons
At-12Qtz	50.8 (4.7)	1.58%	0.08%	18.04%	62.81%	12.09%	4.81%	0.59%
At-13Qtz	55.4 (5.8)	0.31%	0.02%	17.03%	65.34%	11.97%	4.75%	0.58%
95Scot004Qtz	45.3 (4.7)	1.29%	0.06%	32.70%	52.20%	9.20%	4.04%	0.50%
95Scot018Qtz	43.6 (2.1)	5.68%	0.33%	25.89%	54.66%	8.26%	4.61%	0.57%
95Scot020Qtz	47.4 (4.1)	0.23%	0.01%	20.46%	64.52%	9.46%	4.74%	0.58%
95Scot021Qtz	37.4 (2.7)	0.22%	0.01%	24.14%	60.43%	9.29%	5.26%	0.65%
95Scot041Qtz	44.8 (3.2)	0.56%	0.03%	20.48%	63.49%	9.55%	5.24%	0.64%
95Scot042Qtz	38.1 (2.8)	0.66%	0.04%	26.78%	58.62%	8.73%	4.61%	0.57%

The value reported by Phillips *et al.* [Phi96] was $586 \pm 40 \text{ fast n (g air)}^{-1} \text{ yr}^{-1}$. However, as they only considered spallogenic low-energy neutrons, this is reduced to $551 \text{ fast n (g air)}^{-1} \text{ yr}^{-1}$ when the low-energy neutrons produced by negative muon capture reactions and photonuclear reactions (~6%, see Table 5.2) are subtracted.

5.3 The Effect of Erosion and Local Geometry on the ^{36}Cl Produced from Low-energy Neutrons

One of the most striking features of the scaled cosmogenic $^{36}\text{Cl}_{n,\gamma}/\text{Cl}$ ratios from the quartz samples (Table 5.1) is the large sample-to-sample variation, 70% between the highest and the lowest samples. The uncertainty in the AMS measurements was only of the order of 10%, which cannot account for all of the variation. It is possible that the extra variation is due to a combination of three factors:

1. Some of the variation in the scaled cosmogenic $^{36}\text{Cl}_{n,\gamma}/\text{Cl}$ ratios may be due to undetected erosion at the sample surface. As discussed in Section 2.3.3A and 3.1.2, the production rate of ^{36}Cl by spallogenic low-energy neutron capture initially increases with depth just below the surface because of neutrons lost into the atmosphere during the thermalisation process[†].

Figures 2.3 and 3.1 shows the low-energy neutron flux peaks at $\sim 50 \text{ g cm}^{-2}$, at which point it is $\sim 50\%$ higher than surface neutron flux. In other words if $\sim 50 \text{ g cm}^{-2}$ had been removed from the surface in the last 10,000 years, giving an erosion rate of $\sim 0.002 \text{ cm yr}^{-1}$ (which is the highest reasonable erosion rate), then the scaled cosmogenic $^{36}\text{Cl}_{n,\gamma}/\text{Cl}$ ratios would be $\sim 50\%$ too high. As mentioned previously, the samples were chosen with minimal erosion in mind, however, a zero erosion rate cannot be guaranteed. Therefore it is likely that some of the scaled

[†] While this effect has only been studied for spallogenic secondaries, there is no reason to believe a similar effect would not occur for secondary neutrons produced by stopped negative muon capture or photonuclear reactions, although the magnitude may be different as the energy of the original secondary neutrons varies depending on the reaction channel. For example, spallogenic secondaries are produced with an average energy of 1 MeV while neutrons produced by negative muon capture have an average energy of 5 MeV [Fab88]. On the other hand, this effect would not be expected to be seen in the radiogenic ^{36}Cl contribution as the concentration is assumed to be at steady state, and therefore only a minor portion of the ^{36}Cl was produced in the last 11,600 years.

cosmogenic $^{36}\text{Cl}_{n,\gamma}/\text{Cl}$ ratios are high because a small amount of erosion has gone undetected. However, the effect is unlikely to be as high as, and can't be more than, 50%.

2. Production of ^{36}Cl by low-energy neutrons is sensitive to the local geometry, ≤ 1 m radius, where the thermalisation process occurs (§ 3.2). To demonstrate this point, consider the samples 95SCOT041 and 95SCOT042. These samples were collected from the same large boulder (~3 m high, and ~2.5 m long and wide). Therefore, they have the same exposure history, the only difference being that 95SCOT041 was collected in the middle of the top surface (all edges > 1 m away) and 95SCOT042 was collected about 30 cm from the corner. The scaled cosmogenic $^{36}\text{Cl}_{n,\gamma}/\text{Cl}$ ratio for 95SCOT042 is 35% lower than 95SCOT041, which can be attributed to the loss of low-energy neutrons from the sides (if there was pre-exposure from one of the sides, the edge sample would have a higher $^{36}\text{Cl}_{n,\gamma}/\text{Cl}$ ratio). This is analogous to the low-energy neutron loss from the surface described in Section 3.2 and in Liu *et al.* [Liu94].

This conclusion is supported by measurements made by Dep [Dep95], in which the $^{36}\text{Cl}/\text{Cl}$ ratio was measured in four whole rock samples collected from a single granodiorite boulder on a glacial moraine at Bishop Creek, USA. Two of the samples were from the top of the boulder and two of the samples were taken from the side of the boulder. The samples had high chloride concentrations (137-197 ppm) and low calcium and potassium concentrations (3.31-3.89 %wt and 1.60-2.41 %wt respectively). The weighted average exposure age (calculated directly from the measured $^{36}\text{Cl}/\text{Cl}$ ratio) of the two samples taken from the top of the boulder was 15% lower than expected. Dep attributed this to the reduction in the ^{36}Cl production rate from low-energy neutron capture because of the proximity of the sample to the boulder edge.

3. In addition to the effect of erosion discussed above, high $^{36}\text{Cl}_{n,\gamma}/\text{Cl}$ ratios in several of the quartz samples such as AT-13 and 95Scot020 could be explained by a neutron capture enhancement due to outcrop geometry. These samples were collected on the lower portion of glacially-plucked steps in bedrock - a precaution intended to minimize the possibility of pre-exposure (see § 3.2.3). For these samples, high $^{36}\text{Cl}_{n,\gamma}/\text{Cl}$ ratios may be attributable to an increase in the low energy neutron flux at the sample site due to low energy neutrons being lost from the wall overlooking the sampling point and captured in the surface below.

Although some of the scatter in the $^{36}\text{Cl}_{n,\gamma}/\text{Cl}$ values may be due to the effects discussed above, the mean value of $\mathcal{P}_f(0)$ derived here is unlikely to be systematically offset. The samples were collected with care to avoid eroded surfaces and obtain 2π exposure geometry where possible. Nevertheless, the possibility of measurable local geometry effects warrants further investigation.

Chapter Six

³⁶Cl PRODUCTION BY SPALLATION: SCOTTISH K-FELDSPAR MINERAL SEPARATES

The spallation production rate is constrained by 18 surface samples exposed by the end of the Loch Lomond Readvance glaciation in Scotland. Chlorine-36 measurements were made on pure K-feldspar mineral separates, which virtually removed the ³⁶Cl contribution due to calcium production channels. Fifteen of the samples are Torridon Sandstone and had fairly high chloride concentrations (141 – 275 ppm), so that low-energy neutron capture on ³⁵Cl accounted for 24% - 37% of the total cosmogenic ³⁶Cl in the sample. Consequently, the treatment of low-energy neutrons described in Chapter 5 is very important for these samples. The remaining three samples are granites, with low chloride concentrations (20.5 – 27.6 ppm), and therefore more than 89% of the cosmogenic ³⁶Cl was produced via one of the potassium production channels. As a result, these samples played a dominant role in constraining the potassium production rate.

The production rate of ³⁶Cl from potassium spallation is deduced in Section 6.1. Section 6.2 compares the value derived in this work with those previously published. Section 6.3 then demonstrates that the value determined for the potassium spallation production rate is independent of the method of analysis chosen for the quartz samples in Chapter 5.

6.1 Chlorine-36 Production from Spallation on Potassium

A map of the locations from which the samples were collected is given in Figure 6.1, and the details of the sample locations and scaling parameters can be found in Table B1 in Appendix B. The assumed exposure age of all the samples is 11,600 years (a description of the relevant glacial history, justifying this choice of deglaciation age, is given in § 3.3.1). All the samples are Torridon Sandstone, except 95SCOT047, 95SCOT063 and 95SCOT068 which are granites.

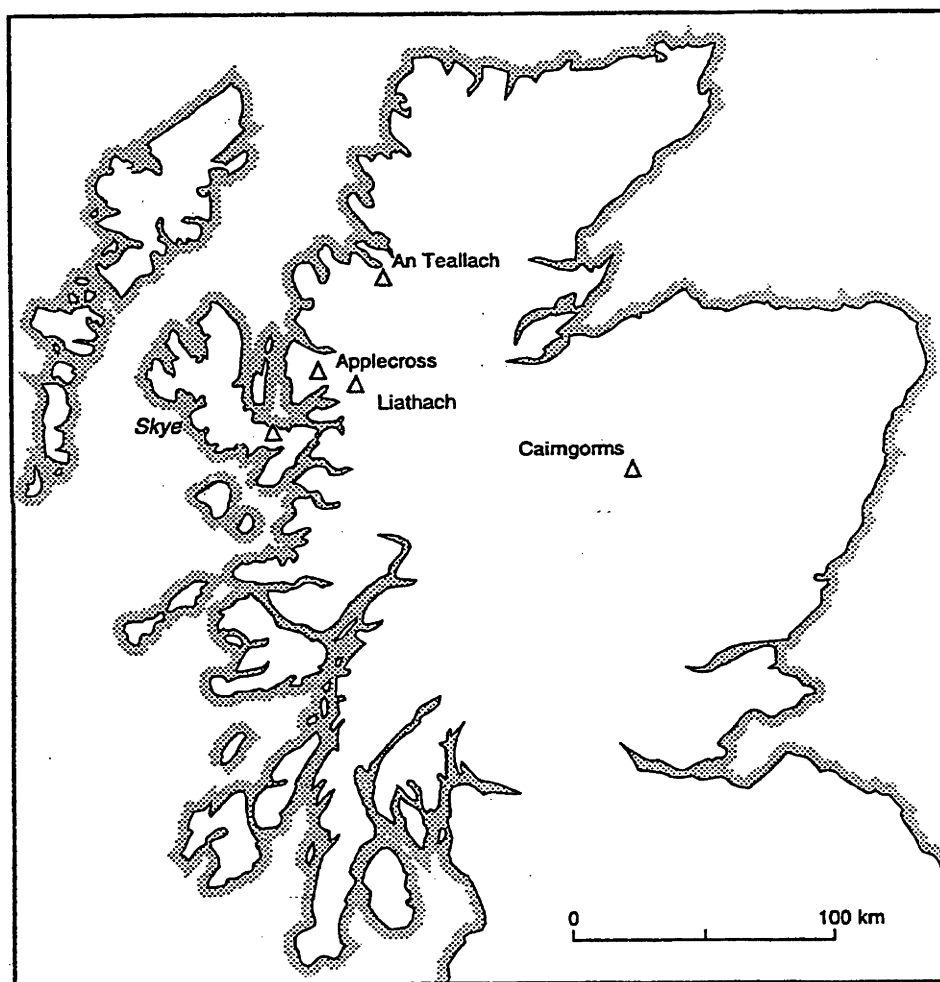


Figure 6.1 Map of Western Scotland indicating the locations from which the samples were collected. Samples AT-10, AT-11, AT-12 and AT-13 were collected at An Teallach. Samples 95SCOT004, 95SCOT018, 95SCOT020, 95SCOT021, 95SCOT032, 95SCOT041 and 95SCOT042 were collected near Liathach. Samples 95SCOT006, 95SCOT007, 95SCOT008 and 95SCOT015 were collected at Applecross. Sample 95SCOT047 was collected from Skye, and samples 95SCOT063 and 95SCOT068 were collected in the Cairngorms.

Table 6.1 presents the measurements made on the K-feldspar mineral separates. The potassium concentration measurements were made by flame photometry, the calcium concentration by X-ray fluorescence, and the chloride concentration by isotope dilution. The $^{36}\text{Cl}/\text{Cl}$ ratios were measured by AMS, and the ^{36}Cl concentrations of the K-feldspar mineral separates were calculated from the $^{36}\text{Cl}/\text{Cl}$ ratio and the chloride concentration. As a result of the samples' low altitudes and relatively short exposure, the ^{36}Cl concentrations in these samples were low and high sensitivity was required in the AMS measurements. The high $^{36}\text{Cl}/\text{Cl}$ ratios for 95SCOT063 and 95SCOT068 reflect the low chloride concentration of the K-feldspar mineral separates and the high altitude from which the samples were collected (~930 m, compared to $\leq 570\text{m}$).

Table 6.1 Composition of K-feldspar mineral separates

Sample Name	Potassium (K % wt)	Calcium (Ca % wt)	Chloride (ppm)	Measured $^{36}\text{Cl}/\text{Cl}$ ($\times 10^{-15}$)	$[^{36}\text{Cl}]$ (atom g^{-1}) ^a ($\times 10^5$)
AT-10	11.48 (0.02)	0.02 (0.02)	169.3 (1.6)	118.0 (5.6)	5.37 (0.26)
AT-11	12.15 (0.01)	0.04 (0.04)	181.9 (1.6)	110.0 (6.8)	5.30 (0.33)
AT-12	11.95 (0.02)	0.04 (0.04)	226.3 (2.2)	103.3 (5.9)	5.57 (0.32)
AT-13	11.86 (0.03)	0.04 (0.04)	237.8 (3.8)	108.0 (6.2)	6.01 (0.36)
95Scot004	10.42 (0.02)	0.11 (0.11)	207.1 (2.5)	70.6 (4.6)	4.53 (0.30)
95Scot006	7.20 (0.10)	0.20 (0.20)	141.2 (1.7)	74.2 (5.1)	2.81 (0.20)
95Scot007	10.70 (0.06)	0.05 (0.05)	213.2 (2.6)	72.4 (4.6)	3.60 (0.23)
95Scot008	10.38 (0.03)	0.46 (0.46)	174.2 (2.0)	71.5 (4.8)	3.10 (0.21)
95Scot015	10.56 (0.06)	0.09 (0.09)	208.3 (2.5)	75.5 (4.7)	3.66 (0.23)
95Scot018	11.44 (0.04)	1.43 (1.43)	232.9 (2.9)	62.2 (4.1)	3.57 (0.24)
95Scot020	10.92 (0.17)	0.04 (0.04)	231.6 (2.2)	68.8 (4.6)	3.93 (0.27)
95Scot021	10.18 (0.02)	0.06 (0.06)	246.9 (3.1)	61.7 (3.8)	3.64 (0.23)
95Scot032	10.14 (0.03)	0.04 (0.04)	173.3 (2.2)	91.3 (6.2)	4.14 (0.29)
95Scot041	10.63 (0.03)	0.04 (0.04)	267.6 (2.4)	70.6 (4.3)	4.27 (0.26)
95Scot042	11.19 (0.05)	0.04 (0.04)	275.4 (3.4)	78.0 (5.2)	4.91 (0.33)
95Scot047	5.97 (0.02)	0.93 (0.93)	22.5 (0.3)	81.5 (6.7)	1.51 (0.13)
95Scot063	11.46 (0.01)	0.34 (0.34)	27.6 (0.3)	301.4 (14.4)	6.59 (0.32)
95Scot068	10.91 (0.08)	0.34 (0.34)	20.5 (0.3)	405.2 (19.9)	6.54 (0.32)

^a Including a measured ^{36}Cl and Cl blank correction of 0.2-1.2%.

The whole rock major element and trace element measurements are given in Table B2 and B3 respectively. These concentrations are important as they are used to calculate terms such as the macroscopic cross section for thermal neutron capture, which define the amount of ^{36}Cl produced by low-energy neutron capture on ^{39}K and ^{35}Cl . All the derived terms (calculated from values in Table B.2, B.3 and 6.1) are given in Table B.4.

It is interesting to note that for the samples with high chloride concentrations, the percentage of low-energy neutrons captured by a ^{35}Cl nucleus is an order of magnitude higher than the percentage of low-energy neutrons

captured by a ³⁹K nucleus. However, for the samples with low chloride (~20 ppm) and high potassium concentrations (~10%), the percentage of low-energy neutrons captured by a ³⁵Cl nucleus is of the same order of magnitude as the percentage of low-energy neutrons captured by a ³⁹K nucleus.

Table 6.2 gives a breakdown of the calculated ³⁶Cl concentration by production channel, as well as the total measured ³⁶Cl concentration for comparative purposes. Spallation on potassium is the largest contributor to ³⁶Cl concentration, although the contribution of ³⁶Cl from low-energy neutron capture on ³⁵Cl is significant in all but the three low chloride samples.

The negative muon capture on ³⁹K accounts for between 3.9% and 5.7% of the total cosmogenic ³⁶Cl production due to potassium in each of the samples, with the variation arising from the different altitudes of the samples. The low-energy neutron capture on ³⁹K accounts for between 2.1% and 3.3% of the total cosmogenic ³⁶Cl produced from potassium in each of the samples, with the range predominantly due to the varying chemical compositions of the samples. The combined ³⁶Cl contribution from these minor production channels is 6.5% to 8.8% of the total cosmogenic ³⁶Cl, with an average of 7.7%. Therefore, values of P_K from earlier work must be adjusted downwards by this fraction in order to compare them with the potassium spallation rate derived in this study.

Table 6.2 Breakdown of ³⁶Cl concentration by production channel in the Scottish K-feldspar samples

Sample Name	Total measured ³⁶ Cl 10 ² atom g ⁻¹	Reactions on Potassium			Reactions on ³⁵ Cl		Reactions on Ca ¹ 10 ² atom g ⁻¹
		Spallation 10 ² atom g ⁻¹	μ capture 10 ² atom g ⁻¹	Neutron capture ² 10 ² atom g ⁻¹	Cosmogenic n capture 10 ² atom g ⁻¹	Radiogenic n capture 10 ² atom g ⁻¹	
AT-10	5370 (263)	3242	158	116	1323	209	2
AT-11	5296 (332)	3531	177	116	1251	304	4
AT-12	5569 (324)	3350	166	94	1289	289	4
AT-13	6007 (356)	3253	162	95	1404	289	4
95Scot004	4532 (302)	2633	136	98	1162	576	9
95Scot006	2811 (196)	1459	88	58	821	192	14
95Scot007	3604 (234)	2129	131	89	1231	357	3
95Scot008	3096 (211)	2041	125	83	905	346	30
95Scot015	3656 (230)	2046	128	92	1229	401	6
95Scot018	3565 (242)	2234	134	89	1180	449	94
95Scot020	3928 (266)	2025	122	78	1182	305	2
95Scot021	3636 (228)	1963	118	73	1204	384	4
95Scot032	4142 (286)	2665	142	110	1406	277	3
95Scot041	4269 (261)	2409	137	87	1546	401	3
95Scot042	4905 (329)	2516	144	101	1623	599	3
95Scot047	1514 (126)	1213	74	42	100	42	63
95Scot063	6589 (316)	4858	205	348	301	451	47
95Scot068	6535 (322)	4625	195	404	217	466	47

¹ spallation + negative muon capture

² cosmogenic + radiogenic

From the ^{36}Cl concentrations and the assumed exposure age of the samples, the ^{36}Cl production rate due to spallation on potassium can be calculated. This was deduced using the values of $\mathcal{P}_f(0)$ constrained by the Scottish quartz samples (see Chapter 5), and the ^{36}Cl yield per stopped negative muon constrained by the Wyangala depth profile (see Chapter 7) to determine the ^{36}Cl concentration as a function of the potassium production rate for each sample. The best value of the potassium spallation production rate was then determined by χ^2 minimisation (see § 3.3.3) over the 18 Scottish K-feldspar mineral separates.

The value of $P_{\text{K,sp}}(0)$ was determined to be 161 ± 9 atom $(\text{gK})^{-1} \text{yr}^{-1}$ with a reduced χ^2 of 1.91. Figure 6.2 shows the χ^2 surface for $P_{\text{K,sp}}(0)$.

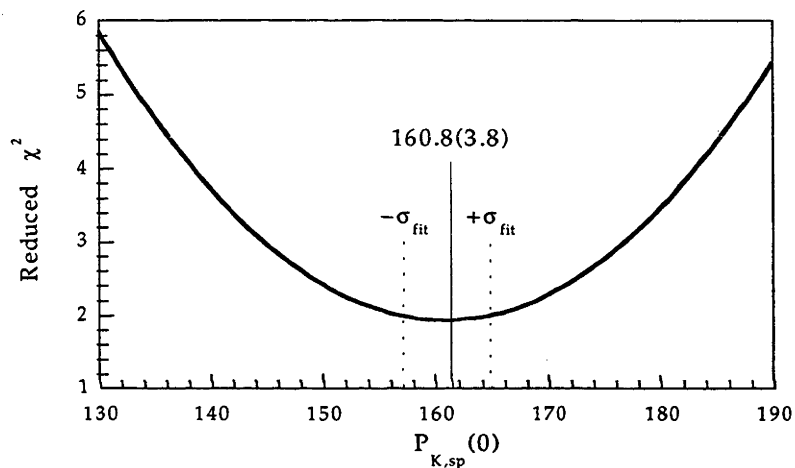


Figure 6.2 The χ^2 surface for $P_{\text{K,sp}}(0)$ determined from 18 Scottish K-feldspar mineral separates.

The uncertainty in the value of $P_{\text{K,sp}}(0)$ above incorporates three components added in quadrature. The first component is the statistical uncertainty from the fit which was determined by increasing the χ^2 by 1 [Bev92, Lyo86, Pre87]. The second component of the uncertainty comes from the assumed exposure age (see §3.3.1). The final component comes from the uncertainty in ^{36}Cl contribution from low-energy neutron capture in the K-feldspar mineral separate. To determine this uncertainty, the fit to $P_{\text{K,sp}}(0)$ was repeated using values of $\mathcal{P}_f(0) \pm 1\sigma$. The change in the value of $P_{\text{K,sp}}(0)$ was taken as the third component of the uncertainty. The major contributor (~60%) to the final value of the uncertainty was from the assumed exposure age.

As a simple exposure history has been assumed for the Scottish samples, the possibility exists that pre-exposure or erosion on the samples has been erroneously

neglected. Both these possibilities are discussed in detail in Appendix C where it is shown that neither pre-exposure nor erosion is likely to be a major source of systematic uncertainty in this study.

6.2 The Potassium Spallation Production Rate and Comparison with Previous Work

The value of $P_{k,sp}(0)$ derived in this study is $161 \pm 9 \text{ atom}^{-1} (\text{gK})^{-1} \text{ yr}^{-1}$ at sea level and high latitude. To compare this with the production rates determined in previous calibrations [Zre91, Swa94, Phi96] the values of P_k from those calibrations must be adjusted by 7.7% (see page 86) to obtain potassium spallation rate values from their results (as opposed to total ³⁶Cl production from potassium).

Table 6.3 Comparison of the values determined for the ³⁶Cl production by spallation on potassium.

This Study	161 (9) atom (gK) ⁻¹ yr ⁻¹
Phillips <i>et al.</i> , (1996)	142 (9) atom ⁻¹ (gK) ⁻¹ yr ⁻¹ (adjusted) ^a
Swanson <i>et al.</i> , (1994)	208 (26) atom ⁻¹ (gK) ⁻¹ yr ⁻¹ (adjusted) ^a
Zreda <i>et al.</i> , (1991)	99 (7) atom ⁻¹ (gK) ⁻¹ yr ⁻¹ (adjusted) ^a

^a 7.7% correction has been made for ³⁶Cl production by negative muon capture and low-energy neutron capture on potassium.

The potassium spallation production rate determined in this study is 29% less than the adjusted production rate determined by Swanson *et al.* [Swa94], which is almost within error, and 13% more than the adjusted production rate determined by Phillips *et al.* [Phi96], which is within error. The adjusted value obtained by Zreda *et al.* [Zre91] is 63% lower than the value determined in this study, but this value has already been superseded [Phi96] because the assumed exposure history of the samples was incorrect (see §3.3.1).

Aside from possible errors in the assumed exposure history in the calibration sites, there are several factors that contribute to the variation in the values in Table 6.3. The first is that the previous calibrations were attempting to determine the ³⁶Cl production rates from calcium, ³⁵Cl and potassium. In almost all the samples, however, the ³⁶Cl production was dominated by calcium and/or ³⁵Cl production channels. Consequently, the production rate due to potassium was extremely vulnerable to systematic errors in these production rates.

Secondly, the previous calibrations only considered the spallation production channel for ^{36}Cl production from potassium (and calcium). Consequently, when the derived production rates were scaled to sea level from the various altitudes of the sample sites, only the spallation correction factors were used. As a portion of the production rate was actually due to muon reactions, which vary less steeply with altitude than spallation reactions, this will underestimate the production rate at sea level. This error was not corrected when the adjustment of 7.7% was made above to account for the production by negative muon capture and low-energy neutron capture. This effect is $\approx 4\%$ (depending on altitude).

Thirdly, the previous calibrations were based on whole rock measurements. Consequently, additional ^{36}Cl would have been produced by minor reaction channels such as spallation of titanium and iron. Iron and titanium tend to concentrate in Ca-rich, basaltic rocks, so contributions from these elements are likely to be a more serious source of error in previous estimates of the Ca spallation rate. Nonetheless, previous whole-rock calibrations of ^{36}Cl from K have used samples requiring significant Ca corrections. If the (granite) samples used for K calibration have lower Fe/Ca and Ti/Ca ratios to those (basaltic samples) used for Ca calibration, the adjustments for Ca-derived ^{36}Cl will be too high - and the resulting estimates of P_K will likely be too low. The magnitude of this effect is likely to be small, based on the Ti and Fe spallation rates estimated by Masarik and Reedy [Mas96] (but these remain to be calibrated). This particular source of uncertainty does not affect the values determined in this calibration because K-feldspar contains only a small amount of iron and negligible titanium.

Finally, the largest uncertainty in this calibration, as with the previous calibrations, is the correction for the ^{36}Cl production by low-energy neutron capture on ^{35}Cl . This is also where the greatest potential for improvement in the near future lies, as discussed in the next section.

6.3 Measured Vs Model-Dependent Correction of Low-energy Neutron Capture on ^{35}Cl

As discussed in Chapter 5, the original intention in this study was to measure $^{36}\text{Cl}_{n,\gamma}/\text{Cl}$ ratios in potassium-free quartz from the Scottish samples, and

use the values as a basis for subtracting the low-energy neutron-produced ^{36}Cl in the K-feldspar. In the end, however, these data were used as input to a model of the neutron capture process to derive a value of $\mathcal{P}_f(0)$. This value was then used to determine the contribution of neutron capture for all 18 samples, not just the 8 for which measurements on quartz were made. It is interesting, however, to compare the model-based approach with the more direct experimental approach. The following will demonstrate that the potassium spallation production rate obtained is independent of the method of the way the quartz data are used in the calculation.

Table 6.4 shows the total ^{36}Cl concentration (cosmogenic and radiogenic) due to low-energy neutron capture on ^{35}Cl determined from i) the model dependent approach (see Chapter 5) and ii) directly from the measurements on the quartz samples.

Table 6.4 The total ^{36}Cl production from neutron capture on potassium calculated using two different methods.

Sample Name	Total ^{36}Cl concentration due to low-energy neutron capture on ^{35}Cl in the K-feldspar mineral separates		P_K^a atom (gK) $^{-1}$ yr $^{-1}$
	model-dependent	measured	
AT-12	$1.58 (0.12) \times 10^5$	$1.98 (0.18) \times 10^5$	176 (16)
AT-13	$1.69 (0.12) \times 10^5$	$2.32 (0.24) \times 10^5$	187 (20)
95Scot004	$1.74 (0.13) \times 10^5$	$1.61 (0.17) \times 10^5$	182 (20)
95Scot018	$1.63 (0.12) \times 10^5$	$1.73 (0.08) \times 10^5$	133 (17)
95Scot020	$1.49 (0.11) \times 10^5$	$1.91 (0.17) \times 10^5$	162 (23)
95Scot021	$1.59 (0.12) \times 10^5$	$1.59 (0.11) \times 10^5$	168 (19)
95Scot041	$1.95 (0.14) \times 10^5$	$2.07 (0.15) \times 10^5$	149 (18)
95Scot042	$2.22 (0.16) \times 10^5$	$1.81 (0.13) \times 10^5$	200 (21)

^a The total ^{36}Cl production from potassium deduced using the measured $^{36}\text{Cl}_{n,\gamma}/\text{Cl}$.

The uncertainty in the measured ^{36}Cl concentration is due to the AMS experimental uncertainty. The calculated and measured ^{36}Cl concentrations due to low-energy neutron capture on ^{35}Cl agree within their relative uncertainties in almost all the samples.

The measured $^{36}\text{Cl}_{n,\gamma}/\text{Cl}$ ratio can now be used to deduce the total ^{36}Cl production from potassium (see Table 6.4). The weighted average of these values is 168 (7) atom (gK) $^{-1}$ yr $^{-1}$. Adjusting this value by 7.7% (see page 86) to subtract the contributions due to negative muon capture and neutron capture by potassium leads to a production rate due to spallation alone of 157 (19) atom (gK) $^{-1}$ yr $^{-1}$. This is in very good agreement with the value of 161 (9) atom (gK) $^{-1}$ yr $^{-1}$ obtained using the

derived value of $\mathcal{P}_A(0)$ and minimising the χ^2 for the entire set of Scottish K-feldspar samples. This indicates that from the eight quartz samples the derived value of $\mathcal{P}_A(0)$ is representative of the 18 K-feldspar samples, and that the Liu *et al.* [Liu94] neutron capture model is adequately treating the low-energy neutrons within the degree of uncertainty of the measurements.

It is important to also note that the $^{36}\text{Cl}_{n,\gamma}/\text{Cl}$ ratio in the quartz samples already incorporates a correction for erosion on that portion of the ^{36}Cl concentration and this makes the value determined for potassium spallation more sensitive to erosion. This point is illustrated in Figures C.1 and C.2, which shows that when ^{36}Cl is produced by both low-energy neutron capture and potassium spallation (as in the K-feldspar samples) the increase in the n-capture production rate just below the surface counteracts the exponential decrease with depth of the spallation production rate, making the samples much less sensitive to erosion than samples containing only spallation or n-produced ^{36}Cl .

A final test of the effect that ^{36}Cl produced by low-energy neutron capture has on the calibration of $P_{K,sp}(0)$ is to determine the value of $P_{K,sp,granite}(0)$ by minimising the χ^2 only over the three low-chloride granite samples. From this, a value of 174 (9) atom (gK) $^{-1}$ yr $^{-1}$, with a reduced χ^2 of 0.66 is obtained. If the same is done for the 15 sandstone samples, which have an average chloride concentration of 212 ppm, the value for $P_{K,sp,sandstone}(0)$ is determined to be 155 (12) atom (gK) $^{-1}$ yr $^{-1}$, with a reduced χ^2 of 1.65. These values agree within error, which again indicates that the treatment of the low-energy neutrons is not adversely affecting the accuracy of the potassium spallation production rate.

There is considerable scope for improving the experimental correction of low-energy n-produced ^{36}Cl by measuring the $^{36}\text{Cl}_{n,\gamma}/\text{Cl}$ ratio. Particularly, the effect of local geometry on low-energy neutrons needs to be quantified, as discussed in Chapter 5. In addition, an improved method for modeling low-energy neutrons by Phillips *et al.* [Phi01] (see §3.2.2) appears promising. With these future improvements, the uncertainty caused by the ^{36}Cl produced by low-energy neutron capture will be reduced and the value of ^{36}Cl production by potassium spallation can be even more tightly constrained.

Chapter Seven

³⁶Cl PRODUCTION DUE TO NEGATIVE MUON CAPTURE: WYANGALA DEPTH PROFILE

The negative muon capture rate was determined by measuring the ³⁶Cl concentration in K-feldspar rich (~30%) granite samples from a depth profile down to 6 meters. The samples were taken from a granite quarry face in Wyangala, Australia (latitude 34° 02' S, longitude 148° 55' E). The quarry is young enough that the surface can be considered fresh in terms of *in-situ* ³⁶Cl production, however, the area is known to be geologically very old and stable (see §3.3.1) so that the ³⁶Cl concentration can be assumed to be at steady state for the entire profile. As a result, even the deepest samples have high ³⁶Cl concentrations and high precision ³⁶Cl measurements were possible.

In total, 18 samples were analysed, 16 samples in the depth profile and 2 samples collected from pastoral land adjacent to the quarry. As even very low erosion rates will have a large effect on the steady state ³⁶Cl concentration, it was necessary to allow the erosion rate to be a free parameter in the fit to the depth profile, as described in Section 3.3.1. Section 7.1 compares the erosion rates determined for the two samples adjacent to the quarry with the erosion rate determined from the sample at the top of the profile.

Section 7.2 discusses the value deduced for the ³⁶Cl yield per stopped negative muon, Y_{ν} , and the erosion rate of the profile, ϵ , determined using the entire deep profile.

Section 7.3 then discusses two possible sources of uncertainty for the value determined for the negative muon production rate: i) assumptions made about the top of the profile, and ii) uncertainty in the ^{36}Cl contribution from low-energy neutron capture at depth in the profile.

Finally, Section 7.4 discusses the ^{36}Cl production rate due to negative muon capture on potassium, and makes a comparison with the ^{36}Cl production rate due to due negative muon capture on calcium [Sto98].

7.1 Surface Samples

Three surface samples were collected for comparison to the profile samples to ensure that the top of the profile was identified. WYS3 and WYS4 were collected in a pastoral paddock adjoining the quarry, and therefore were unaffected by the quarry. The rock outcrops from which the samples were collected were "tors", which are convex, residual outcrops that stick out of the hillside. Consequently, they would be expected to have a lower erosion rate than at the top of the profile. WYS3 was on the top of the hill and WYS4 was roughly half way between WYS3 and the top of the profile.

The third surface sample was WYBACK which was collected several meters from the quarry edge on a flake lying over the slab that formed the top of the profile (see Figure 7.1). To "reconstruct" the profile, it was believed that the flake and the slab extended over the top of the profile until the time of quarrying. Consequently, WYBACK was taken as the original top of the profile, and WYTOP the next highest sample with a shielding depth of $c.15 \text{ g cm}^{-2}$. This scenario is in agreement with the ^{36}Cl concentrations measured in the sample, as well as the measured ^{10}Be and ^{26}Al concentrations made on the samples [Sto01].

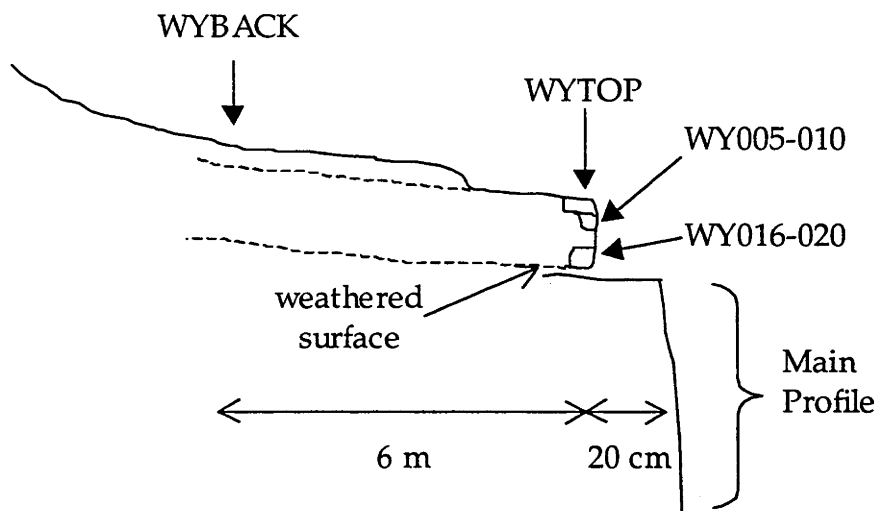


Figure 7.1 Schematic diagram showing the positions of WYBACK and WYTOP relative to the main of the depth profile.

Table 7.1 gives the locations of the surface samples and their correction factors. The thickness corrections shown in the table were calculated assuming there was zero erosion at the surface, and as a consequence of the air/ground boundary effect, the thickness correction for the thermal neutrons is large. However, the air/ground boundary effect occurs only within the top $\sim 50 \text{ g cm}^{-2}$, and at greater depths than this it scales (to first order) with the spallation production rate. Therefore, erosion will reduce this thickness correction.

Table 7.1 Location and Correction factors of the Wyangala surface samples.

Sample Name	Altitude (m)	Alt/Lat Correction		Horizon Correction	Thickness Correction ^a		
		Spallation	Muons		spallation	thermal n	Epithermal n
WYS3	610 ^b	1.45	1.17	1.00	0.96	1.33	1.04
WYS4	570	1.40	1.15	1.00	0.96	1.31	1.05
WYBACK	540	1.37	1.13	0.99	0.94	1.43	1.06

^a Calculated assuming zero erosion.

^b Top of the hill.

To determine the proper low-energy neutron thickness correction for an eroding surface, the ^{36}Cl concentration produced by spallogenic thermal neutron capture on ^{35}Cl was calculated as a function of depth for erosion rates of $0 \text{ }\mu\text{m yr}^{-1}$, $1 \text{ }\mu\text{m yr}^{-1}$, $2 \text{ }\mu\text{m yr}^{-1}$ and $5 \text{ }\mu\text{m yr}^{-1}$, as plotted in Figure 7.2.

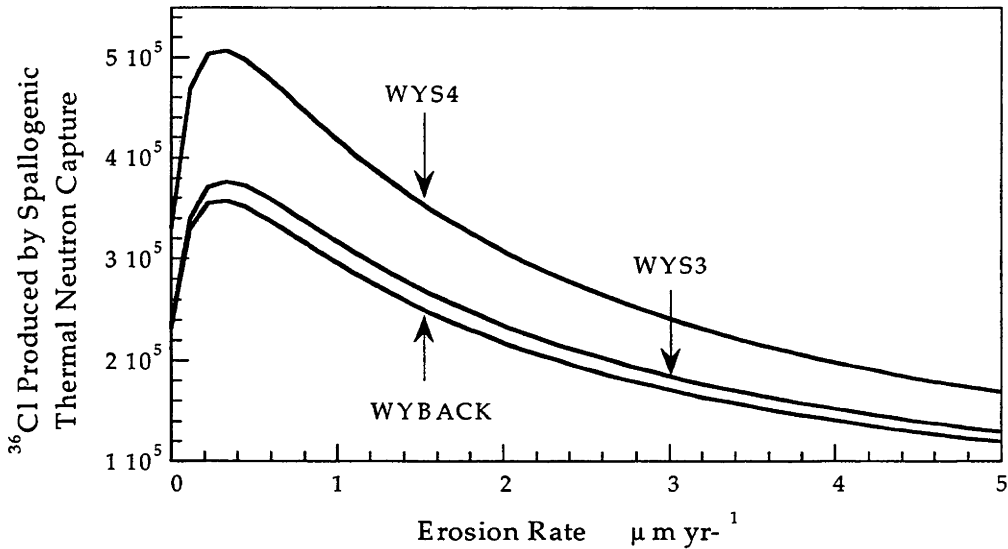


Figure 7.2 The steady state ^{36}Cl concentration produced by spallogenic thermal neutron capture on ^{35}Cl as a function of erosion. The 3 curves are calculated for WYS3, WYS4 and WYBACK. The effect of the air/ground boundary is no longer visible for erosion rates $> 0.5 \mu\text{m yr}^{-1}$, which is lower than the expected erosion rate at Wyangala. Therefore, the spallation depth correction should be used for the low-energy neutron capture production channels for the surface samples.

The effect of the air/ground boundary is removed for erosion rates $> 0.5 \mu\text{m yr}^{-1}$. As the erosion rate at Wyangala is expected to be higher than this, the appropriate thickness scaling parameter for the low-energy neutron capture production rates for the surface samples is the spallation thickness correction.

Figure 7.2 has further implications for the ability of the surface samples to constrain the erosion rate. As discussed in Appendix C, most of the Scottish surface samples were insensitive to erosion because the combined effects of the low-energy neutron capture production rate and the spallation production rate make the ^{36}Cl concentration fairly constant for the first couple of cm, as seen in Figure C.1 and C.2. However, Figure 7.2 shows that because the samples are at steady state, the air/ground boundary effect is only present for erosion rates lower than that expected at Wyangala. Consequently the ^{36}Cl concentration in the surface samples is very sensitive to the erosion rate.

Table 7.2 presents the measurements made on the K-feldspar mineral separate. The $^{36}\text{Cl}/\text{Cl}$ ratios were measured by AMS, the potassium concentration by flame photometry, the calcium concentration by ICP-OES, and the chloride concentration by isotope dilution. The ^{36}Cl concentrations of the K-feldspar

mineral separates were calculated from the $^{36}\text{Cl}/\text{Cl}$ ratio and the chloride concentration. The raw result as well as the value scaled to a 2π surface at the top of the profile are presented below.

The whole rock major element and trace element concentration are given in Table D.1 and D.2 in Appendix D. The results in these Tables, along with the values given in Table 7.2 are used to derive the parameters important to the low-energy neutron capture production rates, and are given in Table D.3.

The ^{36}Cl concentration due to thermal neutron capture in WYS3 is significantly higher than the other samples because its gadolinium and samarium concentrations (Table D.2) are roughly half that of the other surface samples.

Table 7.2 Composition of the Wyangala surface K-feldspar mineral separates.

Sample Name	Potassium (% wt)	Calcium (% wt)	Chloride (ppm)	Measured $^{36}\text{Cl}/\text{Cl}$ ($\times 10^{15}$)	^{36}Cl ^a (atom g^{-1}) ($\times 10^5$)	^{36}Cl ^b (atom g^{-1}) ($\times 10^5$)
WYS3	10.46 (0.01)	0.24 (0.10)	18.1 (0.2)	See Table 7.3	44.03 (1.40) ^c	43.50 (1.38)
WYS4	10.95 (0.12)	0.29 (0.03)	19.0 (0.3)	2328 (78)	25.81 (0.89)	26.38 (0.93)
WYBACK	11.11 (0.07)	0.24 (0.10)	17.5 (0.2)	1883 (65)	19.93 (0.71)	21.66 (0.76)

^a Unscaled ^{36}Cl concentration.

^b Chlorine-36 concentration scaled to the top of the profile and corrected for thickness and shielding.

^c Weighted average of measurements on duplicate AgCl samples from the same K-feldspar.

The reproducibility of the chemical preparation and AMS measurements was demonstrated by four repeat Wyangala samples, shown in Table 7.3. After adjusting the measured $^{36}\text{Cl}/\text{Cl}$ for the different sample weights and the amount of carrier added, the ^{36}Cl concentrations obtained for all four samples are in very good agreement. The weighted average of the two ^{36}Cl concentrations were used in all the calculations and are shown in all subsequent tables and figures.

Table 7.3 The ^{36}Cl concentration measurements made on duplicate AgCl samples prepared from the same K-feldspar mineral separate.

Sample Name	Sample Weight (g)	Chloride Carrier (mg)	Measured $^{36}\text{Cl}/\text{Cl} \times 10^{15}$	^{36}Cl (10^5 atom g^{-1})	^{36}Cl ^a (10^5 atom g^{-1})
WYS3	13.060	1.164	2412 (81)	44.21 (1.50)	
WYS3R	24.209	1.179	3828 (123)	43.91 (1.44)	44.03 (1.40)
WYTOP	13.672	1.166	1006 (38)	18.74 (0.71)	
WYTOPR	17.593	1.185	1192 (50)	18.63 (0.79)	18.70 (0.66)
WY016-020	14.099	1.163	923 (37)	16.39 (0.82)	
WY016-020R	26.639	1.181	1368 (49)	15.44 (0.56)	15.61 (0.55)
WY038-045	14.007	1.160	550 (24)	9.52 (0.42)	
WY039-045R	10.413	1.181	472 (19)	10.57 (0.44)	10.06 (0.37)

^a weighted average.

Table 7.4 gives a breakdown of the calculated ^{36}Cl concentration for each production channel. The total measured ^{36}Cl concentration is also included for comparative purposes.

Table 7.4 Breakdown of ^{36}Cl concentrations by production channel in the Wyangala surface samples.

Sample Name	Measured ^{36}Cl 10^2 atom g^{-1}	Reactions on Potassium			Reactions on ^{35}Cl		Reactions on Ca ^b 10^2 atom g^{-1}
		Spallation 10^2 atom g^{-1}	μ capture 10^2 atom g^{-1}	n capture ^a 10^2 atom g^{-1}	Cosmogenic 10^2 atom g^{-1}	Radiogenic 10^2 atom g^{-1}	
WYS3	44037 (1396)	35065	3981	1856	846	76	263
WYS4	25812 (886)	18791	3166	1445	773	142	163
WYBACK	19928 (711)	14789	2862	981	530	89	105

^a cosmogenic + radiogenic

^b spallation + negative muon capture.

The ^{36}Cl production from potassium accounts for ~90% of the total ^{36}Cl production. Potassium spallation, however, only accounts for ~80% of this, which is less than the proportion due to spallation in the Scottish samples, again because of the impact erosion has on the present samples.

The long term erosion rates were determined from the three surface samples from the measured ^{36}Cl concentrations, as described in § 3.3.3, and given in Table 7.5.

Table 7.5 Erosion Rates of the Wyangala surface samples.

Sample Name	Altitude	Erosion Rate
WYS3	610 m	2.64 (0.14) $\mu\text{m yr}^{-1}$
WYS4	570 m	6.21 (0.30) $\mu\text{m yr}^{-1}$
WYBACK	540 m	7.91 (0.37) $\mu\text{m yr}^{-1}$

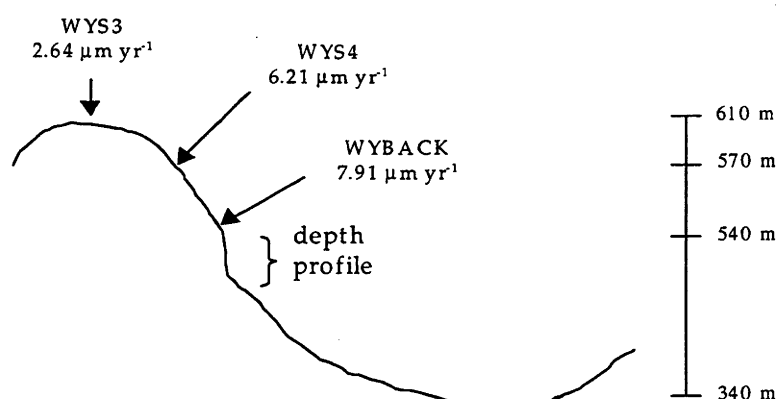


Figure 7.3 The erosion rate relative to the surrounding terrain. The erosion rate increases down the hill, as expected.

The erosion rate increases with increased distance from the top of the hill (see Figure 7.3), which is as expected for two reasons. Firstly, WYS3 and WYS4 were collected from tors which have a lower erosion rate than the surrounding bedrock. And secondly, erosion rates are typically lower on top of a hill as there is neither slope to increase erosive power of water flowing over the surface, nor any catchment area upslope to gather water.

The values also agree well with general estimates of erosion rates in the region. Limestone erosion rate in south eastern Australia have been measured by ^{36}Cl produced in calcite [Sto94] by employing the ^{36}Cl production rates for calcium spallation and negative muon capture on ^{40}Ca [Sto97, Sto98]. These give values between 11 and 36 $\mu\text{m yr}^{-1}$. Given the high susceptibility of limestone to erosion, it would be expected that these erosion rate would be significantly higher than those at Wyangala. However, they reflect the same time period as that of the Wyangala samples since they are both ^{36}Cl measurements. Therefore they provide a reliable upper limit of the erosion rate.

Consequently, the ^{36}Cl concentrations of the surface samples are in agreement with the scenario that an insignificant amount of rock or soil has been removed during the process of quarrying.

7.2 The Depth Profile

Sixteen samples were measured in the depth profile, down to a depth of 6.1 m. Table 7.6 gives the depth and thickness of the samples in the depth profile. For samples above 2 m, where ^{36}Cl production is dominated by spallation, the representative depth was calculated as the effective depth assuming the production rate had an exponential attenuation length of 160 g cm^{-2} . Below 2 m the representative depth was taken as the average depth of the sample. The corrections for altitude and shielding for the samples in the depth profile, are the same as for WYBACK (see Table 7.1).

To determine the mass shielding depths for the samples, the density of the granite was measured to be $2.643 \pm 0.003 \text{ g cm}^{-3}$. This measurement was made by determining the weight and volume of displaced water of 10 representative uncrushed samples (weighing up to ~130g) from various places in the profile.

Table 7.6 Depth of Wyangala samples.

Sample Name	Sample Thickness (cm)	Representative Depth (cm)	Mass shielding depth (g cm^{-2})
WYBACK	5	2.5	6.6
WYTOP	5	8.16	21.6
WY005-010	5	13.2	34.8
WY016-020	4	23.7	62.5
WY039-045	6	47.7	126
WY050-055	5	58.2	154
WY080-085	5	88.2	233
WY095-100	5	103	273
WY130-140	10	141	372
WY190-200	10	201	530
WY240-250	10	251	663
WY330-350	20	346	914
WY455-473	18	470	1241
WY535-550	15	548	1448
WY585-600	15	598	1581
WY600-610	10	611	1614

In Section 7.1, WYBACK was treated as a surface sample and a thickness correction was applied. In this section, however, WYBACK is considered part of the depth profile and is given a representative depth of 2.5 cm (as shown in Table 7.6) with no thickness correction, in line with the other depth profile samples.

Table 7.7 gives the chemical composition of the K-feldspar mineral separates for the depth profile and the calculated ^{36}Cl concentration. From the top of the profile to the bottom the total ^{36}Cl concentration decreases by 95%. Even for the deepest samples, however, a measurement uncertainty of ~5% was obtained.

Table 7.7 K-feldspar mineral separate compositions of the Wyangala depth profile.

Sample Name	Potassium (% wt)	Calcium (% wt)	Chloride (ppm)	Measured $^{36}\text{Cl}/\text{Cl}$ ($\times 10^{15}$)	$[\text{Cl}]$ (atom g^{-1}) ($\times 10^5$)
WYBACK	11.11 (0.07)	0.24 (0.10)	17.5 (0.2)	1883 (65)	20.12 (0.71)
WYTOP	11.05 (0.01)	0.20 (0.06)	23.8 (0.3)	See Table 7.3	18.70 (0.66)
WY005-010	11.47 (0.08)	0.22 (0.10)	25.5 (0.7)	951 (35)	17.74 (0.67)
WY016-020	10.99 (0.04)	0.12 (0.10)	21.5 (0.3)	See Table 7.3	15.61 (0.55) ^a
WY039-045	10.72 (0.04)	0.16 (0.10)	17.5 (0.3)	See Table 7.3	10.06 (0.37) ^a
WY050-055	10.77(0.05)	0.22 (0.07)	18.9 (0.3)	723 (26)	9.65 (0.36)
WY080-085	11.03 (0.11)	0.19 (0.10)	21.2 (0.3)	541 (21)	7.12 (0.28)
WY095-100	11.15 (0.07)	0.30 (0.10)	20.8 (0.3)	329 (13)	6.11 (0.24)
WY130-140	10.77 (0.02)	0.17 (0.10)	22.2 (0.4)	307 (14)	4.22 (0.20)
WY190-200	10.94 (0.03)	0.15 (0.10)	21.5 (0.4)	251 (10)	2.89 (0.12)
WY240-250	10.05 (0.05)	0.27 (0.04)	22.6 (0.3)	176 (7)	2.08 (0.09)
WY330-350	11.14 (0.03)	0.13 (0.10)	19.2 (0.2)	162 (7)	1.76 (0.08)
WY455-473	11.12 (0.05)	0.11 (0.10)	19.5 (0.3)	130 (6)	1.45 (0.07)
WY535-550	10.90 (0.05)	0.16 (0.10)	20.0 (0.2)	113 (5)	1.22 (0.06)
WY585-600	10.90 (0.04)	0.24 (0.06)	21.8 (0.3)	106 (5)	1.20 (0.06)
WY600-610	10.93 (0.04)	0.14 (0.10)	20.7 (0.3)	96 (5)	1.09 (0.05)

^a Weighted average of measurements on duplicate AgCl samples from the same K-feldspar, see Table 7.3.

The measured ^{36}Cl concentration with depth can be seen in Figure 7.4. A clear elbow can be seen at a depth of ~2m where the dominant production mechanism changes from potassium spallation to negative muon capture on potassium. Scatter is expected in this curve as a result in variations in the chemical composition of the samples, particularly in the potassium and chloride concentrations.

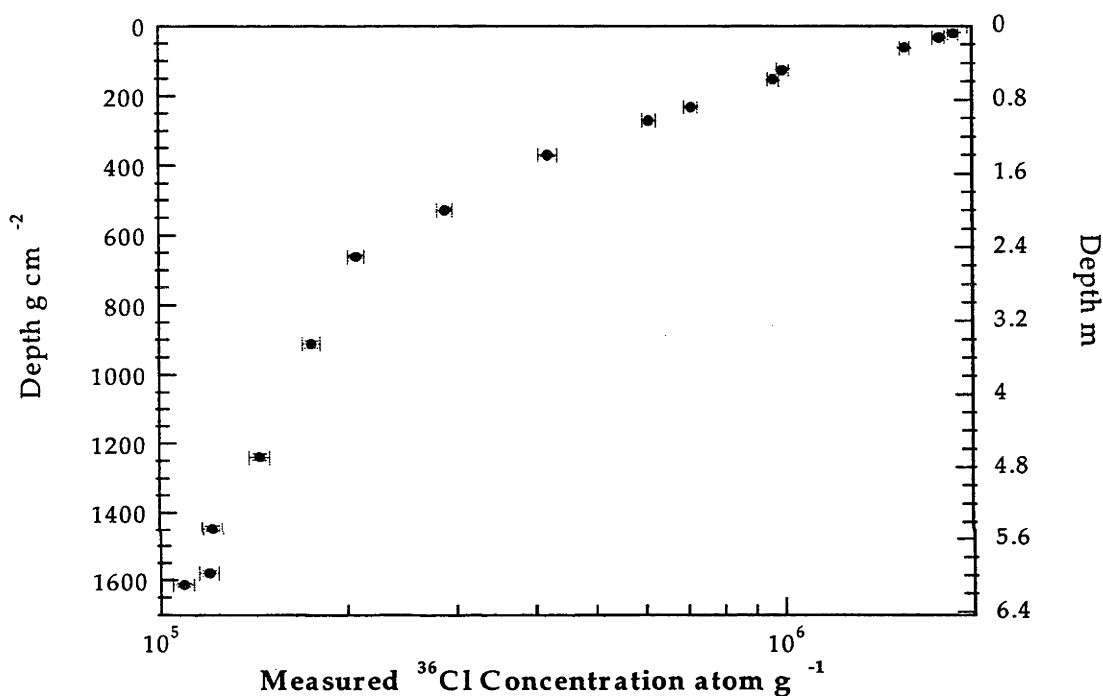


Figure 7.4 The measured ^{36}Cl concentration with depth. The error bars are the experimental uncertainty. Scatter in the profile is expected due to the variations in the chemical composition of the samples.

Table 7.8 gives the breakdown of the ^{36}Cl concentration by production rate for the depth profile. At the top of the profile ~15% of the potassium-produced ^{36}Cl is due to negative muon capture because the surface is eroding. This percentage increases with depth as the spallation component becomes less dominant. At a depth of 1.4m ~52% of the potassium-produced ^{36}Cl is due to negative muon capture, and at the bottom of the profile, ~79% of the potassium-produced ^{36}Cl is due to negative muon capture.

Chapter Seven ~ ³⁶Cl production due to negative muon capture: Wyangala depth profile

Table 7.8 Breakdown of the ³⁶Cl concentration by production channel in the Wyangala K-feldspar samples

Sample Name	Measured [³⁶ Cl] 10 ² atom g ⁻¹	Reactions on K			Reactions on ³⁵ Cl		Reactions on Ca ^b 10 ² atom g ⁻¹
		Spallation 10 ² atom g ⁻¹	μ capture 10 ² atom g ⁻¹	n capture ^a 10 ² atom g ⁻¹	Cosmogenic 10 ² atom g ⁻¹	Radiogenic 10 ² atom g ⁻¹	
WYBACK	20120 (711)	14242	2764	963	541	89	101
WYTOP	18699 (658)	12899	2749	1137	916	152	77
WY005-010	17740 (673)	12319	2819	1030	915	122	79
WY016-020	15614 (547)	9927	2631	830	687	109	37
WY039-045	10049 (371)	6515	2407	630	481	83	35
WY050-055	9649 (358)	5502	2349	595	498	104	41
WY080-085	7124 (278)	3432	2212	517	504	148	24
WY095-100	6110 (238)	2709	2144	439	446	112	32
WY130-140	4220 (196)	1409	1868	338	389	141	12
WY190-200	2894 (120)	531	1618	293	325	160	7
WY240-250	2076 (89)	213	1309	221	301	131	10
WY330-350	1761 (79)	49	1158	235	213	149	4
WY455-473	1448 (69)	6	885	168	153	113	4
WY535-550	1223 (59)	2	742	148	136	109	5
WY585-600	1199 (55)	1	674	167	155	147	8
WY600-610	1086 (54)	1	661	177	146	157	5

^a cosmogenic + radiogenic.

^b spallation + negative muon capture.

From the measured ³⁶Cl concentrations in the 16 depth profile mineral separates, the best values for the ³⁶Cl yield per stopped negative muon and the depth profile erosion rate were determined by calculating the expected ³⁶Cl concentration and minimising the χ^2 as described in § 3.3.

The depth profile erosion rate was determined to be 8.50 (0.22) $\mu\text{m yr}^{-1}$ and the value of Y_K was determined to be 5.80×10^2 atom per stopped μ^- with a reduced χ^2 of 1.17. From the goodness of fit of the model to the measured samples, Y_K has an uncertainty of 2.1×10^3 atom per stopped μ^- .

Figure 7.6 shows the χ^2 surface for Y_K and ϵ , while Figure 7.5 shows projections of the χ^2 surface for Y_K and ϵ respectively.

The value for the erosion rate determined during the minimisation of the depth profile is in good agreement with the value of 7.91 (0.37) $\mu\text{m yr}^{-1}$ which was determined in Section 7.1 using WYBACK as a surface sample. This gives further support to the conclusion that a negligible amount of the material has been removed by quarrying.

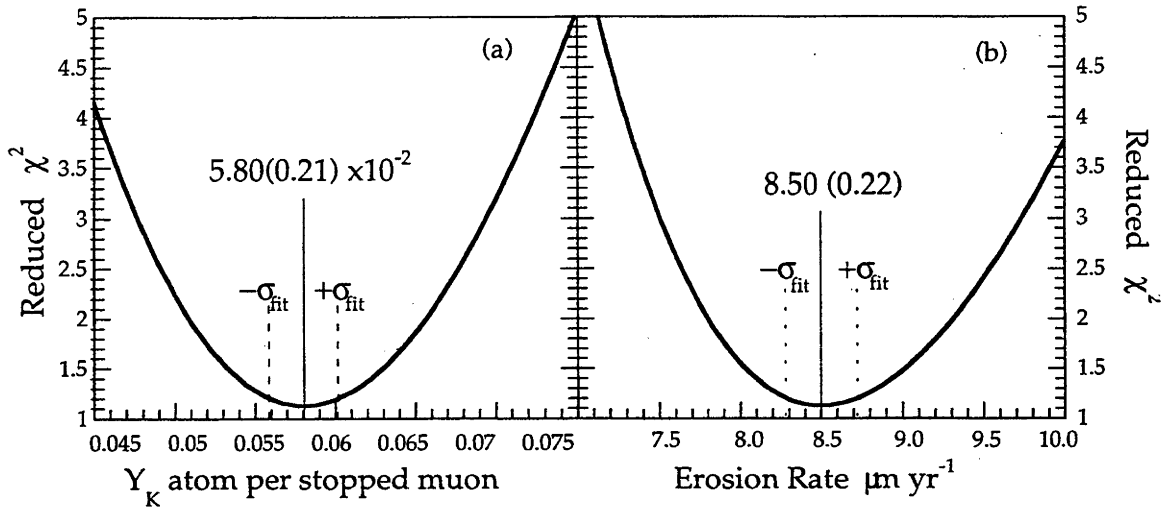


Figure 7.5 Projections of the χ^2 surfaces for a) Y_K and b) ϵ .

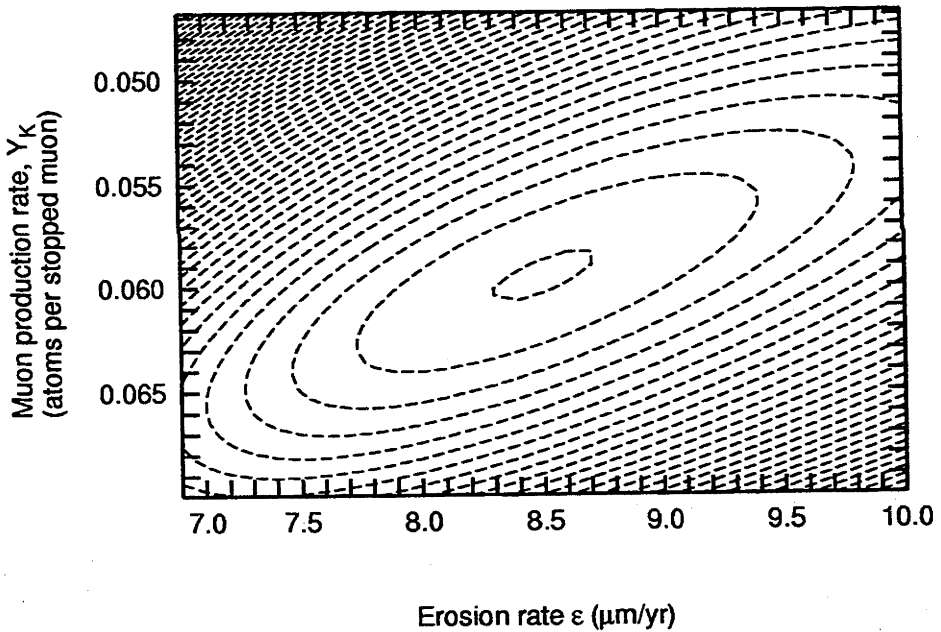


Figure 7.6 The χ^2 surfaces for Y_K and ϵ . The inner contour is at $\chi^2_{\min} = 1.2$, then the contours increases in steps of 1.0.

Figure 7.7 shows the measured ^{36}Cl concentration for each sample, as well as the calculated ^{36}Cl concentrations from potassium, and negative muon capture on ^{39}K . Also shown are profiles of the calculated ^{36}Cl concentration from negative muon capture on ^{39}K , the total production from potassium, and the production

from 10.9% K and 21 ppm Cl. These profiles are calculated using the average values for potassium, chloride and wholerock concentrations for the depth profile samples.

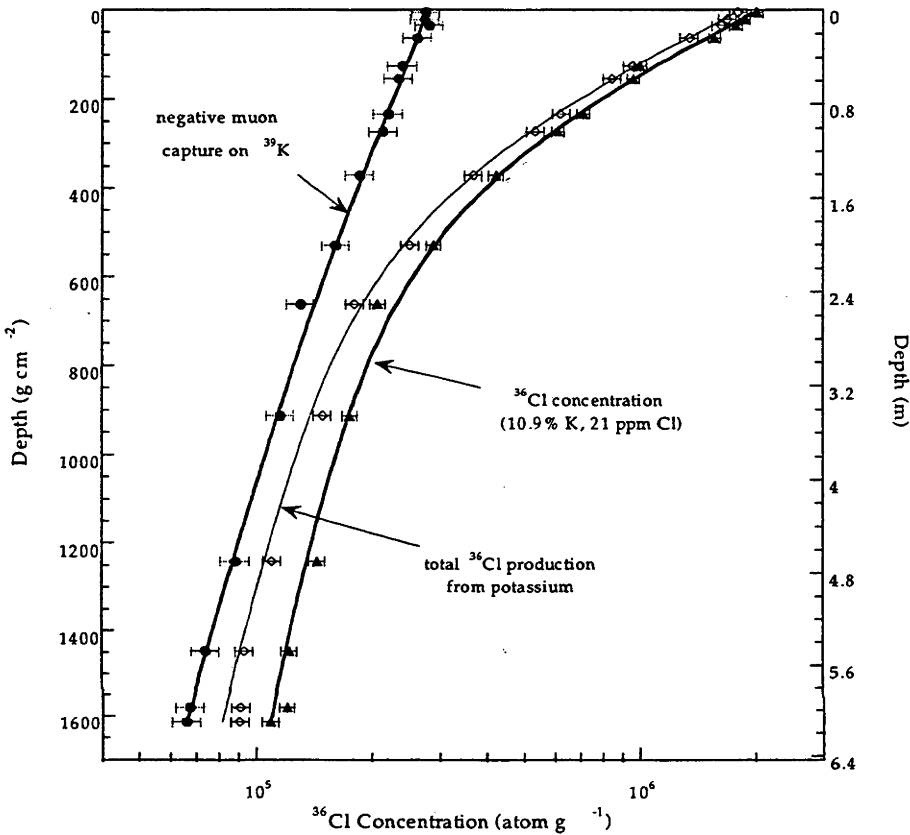


Figure 7.7 A breakdown of the ^{36}Cl concentrations in the Wyangala K-feldspar depth profile. The closed circles are the calculated ^{36}Cl concentration from negative muon capture on ^{39}K , the open diamonds are the total ^{36}Cl concentration due to potassium, and the closed triangles are the measured ^{36}Cl concentration. All the ^{36}Cl concentrations include $\pm 1\sigma$ error limits. The solid lines are the modeled ^{36}Cl concentration for negative muon capture, total production due to potassium and total production in the samples using the average values for the depth profile samples of: 10.9% K, 21 ppm Cl, $f_{35} = 0.00177$, $f_{39} = 0.00101$, $k_1 = 1.154$, $k_2 = -0.711$, $k_3 = 0.137$, $k_4 = 0.0547$, $L_{th} = 21.9$, $L_{epi} = 34.1$ and $P_{n,U+Th} = 16.56$.

7.3 Possible Sources of Uncertainty in the Derived Value of Y_K

Two possible sources of uncertainty in the derivation above require further consideration. The first is if the presumed top of the profile is not correct. As

discussed earlier, there are good grounds for believing that the top of the profile has been correctly identified. Nevertheless, the possibility that the quarrying may have removed unrecognised material is considered in Section 7.3.1.

Secondly, the value of Y_k is most tightly constrained by the deep samples where negative muon capture is the dominant production mechanism of ³⁶Cl. However, there is a considerable, 30-40%, contribution of ³⁶Cl from low-energy neutron capture on ³⁹K and ³⁵Cl in this region of the profile. Consequently, an adequate treatment of low-energy neutrons below ~1m in the profile is very important to the calibration of the value of Y_k . This is discussed in Section 7.3.2.

7.3.1 The Possible Effect of Quarrying on the Calibration

To test the possibility that material was removed during quarrying, the depth of each sample was increased by 20 cm and 40 cm to model the scenario that 20 cm or 40 cm of rock, or the equivalent thickness of soil, was removed. With the new sample depths the χ^2 minimisation was repeated to deduce the best fitting values of Y_k and ϵ , shown in Table 7.9.

Table 7.9 The values for ϵ and Y_k that minimise the χ^2 for the scenarios that 0 cm, 20 cm and 40 cm of rock (or equivalent density of soil) was removed prior to the quarrying.

Effective Depth Removed by Quarrying	ϵ $\mu\text{m yr}^{-1}$	Y_k ³⁶ Cl atoms (stopped μ)	Reduced χ^2
0 cm	8.50	5.80×10^{-2}	1.17
20 cm	5.52	5.02×10^{-2}	1.30
40 cm	3.81	4.60×10^{-2}	1.35

Table 7.9 shows that the effect of a 20 cm or 40 cm unrecognised loss of rock (53 or 106 g cm⁻² of soil) would be significant overestimation of the true erosion rate (2.5x for 40 cm), but it will only have a minor effect on the fit to the profile and on the value of Y_k (~20% for 40 cm). The large changes in the erosion rates are a result of the sensitivity of the spallation component of the ³⁶Cl profile to erosion, due to the short attenuation length of fast neutrons (~60 cm in granite). The muon flux, on the other hand, attenuates much more slowly with depth and therefore the value determined for Y_k is fairly insensitive to changes at the surface.

Therefore, performing the calibration assuming the profile surface is unaffected by quarrying does not lead to significant uncertainties in the value deduced for Y_K .

7.3.2 Chlorine-36 Produced by Low-energy Neutron Capture

For samples that were collected from below ~1m in the depth profile, the total ³⁶Cl production is dominated by negative muon capture on ³⁹K. Consequently these samples most tightly constrain the value of Y_K . However, the calculated ³⁶Cl production due to low-energy neutron capture on ³⁵Cl and ³⁹K accounts for 30% to 40% of the total ³⁶Cl concentration in samples in this depth region. Because the K/Cl ratio is almost constant throughout the profile, it is impossible from these data to determine separately the relative contributions of production by muon capture and muon-induced n-capture reactions. Consequently, the value determined for Y_K is vulnerable to uncertainties in the treatment of low-energy neutrons.

Table 7.10 presents a break down of the fraction of ³⁶Cl that is produced by low-energy neutron capture on ³⁹K and ³⁵Cl in each of the depth profile samples. The degree to which uncertainties in the low-energy neutron production rate will translate to uncertainties on the deduced value of Y_K depends on the total amount of ³⁶Cl produced by these reaction channels, i.e. from both ³⁵Cl and ³⁹K

Table 7.10 Breakdown of the ³⁶Cl concentration by low-energy neutron capture.

Sample Name	Radiogenic Neutrons		Spallogenic Thermal Neutrons		Spallogenic Epithermal Neutrons		Mu-genic Neutrons		Photonuclear Neutrons		Total ³⁶ Cl by low-energy neutrons
	³⁹ K	³⁵ Cl	³⁹ K	³⁵ Cl	³⁹ K	³⁵ Cl	³⁹ K	³⁵ Cl	³⁹ K	³⁵ Cl	
WYS3	0.1%	0.2%	3.9%	6.1%	0.5%	0.6%	0.6%	1.0%	0.1%	0.2%	13.2%
WYS4	0.3%	0.5%	4.6%	7.2%	0.4%	0.6%	1.1%	1.7%	0.2%	0.4%	17.0%
WYBACK	0.3%	0.4%	2.7%	3.8%	0.4%	0.5%	1.0%	1.4%	0.2%	0.3%	11.2%
WYTOP	0.4%	0.8%	3.5%	6.8%	0.4%	0.7%	1.3%	2.6%	0.3%	0.6%	17.4%
WY005-010	0.3%	0.7%	3.3%	6.6%	0.4%	0.7%	1.3%	2.6%	0.3%	0.6%	16.7%
WY016-020	0.4%	0.7%	3.0%	5.4%	0.4%	0.6%	1.4%	2.4%	0.3%	0.6%	15.3%
WY039-045	0.5%	0.8%	2.8%	4.2%	0.4%	0.5%	1.8%	2.6%	0.5%	0.7%	14.7%
WY050-055	0.7%	1.1%	2.7%	4.3%	0.4%	0.5%	2.0%	3.1%	0.5%	0.8%	16.2%
WY080-085	1.2%	2.1%	2.4%	4.2%	0.3%	0.5%	2.6%	4.5%	0.7%	1.3%	19.9%
WY095-100	1.1%	1.8%	2.1%	3.6%	0.3%	0.4%	2.9%	4.8%	0.8%	1.4%	19.3%
WY130-140	1.8%	3.3%	1.5%	2.8%	0.2%	0.3%	3.4%	6.3%	1.1%	2.0%	22.7%
WY190-200	3.0%	5.4%	0.8%	1.5%	0.1%	0.2%	4.4%	7.8%	1.5%	2.7%	27.3%
WY240-250	2.9%	5.9%	0.5%	0.9%	0.1%	0.1%	4.8%	9.7%	1.8%	3.6%	30.4%
WY330-350	5.3%	8.3%	0.1%	0.2%	0.0%	0.0%	5.3%	8.2%	2.2%	3.4%	33.1%
WY455-473	5.4%	8.5%	0.0%	0.0%	0.0%	0.0%	4.9%	7.8%	2.3%	3.7%	32.6%
WY535-550	5.7%	9.5%	0.0%	0.0%	0.0%	0.0%	4.8%	7.9%	2.4%	4.0%	34.4%
WY585-600	7.1%	12.8%	0.0%	0.0%	0.0%	0.0%	4.8%	8.8%	2.6%	4.6%	40.7%
WY600-610	8.0%	13.7%	0.0%	0.0%	0.0%	0.0%	4.8%	8.3%	2.6%	4.4%	41.9%

Spallogenic thermal neutrons are the dominant source of low-energy neutrons in the top metre of the profile and account for a total of ~10% of the ^{36}Cl produced at the surface. The magnitude of this contribution was calibrated, in effect, when the value of $\mathcal{P}_f(0)$ was determined in Chapter 5.

At depths greater than ~1 m the fraction of ^{36}Cl produced by low-energy neutron capture increases to as much as 40% at a depth of 6m. Roughly half of this contribution is due to radiogenic low-energy neutrons, since the Wyangala samples have high thorium concentrations. This low-energy neutron source is independent of depth (the fraction of radiogenic ^{36}Cl is only increasing with depth because the other production rates are decreasing), and has an uncertainty of ~7%.

Neutrons emitted following negative muon capture reactions on the various rock constituents are the dominant source of cosmogenic low-energy neutrons in the significant depth region for the calibration of Y_K , and account for ~13% of the total ^{36}Cl concentration in the K-feldspar mineral separates. This production channel depends on an assumed value of 0.5 for the average neutron yield per negative muon capture, Y_s . The value of Y_s is composition dependent; the adopted value is similar to that determined for limestone (0.44 ± 0.15 n per stopped μ), and the uncertainty is estimated at ~50%.

The ^{36}Cl contribution from photonuclear low-energy neutrons due to fast muons increases from 3% at 1m to 7% at 6m, and is expected to become the dominant ^{36}Cl production mechanism in K-feldspar between 10m and 20m as it diminishes less steeply with depth than the other cosmogenic production rates. This reaction channel depends on assumed values for the average neutron yield per photodisintegration, Y_f . Following Stone *et al.* [Sto98], a value of 1 n (disintegration)⁻¹ has been assumed, and the uncertainty is conservatively estimated to be ~50%.

Adopting 50% uncertainties on both Y_s and Y_f leads to an additional uncertainty of ~7.5% in Y_K . This is larger than the uncertainty in Y_K derived from the fit to the depth profile (~3.5%). Therefore the overall uncertainty is obtained by adding these two contributions together in quadrature to obtain an uncertainty of 8.3%.

To constrain the value of Y_K more precisely in future, the low-energy neutron capture production channel would need to be treated differently. It would be possible in principle to reduce the uncertainty arising from the neutron capture

mechanism by measuring independently the production of ^{36}Cl from chlorine alone. This could be accomplished by measuring the ^{36}Cl concentration in quartz mineral separates from the deeper samples, in the same way as for the Scottish samples (see Chapter 5). The ^{36}Cl contribution due to low-energy neutron capture on ^{39}K can then be calculated from the different cross sections and concentrations of ^{35}Cl and ^{39}K .

7.4 Discussion on the Negative Muon Capture on Potassium Production Rate

The ^{36}Cl yield per stopped negative muon is $5.80 (0.48) \times 10^{-2}$ atom per stopped μ^- . Assuming a negative muon stopping rate of $175 \mu^- \text{g}^{-1} \text{yr}^{-1}$ at the surface with an uncertainty of 10%, the ^{36}Cl production rate by negative muon capture is $10.2 (1.3) \text{atom (gK)}^{-1} \text{yr}^{-1}$ at sea level and high latitude. The largest source of error in this value comes from the uncertainty in the ^{36}Cl produced by low-energy neutron capture in the samples at depths below $\sim 1\text{m}$.

The surface ^{36}Cl production by negative muon capture on potassium per target nucleus is almost twice that for calcium, which is $5.3 \text{atom (gCa)}^{-1} \text{yr}^{-1}$ [Sto98]. This is because the emission channel from potassium is more favourable than the emission channel from calcium as fewer nucleons (and more specifically protons) need to be emitted to produce a ^{36}Cl nucleus. Calcium, however, has the advantage that there are rock types with larger target nuclei concentrations than is the case for potassium.

Negative muon capture on potassium accounts for $\sim 6\%$ of the total cosmogenic ^{36}Cl surface production at sea level and high latitude. If the surface is eroding, however, the contribution from negative muon capture will account for a significantly larger proportion of the ^{36}Cl at the surface. At Wyangala, where the erosion rate is $8.5 \mu\text{m yr}^{-1}$, the negative muon capture production mechanism accounts for 15% of the K-produced ^{36}Cl at the surface. Therefore, negative muon capture is important not only for samples collected from $>1\text{m}$ below the surface, but for eroding surfaces, and for surfaces that have had a short exposure time and only been exposed by a shallow excavation (1-2m). A detailed discussion of this issue can be found in Stone *et al.* [Sto98]. However, it should be noted that this

discussion refers to ^{36}Cl production from calcium, which is more sensitive to the effects of erosion as the ^{36}Cl production by negative muons on ^{40}Ca is ~11% of the calcium spallation production rate at sea level and high latitude. In comparison, the ^{36}Cl production by negative muons on ^{39}K is only ~6% of the potassium spallation production rate.

Chapter Eight

CONCLUSIONS

This thesis has presented the results of a complete calibration of the production rates of cosmogenic ^{36}Cl from potassium in the top 10 metres of the lithosphere. Three previous calibrations have been performed to determine the total surface production rate of ^{36}Cl from potassium. This work is an improvement on these studies as a result of three strategies:

1. The two main production mechanisms in the top 10 metres of the lithosphere: spallation and negative muon capture were determined separately by analysing surface samples and a depth profile,
2. ^{36}Cl measurements were made on samples with well constrained exposure histories.
3. The ^{36}Cl concentration measurements were made on pure K-feldspar mineral separates to maximise the potassium-produced ^{36}Cl . In addition, this virtually removed the ^{36}Cl contribution from calcium, iron and titanium, and minimised the ^{36}Cl contribution from ^{35}Cl .

The value of $P_{\text{K,sp}}(0)$ was deduced to be $161 (9) \text{ atom (gK)}^{-1} \text{ yr}^{-1}$ at sea level and high latitude (see Table 8.1). This was determined from 18 K-feldspar mineral separates prepared from samples exposed by the end of the Loch Lomond Readvance in Scotland, which has been assigned an exposure age of 11,600 years. The possible uncertainty in this value due to erosion or pre-exposure was modeled and shown to be insignificant within measurement uncertainties.

The ^{36}Cl yield per stopped negative muon, Y_{μ^-} , was deduced as $5.80 (0.48) \times 10^{-2}$. This value was determined from 16 samples measured in a depth profile down to 6.1 metres from a granite quarry. The quarry was located in Wyangala, south

eastern Australia, and the ^{36}Cl concentration was assumed to be at steady state for the whole depth profile. Assuming a negative muon stopping rate of $175 \mu \text{ g}^{-1} \text{ yr}^{-1}$ at sea level and high latitude (with a 10% uncertainty), the negative muon capture production rate is $10.2 (1.3) \text{ atom (gK)}^{-1} \text{ yr}^{-1}$.

Table 8.1 The results of this calibration, scaled to sea level and high latitude.

$P_{\text{K,sp}}(0)$	161 (9) atom (gK) $^{-1}$ yr $^{-1}$
Y_{K}	5.80 (0.48) $\times 10^{-2}$ ^{36}Cl atoms per stopped μ
$\mathcal{P}_f(0)$	740 (63) fast n (g air) $^{-1}$ yr $^{-1}$

For comparative purposes, the total production rate due to potassium at the surface at sea level and high latitude is shown in Table 8.2 as $174.4 \text{ atom (gK)}^{-1} \text{ yr}^{-1}$. To calculate this production rate a 2% contribution at the surface from low-energy neutron capture on ^{39}K was assumed. (This contribution will vary from sample to sample as it is composition dependent.) This total rate lies between the values of $225(25) \text{ atom (gK)}^{-1} \text{ yr}^{-1}$ [Swa94] and $154 (10) \text{ atom (gK)}^{-1} \text{ yr}^{-1}$ [Phi96], the two most recent calibrations of the total ^{36}Cl production due to potassium. (The earliest calibrated value of $107(8) \text{ atom (gK)}^{-1} \text{ yr}^{-1}$ [Zre91] was superseded [Phi96]).

Table 8.2 Comparison of Production Rates determined in this study to those determined in previous work.

This Work	Previous Work
$P_{\text{K,total}}(0) = 174.4 (9.1) \text{ atom (gK)}^{-1} \text{ yr}^{-1\text{a}}$	107(8) atom (gK) $^{-1}$ yr $^{-1}$ [Zre91] $P_{\text{K,total}}(0): 225(25) \text{ atom (gK)}^{-1} \text{ yr}^{-1}$ [Swa94] 154 (10) atom (gK) $^{-1}$ yr $^{-1}$ [Phi96]
$\mathcal{P}_f(0) = 740 (54) \text{ fast n (g air)}^{-1} \text{ yr}^{-1}$	586 (40) fast n (g air) $^{-1}$ yr $^{-1}$ [Phi96] ^b (551 (40) fast n (g air) $^{-1}$ yr $^{-1}$) ^c

^a $P_{\text{K,total}}(0) = (P_{\text{K,sp}}(0) + Y_{\text{K}} \times 175) \times 1.02$, assuming a negative muon stopping rate of $175 \mu \text{ g}^{-1} \text{ yr}^{-1}$ and 2% of the total surface production from potassium is produced by low-energy neutron capture on ^{39}K .

^b Assuming spallation as the only source of low-energy neutrons.

^c The value of [Phi96] corrected for low-energy neutrons produced by negative muon capture and photonuclear reaction induced by fast muons.

For 15 of the Scottish samples the contribution from low-energy neutron capture on ^{35}Cl was 24% to 37% of the total ^{36}Cl concentration. Therefore, a significant source of uncertainty on the determined value of $P_{\text{K,sp}}(0)$ was the

treatment of the low-energy neutrons at the surface. To overcome this, the value for the fast neutrons in air directly above the ground, $\mathcal{P}_f(0)$, was determined to be 740 (63) fast n (g air)⁻¹ yr⁻¹ from pure quartz mineral separates prepared from eight of the Scottish samples. The previously deduced value of $\mathcal{P}_f(0)$ of 586 fast n (g air)⁻¹ yr⁻¹ given in Table 8.2 was determined assuming all the low-energy neutrons at the air/ground boundary were derived from spallogenic reactions. If this value is lowered by 6% to a value of 551 (40) fast n (g air)⁻¹ yr⁻¹ (to account for low-energy neutrons produced by negative muon capture and photonuclear reactions due to fast muons) then it is 35% lower than the value of $\mathcal{P}_f(0)$ determined in this work.

There appeared to be a sample to sample variation amongst the eight quartz mineral separates due to the effects of local geometry on the low-energy neutron flux. Future studies that isolate the ³⁶Cl contribution from low-energy neutron capture on ³⁵Cl, combined with an improved method of modeling low-energy neutrons at the air/ground boundary [Phi01], will significantly reduce the uncertainty in determining the ³⁶Cl produced by low-energy neutron capture on ³⁵Cl, and enable the value of $P_{K,sp}(0)$ to be even more tightly constrained.

While muon capture is responsible for the majority of the ³⁶Cl in the samples below 2m in the depth profile, low-energy neutron capture on ³⁵Cl and ³⁹K accounted for an estimated 30% to 40% of the total ³⁶Cl produced in these samples. This contribution is only an estimate because it is based on assumed values of the average neutron yield per muon capture in the sample, Y_μ , and the average neutron yield per photodisintegration, Y_γ . The uncertainty from these assumed values is believed to be twice the statistical uncertainty in the derived value of Y_K . A more accurate account of low-energy neutron sources at depth will be needed in the future to constrain the value of Y_K more tightly. This could be achieved by applying a similar approach to that used for the Scottish samples and measuring the ³⁶Cl concentration in quartz mineral separates from below 2m, which would allow the contribution from ³⁵Cl to be determined, and from this, the contribution from ³⁹K can be deduced.

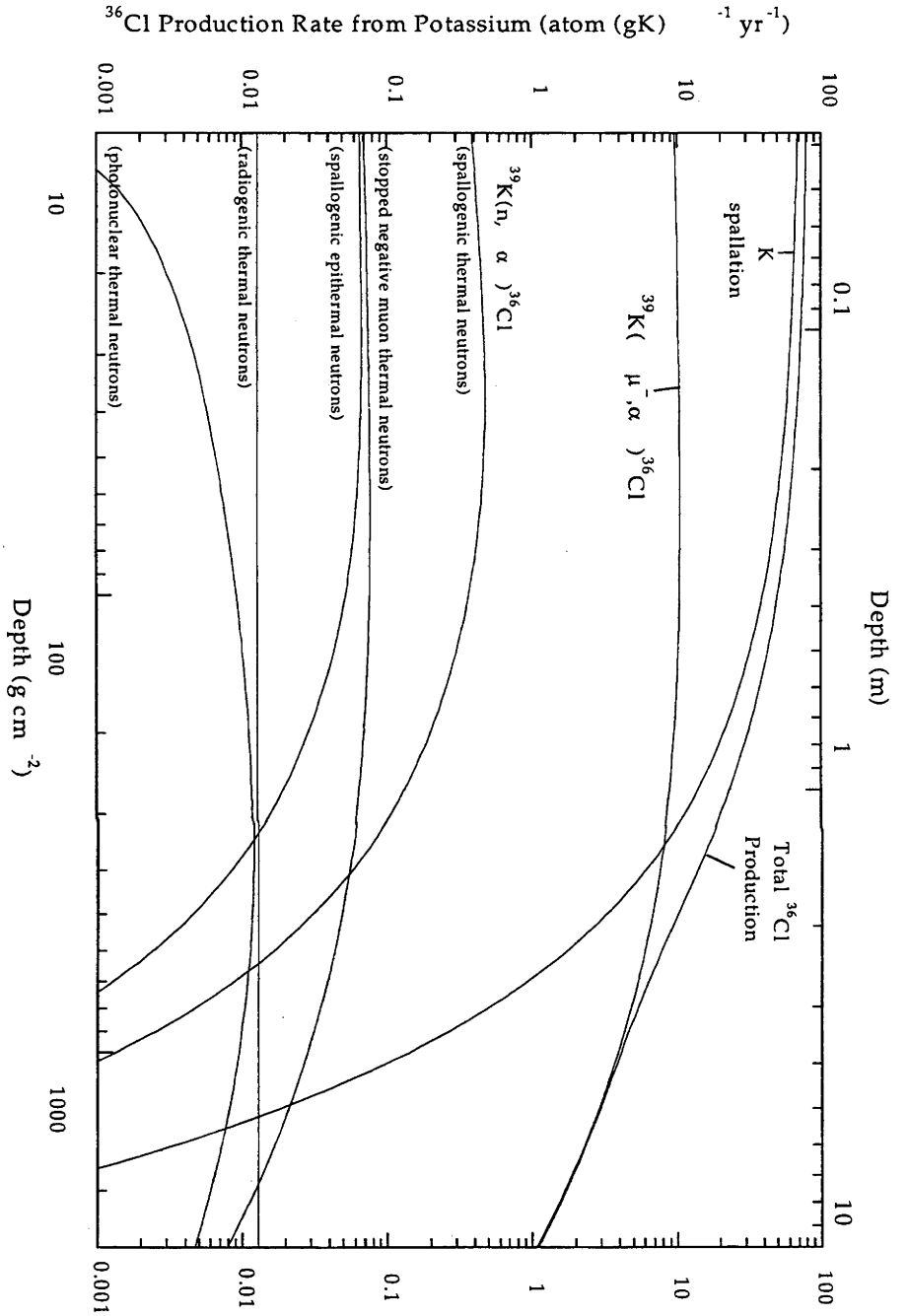


Figure 8.1 Summary of the ^{36}Cl production rates from potassium as a function of depth at sea level and high latitude. The composition dependent values used to calculate the low-energy neutron capture rates on ^{39}K are $f_{39} = 8.39 \times 10^{-4}$, $f_{\text{ep},39} = 1.02 \times 10^{-3}$, $k_1 = 1.129$, $k_2 = -0.696$, $k_3 = 0.0136$, $k_4 = 0.00544$, $L_{\text{th}} = 20.8$, $L_{\text{epi}} = 34.0$, $[U] = 3 \text{ ppm}$, $[Th] = 22 \text{ ppm}$.

For reference purposes and to enable a visual comparison of the different depth dependences and relative yields for the different production rates, Figure 8.1 gives a summary of the ^{36}Cl production rates from potassium at sea level and high latitude. It is of note that the spallation production profile is only dependent on the density of the rock and the potassium concentration (assumed to be 2.65 g cm^{-3} and 10%K respectively), while the negative muon capture production rate is also dependent on the particular rock or mineral type. The low-energy neutron capture production profile, however, is also dependent on the sample's chemical composition.

The ^{36}Cl production rates due to low-energy neutron capture on ^{35}Cl are not shown. Nevertheless, Figure 8.1 is useful for understanding the neutron production channels for ^{36}Cl , as they show the same behaviour as for low-energy neutron capture on ^{39}K . Therefore, the shapes of these curves can be used and scaled up or down depending on the chloride concentration. For example, if the chloride concentration were 11 ppm, then the ^{36}Cl contribution from low-energy neutron capture on ^{35}Cl would be the same as that shown in Figure 8.1 for ^{39}K with a 10% potassium concentration.

To conclude, this thesis presents the most comprehensive and accurate study currently available on the production *in-situ* of ^{36}Cl from potassium. The chief source of uncertainty remains the contribution from neutron-produced ^{36}Cl (from both ^{35}Cl and ^{39}K) at the air/ground boundary and at depth between 2 and 6 metres. Further investigations which isolate the low-energy neutron capture reaction on ^{35}Cl will provide significant insight into this production mechanism, as well as allowing an accurate determination of the ^{36}Cl contribution from this mechanism on a sample to sample basis. Applications of these production rates by themselves, and in conjunction with the calcium spallation and negative muon capture production rates [Eva93, Sto96, Sto98], will enable future measurements of precise exposure ages and erosion rate measurements in almost all rock-types.

Appendix A

EARLY ATTEMPTS AT ISOLATING THE ^{36}Cl PRODUCED BY LOW- ENERGY NEUTRON CAPTURE ON ^{35}Cl

A.1 Early Attempt: The Crushing Technique

The first attempt at isolating the low-energy neutron capture of ^{35}Cl pathway was very similar to that of Bierman *et al.* [Bie94] (see § 3.2.3) in that the sample was crushed to break open the fluid inclusions and release the chloride (and neutron-produced ^{36}Cl). Some of the K-feldspar mineral separate was placed in a mortar and pestle with deionised water and ground up to break open the fluid inclusions. The chloride (and neutron-produced ^{36}Cl) would be released directly into the water. The remaining K-feldspar was then removed by centrifuging and the solution was prepared for an AMS measurement using the method described in Section 4.2.2.

Initially an agate mortar and pestle was used. It was cleaned by scouring and rinsing multiple times in de-ionised water, and then soaking it for 24 hours or more in 10% HNO_3 . This process was repeated multiple times. Several samples were crushed and prepared as AgCl . Procedural blanks were prepared by placing distilled water in the mortar and pestle, grinding, collecting the water and preparing for an AMS measurement in the same way as a sample. The AMS

measurements revealed that the solutions contained extremely high ^{36}Cl concentrations, with $^{36}\text{Cl}/\text{Cl}$ ratios higher than 10^{-10} . This occurred for multiple samples and blanks. As the mortar and pestle had been very thoroughly cleaned, it was believed that the ^{36}Cl contamination came from the agate as some of it was abraded off with each crushing. Interestingly, the AMS measurements on the remaining K-feldspar, which had been rinsed several times in de-ionised water, gave ratios that were up to ~ 40 x lower and were in reasonable agreement with previous measurements, indicating the efficiency with which such rinses remove unbound chloride. As the previous history of the mortar and pestle was unknown, the cause of the contamination remains a mystery.

The second attempt at isolating the low-energy neutron capture of ^{35}Cl pathway again involved crushing the K-feldspar, this time using a new corundum mortar and pestle. A procedural blank was prepared in this mortar and pestle which showed it contained negligible ^{36}Cl . The available K-feldspar for a sample was now low, and as a consequence insufficient chloride could be released to guarantee sufficient AgCl could be precipitated for an AMS measurement (generally it was found that precipitating small amounts of AgCl , ≤ 2 mg, from a large volume of solution, ≥ 400 ml, gave very low yields). To address this chloride carrier was added. As a result, to calculate the $^{36}\text{Cl}_{n,\gamma}/\text{Cl}$ ratio from the $^{36}\text{Cl}/\text{Cl}$ ratio measured by AMS, the amount of chlorine released had to be measured and the yield from the chemical procedure had to be known. Given the difficulties of quantitatively transferring the solution and powdery K-feldspar into the beaker from the mortar and pestle, ambiguity in the yield was large enough to obscure any useful information from the final $^{36}\text{Cl}_{n,\gamma}/\text{Cl}$ ratios.

Upon reflection, there are several things that could be done to greatly improve the mortar and pestle technique of isolating the $^{36}\text{Cl}_{n,\gamma}/\text{Cl}$ ratio. The principle goal would be to increase the amount of chloride released so that carrier was not required and hence the yield would not be important. This could be achieved by crushing larger samples (about 8 g, depending on the size of the mortar and pestle) for longer amounts of time (≥ 5 min) to release as much chloride as possible. It should also be possible to use another mineral separate, or even a whole rock aliquot, in the crushing procedure than the precious (in this work) K-feldspar mineral separate. If a pure mineral separate was not used, it would also be possible to use a larger grain size, which should contain more

intact fluid inclusions. If there was still insufficient AgCl, NaBr carrier could be added to precipitate AgBr with the AgCl.

A.2 Second Attempt: The Quartz Samples

As crushing the samples had not been completely successful, another method was used to determine $^{36}\text{Cl}_{n,\gamma}/\text{Cl}$, similar to the technique used by Dep [Dep95]. Pure quartz mineral separates were prepared by the technique described in Section 4.2.1. Quartz was chosen as the best mineral as it is easy to separate (given its high resistance to HF [Kol92]) and while it contains no potassium, calcium or chloride in its crystal lattice, it often contains chloride in fluid inclusions [Nor89]. The method of extracting the chloride and preparing it as AgCl for an AMS measurement is described in Section 4.2.2. While this method was relatively simple and successful for most of the quartz samples, for some samples the AgCl precipitate was much smaller than expected and very hard to collect. It became evident afterwards that when the quartz dissolved it produced a very dense solution, and this inhibited flocculation of the AgCl into large clumps. If there was insufficient AgCl to flocculate, it would remain as tiny particles suspended in the solution and was not recoverable. To overcome this, NaBr carrier could be added to precipitate AgBr with the AgCl to aid flocculation (see § 4.2.2). The latter technique proved relatively successful for several Sierra Nevada samples; however as they are not directly relevant to this calibration, they shall not be discussed further.

Appendix B

THE SCOTTISH SAMPLES: SAMPLE LOCATIONS, WHOLE ROCK MEASUREMENTS AND DERIVED QUANTITIES

Table B.1 details the locations from which the Scottish samples were collected, as well as a breakdown of the correction factors applied to the sample to scale the production rate from the sample site to the surface production rate at sea level and high latitude with a 2π horizon (the typical location for which cosmogenic nuclide production rates are expressed).

Table B.1 Location Parameters and Correction Factors

Sample Name	Altitude	Latitude	Sample Type ^a	Alt/Lat Scaling		Horizon Scaling	Thickness Scaling		
				spallation	μ capture		spallation	Epithermal neutrons	Thermal neutrons
AT-10	570 m	58.5°	1A	1.754	1.318	0.900	0.972	1.034	1.246
AT-11	520 m	57.8°	1A	1.674	1.289	0.970	0.972	1.041	1.229
AT-12	520 m	57.8°	1A	1.674	1.289	0.925	0.984	1.028	1.136
AT-13	520 m	57.8°	1A	1.674	1.289	0.912	0.976	1.041	1.195
95Scot004	430 m	57.5°	1A	1.540	1.236	0.906	0.984	1.026	1.142
95Scot006	105 m	57.0°	2A	1.122	1.058	0.998	0.984	1.019	1.154
95Scot007	95 m	57.0°	2A	1.110	1.052	0.998	0.976	1.027	1.218
95Scot008	95 m	57.0°	2A	1.110	1.052	0.986	0.976	1.030	1.211
95Scot015	100 m	57.0°	2A	1.116	1.055	0.990	0.953	1.053	1.373
95Scot018	130 m	57.5°	1A	1.151	1.070	0.945	0.976	1.029	1.203
95Scot020	170 m	57.5°	1A	1.198	1.091	0.879	0.957	1.057	1.341
95Scot021	110 m	57.5°	1A	1.127	1.060	0.945	0.984	1.021	1.149
95Scot032	388 m	57.5°	2A	1.481	1.212	0.996	0.968	1.033	1.283
95Scot041 ^b	220 m	57.5°	2A	1.260	1.118	0.993	0.984	1.020	1.149
95Scot042 ^b	220 m	57.5°	2A	1.260	1.118	0.993	0.976	1.032	1.211
95Scot047	130 m	57.0°	2B	1.151	1.071	0.990	0.968	1.044	1.245
95Scot063	930 m	57.0°	2B	2.395	1.559	0.985	0.976	1.028	1.211
95Scot068	925 m	57.0°	2B	2.384	1.556	0.990	0.976	1.028	1.208

^a 1 = bedrock, 2 = glacially transported boulder, A = Torridon sandstone, B = granite.

^b Collected ~1.5 m apart on the top of the same very large erratic.

As the Scottish sample sites are at low altitude (less than 930m) and high latitude these corrections amount to less than a factor of 2.4 in all cases. In addition, because of the high latitude (almost 60°) no correction is required for changes in the Earth's magnetic field strength (as described in section 2.2.1).

Table B.2 presents the results of the major element measurements made on a whole rock fraction of the sample by X-ray fluorescence (see Chapter 4).

Table B.2 Whole Rock Major Element Concentrations (%wt)

Sample Name	SiO ₂	TiO ₂	Al ₂ O ₃	Fe ₂ O ₃	MnO	MgO	CaO	Na ₂ O	K ₂ O	P ₂ O ₅
AT-10	84.29	0.39	8.09	1.38	0.01	0.56	0.03	0.99	4.15	0.01
AT-11	77.51	0.64	11.11	1.29	0.01	0.98	0.05	1.17	5.25	0.01
AT-12	75.67	0.46	11.85	1.33	0.01	1.10	0.05	1.16	5.90	0.02
AT-13	76.29	0.32	11.73	1.52	0.01	1.12	0.05	1.24	5.70	0.02
95Scot004	71.90	0.53	13.57	3.09	0.03	1.87	0.16	2.43	4.71	0.09
95Scot006	80.87	0.46	9.45	2.32	0.02	0.37	0.28	2.76	3.30	0.04
95Scot007	84.19	0.31	7.89	1.32	0.01	0.48	0.07	1.72	3.38	0.02
95Scot008	80.46	0.48	8.95	1.86	0.08	0.71	0.64	2.12	3.22	0.05
95Scot015	76.72	0.30	12.16	1.81	0.01	0.57	0.13	3.44	4.36	0.02
95Scot018	76.19	0.21	8.70	1.36	0.16	1.46	2.00	2.03	3.05	0.09
95Scot020	80.30	0.28	10.50	1.78	0.01	1.06	0.06	1.33	4.62	0.03
95Scot021	82.26	0.40	8.97	1.83	0.01	0.68	0.08	1.54	4.09	0.02
95Scot032	85.72	0.22	7.51	0.83	0.01	0.79	0.06	1.60	3.15	0.02
95Scot041	83.14	0.28	8.42	1.40	0.01	0.83	0.05	1.23	3.97	0.01
95Scot042	80.41	0.56	9.09	2.41	0.02	1.16	0.06	1.12	4.07	0.03
95Scot047	69.54	0.50	13.18	5.07	0.10	0.11	1.30	4.27	4.57	0.07
95Scot063	75.75	0.11	13.38	1.01	0.03	0.09	0.48	3.84	5.36	0.05
95Scot068	75.49	0.14	13.33	1.15	0.03	0.09	0.48	3.81	5.41	0.06

Table B.3 Whole Rock Trace Element Concentrations (ppm)

Sample Name	B (ppm)	Gd (ppm)	Sm (ppm)	U (ppm)	Th (ppm)
AT-10	24.5	1.9	1.7	1.0	4.1
AT-11	47.0	2.6	3.8	1.4	7.1
AT-12	64.5	3.5	2.5	1.2	6.0
AT-13	68.0	2.2	3.0	1.2	5.5
95Scot004	41.5	2.3	2.1	2.2	8.8
95Scot006	5.9	0.9	1.0	0.8	3.0
95Scot007	16.5	2.1	2.6	1.1	5.2
95Scot008	18.0	4.8	6.2	1.5	6.5
95Scot015	18.0	2.2	3.1	1.2	5.0
95Scot018	23.0	4.8	5.7	2.3	3.8
95Scot020	40.0	3.0	2.4	1.2	4.6
95Scot021	20.0	4.0	3.6	1.2	5.3
95Scot032	17.0	1.7	2.5	0.9	4.9
95Scot041	21.0	1.5	2.2	1.4	4.5
95Scot042	27.5	2.8	4.2	2.2	6.5
95Scot047	3.0	19.2	19.9	0.6	10.4
95Scot063	3.8	6.4	8.2	8.5	45.1
95Scot068	2.5	8.1	10.6	15.8	58.1

Table B.3 presents the concentrations measured on whole rock of the important trace elements for low-energy neutron production and absorption.

The boron and gadolinium concentrations were measured by neutron activation/prompt gamma analyses, and the samarium, uranium and thorium concentrations were measured by ICP-MS.

Accurate measurements of whole rock concentrations are important as they are used, along with the K-feldspar chemical composition given in Table 6.1, to calculate the terms which define the ^{36}Cl production from low-energy neutron capture on ^{35}Cl and ^{39}K , such as the macroscopic cross section, which are given below in Table B.4. For example, many of the Torridon Sandstone samples have very high boron concentrations. As boron has a high thermal neutron capture cross section a lot of the thermal neutrons in the rock will be absorbed by boron instead of ^{35}Cl , which is shown by a high macroscopic cross section number (compare AT-13 with 95SCOT006 for instance).

Table B.4 Derived Quantities for Scottish K-feldspar Mineral Separates.

Sample Name	$\Sigma \sigma_i N_i$ $\times 10^3$	$\Sigma I_i N_i$ $\times 10^3$	Spallogenic Thermal Neutrons			Spallogenic Epithermal Neutrons			Percent neutrons captured by:	
			k_1	k_2	L_{th}	k_3	k_4	L_{epi}	$^{35}\text{Cl}^a$	$^{39}\text{K}^b$
AT-10	5.276	2.609	1.116	-0.745	24.516	0.129	0.0517	34.345	3.21%	0.25%
AT-11	6.796	3.224	1.079	-0.676	21.876	0.159	0.0636	31.287	2.73%	0.21%
AT-12	7.765	3.605	1.061	-0.640	20.542	0.177	0.0707	29.698	3.00%	0.19%
AT-13	7.635	3.647	1.062	-0.644	20.654	0.179	0.0715	29.441	3.17%	0.18%
95Scot004	6.767	3.297	1.085	-0.682	21.824	0.164	0.0655	30.804	3.09%	0.18%
95Scot006	4.447	2.354	1.130	-0.785	26.653	0.118	0.0471	36.095	3.09%	0.18%
95Scot007	4.808	2.376	1.120	-0.764	25.701	0.118	0.0471	36.014	4.44%	0.26%
95Scot008	5.725	2.600	1.110	-0.727	23.642	0.129	0.0516	34.563	3.17%	0.22%
95Scot015	5.580	2.686	1.112	-0.733	23.932	0.134	0.0535	33.981	3.78%	0.22%
95Scot018	5.761	2.638	1.089	-0.709	23.971	0.131	0.0523	34.876	4.19%	0.24%
95Scot020	6.358	3.019	1.100	-0.703	22.354	0.149	0.0597	31.964	3.71%	0.20%
95Scot021	5.653	2.620	1.117	-0.735	23.675	0.130	0.0521	34.262	4.50%	0.22%
95Scot032	4.556	2.283	1.124	-0.776	26.337	0.113	0.0452	36.648	3.79%	0.26%
95Scot041	5.452	2.530	1.115	-0.740	24.166	0.125	0.0502	34.952	5.06%	0.24%
95Scot042	5.731	2.739	1.110	-0.727	23.588	0.136	0.0545	33.619	4.89%	0.23%
95Scot047	8.947	3.002	1.114	-0.650	18.922	0.153	0.0610	32.198	0.30%	0.10%
95Scot063	5.722	2.472	1.125	-0.737	23.683	0.124	0.0496	35.501	0.51%	0.25%
95Scot068	6.073	2.484	1.125	-0.727	22.999	0.125	0.0499	35.435	0.37%	0.23%

^a equivalent to $(f_{35} + f_{epi,35}) \times 100$

^b equivalent to $(f_{39} + f_{epi,39}) \times 100$

Appendix C

THE POSSIBLE INFLUENCE OF PRE-EXPOSURE AND EROSION ON THE SCOTTISH SAMPLES

A simple exposure history has been assumed in this study, that is, the surface ^{36}Cl concentration is negligible at the end of the Loch Lomond Readvance, followed by continuous exposure on a static surface up to the present. To be confident that a systematic error is not being incorporated into the calibration, the probable effects of pre-exposure and erosion are considered below.

C.1 Pre-exposure

There are two possibilities for pre-exposure.

1. Loch Lomond glaciers may not have removed sufficient material from the rock surface to reduce the surface ^{36}Cl concentration to (within experimental uncertainty) zero at the retreat of the Loch Lomond Readvance.
2. Samples from the glacially transported boulders may have been taken from sides that don't have an exposure age of 11,600. This could be because the sample surface was the original exposed surface prior to the erratic being extracted from its host rock, or that the erratic was dislodged from its host rock significantly before the end of the Loch Lomond Re-advance.

There is evidence of many glacial episodes in Britain and Northern Europe in the Quaternary period. Following the Anglian glacier there were four possible glacial periods before the Late Devensian Substage (which include the Dimlington and Loch Lomond Stadials, discussed in §3.3.1). These events are not sufficiently constrained to speculate on the actual exposure history in Scotland over the last 430,000 years, but they do strongly suggest it is very unlikely that the surfaces would have been at steady state at the onset of the Loch Lomond Readvance. This reduces the chances of pre-exposure as the lower the ^{36}Cl concentration at the beginning of the Loch Lomond Readvance, the less material that would have had to be removed to reach a ^{36}Cl concentration that is less than the concentration measurement uncertainty 11,600 years later.

To demonstrate this point, if we assume a spallation production rate of $162 \text{ atoms (gK)}^{-1} \text{ yr}^{-1}$ and a negative muon capture production rate of $10 \text{ atoms (gK)}^{-1} \text{ yr}^{-1}$, then over 11,600 years of exposure the surface ^{36}Cl concentration is $6.85 \times 10^7 \text{ atom (gK)}^{-1}$. Assuming a 5% measurement uncertainty, then the ^{36}Cl surface concentration just after the retreat of the Loch Lomond Readvance must be $\leq 3.4 \times 10^6 \text{ atom (gK)}^{-1}$ for pre-exposure to be less than the experimental uncertainty. The amount of material which the Loch Lomond Readvance must have removed to reach this concentration depends on the ^{36}Cl concentration at the onset of the Loch Lomond Readvance, as shown in Table C.1.

Table C.1 The thickness of material which must have been removed by the Loch Lomond Readvance to satisfy the condition of negligible pre-exposure.

^{36}Cl Concentration prior to the onset of Loch Lomond Readvance	Net Accumulation Time	Spallation Only	Spallation + Negative Muon Capture
Steady state	$\geq 2.88 \text{ Ma}$	1.8 m	3.3 m
$\frac{3}{4}$ steady state	$\sim 0.6 \text{ Ma}$ (2 ^{36}Cl half lives)	1.7 m	2.5 m
$\frac{1}{2}$ steady state	$\sim 0.3 \text{ Ma}$ (1 ^{36}Cl half lives)	1.4 m	1.9 m
$\frac{1}{4}$ steady state	$\sim 125 \text{ ka}$	1.0 m	1.2 m

To reduce the possibility of pre-exposure, samples were chosen to maximise the material removed during the Loch Lomond Readvance. The glacially transported boulders were at least $1.5\text{m} \times 1.5\text{m} \times 1.5\text{m}$, while the roches moutonnées were sampled on the downward side where the step up was at least

1 m. Consequently, it can be assumed that at least 1 m of material was removed above each sample. This implies that pre-exposure is negligible if the surface concentration prior to the onset of the Loch Lomond Readvance was $\leq \frac{1}{4}$ steady state. This would be the case if the four or more glacial episodes (including the Dimlington Stadial) since the Anglian Icesheet removed >2.5 m. While there is no hard evidence to prove this, it seems a very likely scenario. Therefore, although pre-exposure can not be categorically dismissed, it seems improbable that is a large source of systematic uncertainty in this calibration.

An additional consideration for pre-exposure is if some of the boulders landed with a surface that was pre-exposed facing upward, or that they were extracted from their host rock a considerable time before the retreat of the Loch Lomond Readvance. While the strict sampling criteria for glacially transported boulders reduced this probability, it is possible that one or two pre-exposed boulders slipped through. To determine the likelihood of this, the minimised potassium spallation production rate using only the glacially transported boulders was calculated to be $158 (9) \text{ atom (gK)}^{-1} \text{ yr}^{-1}$, compared with the minimized potassium spallation production rate using only the bedrock samples of $165 (10) \text{ atom (gK)}^{-1} \text{ yr}^{-1}$. As the values are in excellent agreement, the amount of pre-exposure in the glacially transported boulders is not significant compared to other sources of uncertainty.

C.2 Erosion

To perform this calibration it has been assumed that the rock surfaces have not eroded significantly since the retreat of the Loch Lomond Readvance. While an important part of the fieldwork was to find surfaces that showed no evidence of erosion, the nature of the samples collected (to minimise pre-exposure) made it difficult to prove the absence of erosion. The glacially transported rock-fall boulders will obviously not be glacially striated as they stayed on top of the ice, while the down-flow sides of roches moutonnées, by their nature, aren't glacially striated (with rock being removed by "plucking" rather than "scouring"). It is possible, therefore, that some surfaces may have eroded since the retreat of the Loch Lomond Readvance and this needs to be considered as a source of systematic uncertainty.

To estimate the possible effect of erosion on this calibration, variations in the surface concentration with erosion are shown for two K-feldspar samples in Figures C.1 and C.2. As the spallation production rate has a very different depth dependence compared to the low-energy neutron capture production rate, the effect of erosion on the surface concentration is strongly dependent on the proportion of ^{36}Cl produced by spallation compared to the amount produced by low-energy neutron capture on ^{35}Cl . As a result, the K-feldspar samples are broken into two groups, the high potassium, high chloride concentrations of the Torridon sandstone samples, as represented by the sample 95SCOT004 in Figure C.1, and the high potassium, low chloride concentrations of the granite samples, as represented by the sample 95SCOT068 in Figure C.2.

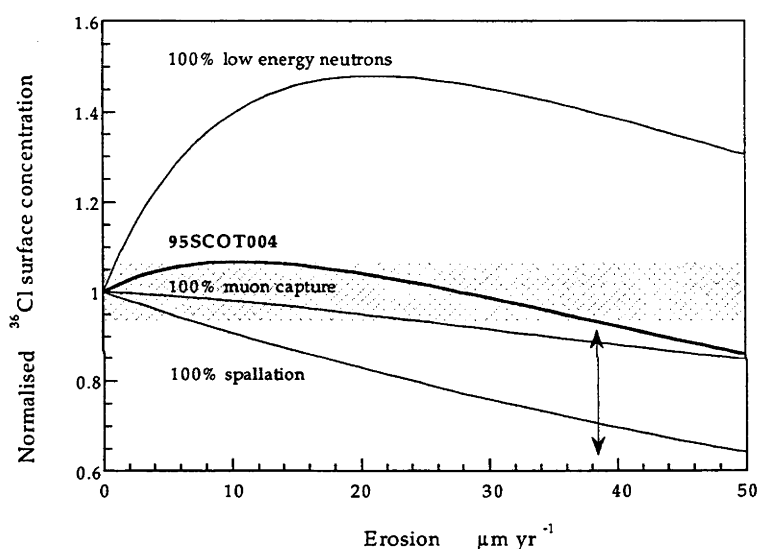


Figure C.1 The effects of erosion on the surface ^{36}Cl concentration, normalised to surface ^{36}Cl concentration with zero erosion for the K-feldspar mineral separate 95SCOT004. Also shown is the effect erosion would have if the ^{36}Cl production was due to 100% spallation, 100% negative muon capture or 100% low-energy neutron capture on ^{35}Cl . The mineral separate has 207 ppm Cl- and 10.4 %K, and therefore $\sim 2/3$ of the ^{36}Cl production is due to spallation. The shaded region represents the 6% uncertainty on the measured ^{36}Cl concentration. The arrow represents the minimum erosion rate required to influence the calibration.

The K-feldspar mineral separate 95SCOT004 has approximately average concentrations of chloride and potassium for this group, with 207 ppm Cl- and 10.4%K. As a result, approximately two thirds of the ^{36}Cl production in this sample is due to spallation and approximately one third is due to low-energy

neutron capture. (To simplify these calculations, only spallation and negative muon capture on ^{39}K , and spallogenic thermal and epithermal neutron capture on ^{35}Cl were considered.)

Figure C.1 show the surface concentration as a function of erosion rate normalised to the surface concentration with no erosion, so that only the chemical composition of the sample is important. Three of the curves show the erosion dependence if the ^{36}Cl production due solely to low-energy neutron capture on ^{35}Cl , spallation on ^{39}K , and negative muon capture on ^{39}K . The middle line is the combination of these production channels for 95SCOT004, assuming 5% of the surface production due to potassium is by negative muon capture. The shaded region represents the 6% measurement uncertainty in the ^{36}Cl concentration measurement for 95SCOT004. When the curves are within this uncertainty region, the erosion rate doesn't have a distinguishable effect on the surface concentration. Only a very small erosion rate would be required to make a large impact on the surface concentration if the ^{36}Cl production was due solely to spallation or low-energy neutron capture. The ^{36}Cl concentration due to negative muon capture however, is less sensitive to the erosion rate as production due to negative muons diminishes less steeply with depth than fast neutrons. The particular combination of the three production mechanisms for 95SCOT004, however, means that the sample is only slightly affected by low erosion rates. (This feature of a combined spallation/low-energy neutron capture production rate is also discussed in references [Liu94, Dep95, Mas95]). The effect of erosion becomes distinguishable from no erosion at $\epsilon > \sim 0.0038 \text{ cm yr}^{-1}$. During the time since the retreat of the Loch Lomond Readvance, this is equivalent to the removal of 44 cm of rock from the surface, which is considered a highly unlikely event, and therefore erosion from the surface does not make a large contribution to the calibration uncertainty for the Torridon sandstone samples.

The low chloride K-feldspar mineral separates are represented by 95SCOT068 which has 20.5ppm Cl and 10.9%K. Consequently, only 10% of the ^{36}Cl production is due to low-energy neutron capture on ^{35}Cl and this sample is dominated by spallation. As this sample was collected from high altitude it has a higher ^{36}Cl concentration than 95SCOT004 which was easier to measure precisely, so that the shaded region is smaller with an uncertainty of 4%.

For this sample, the erosion rate only needs to be $\geq 0.0012 \text{ cm yr}^{-1}$ for it to have a distinguishable effect on the ^{36}Cl surface concentration. During the time since the retreat of the Loch Lomond Readvance, this is equivalent to the removal of 13 cm of rock from the surface. Therefore these samples are much more sensitive to the effects of erosion, which is significant as these samples played such a dominant role in constraining the potassium spallation production rate. However, it seems likely that any surface from which 13 cm of rock had been removed would have been recognised in the field and avoided, so this isn't considered a large contributor to the uncertainty in the calibration.

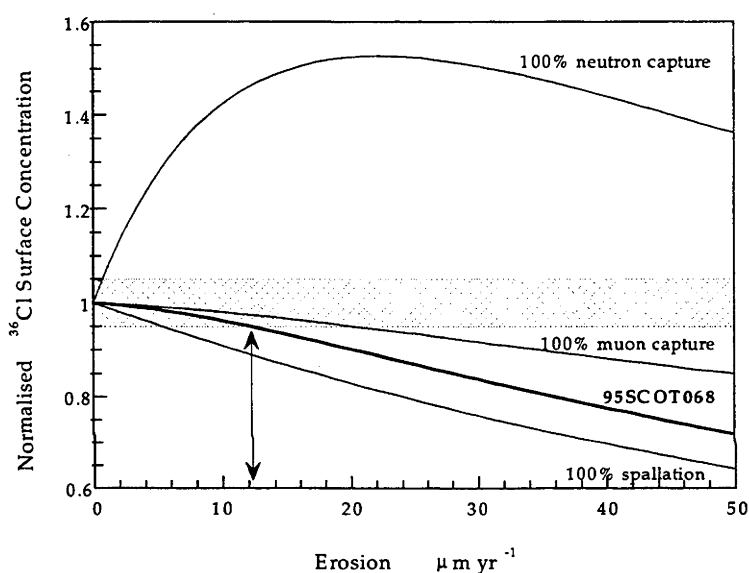


Figure C.2 The effects of erosion on the surface ^{36}Cl concentration, normalised to surface ^{36}Cl concentration with zero erosion for the K-feldspar mineral separate 95SCOT068. Also shown is the effect erosion would have if the ^{36}Cl production was due to 100% spallation, 100% negative muon capture or 100% low-energy neutron capture on ^{35}Cl for this sample. The mineral separate has 20.5 ppm Cl- and 10.9 %K, and therefore ~90% of the ^{36}Cl production is due to spallation. There is a 4% uncertainty in the measured ^{36}Cl concentration. The arrow represents the minimum erosion rate required to influence the calibration.

Appendix D

THE WYANGALA SAMPLES: SAMPLE LOCATIONS, WHOLE ROCK MEASUREMENTS AND DERIVED QUANTITIES

D.1 The Surface Samples

Tables D.1 and D.2 shows the whole rock major element concentrations and trace element concentrations, respectively. The whole rock major element concentrations and uranium and thorium concentrations were measured by XRF, and boron, gadolinium and samarium were measured by ICP-MS (see § 4.2.3).

Table D.1 Whole Rock Major Element Chemistry of the Wyangala surface samples (% wt).

Sample Name	SiO ₂	TiO ₂	Al ₂ O ₃	Fe ₂ O ₃	MnO	MgO	CaO	Na ₂ O	K ₂ O	P ₂ O ₅
WYS3	74.28	0.41	13.11	2.69	0.04	0.73	1.73	2.45	4.46	0.11
WYS4	73.16	0.49	13.06	3.17	0.04	0.87	1.71	2.37	4.69	0.13
WYBACK	72.28	0.48	13.75	3.13	0.04	0.89	1.80	2.50	5.01	0.10

Table D.2 Whole Rock Trace Element Concentrations of the Wyangala surface samples.

Sample Name	B (ppm)	Gd (ppm)	Sm (ppm)	U (ppm)	Th (ppm)
WYS3	1.8	7.5	9.0	2	21
WYS4	2.1	14.3	17.6	3	29
WYBACK	1.6	13.1	15.7	3	22

The values in Table D.3 are the quantities derived to determine the low-energy neutron production rate, calculated from the values in Tables D.1, D.2 and 7.2.

Table D.3 Derived Quantities for the Wyangala surface samples.

Sample Name	$\Sigma \sigma_i N_i$ $\times 10^{-3}$	$\Sigma I_i N_i$ $\times 10^{-3}$	Spallogenic Thermal Neutrons			Spallogenic Epithermal Neutrons			Percent neutrons captured by:	
			k_1	k_2	L_{th}	k_3	k_4	L_{epi}	$^{35}\text{Cl}^a$	$^{39}\text{K}^b$
WYS3	5.973	2.509	1.128	-0.691	20.572	0.1271	0.0508	34.210	0.34%	0.23%
WYS4	7.548	2.652	1.133	-0.736	23.103	0.1345	0.0538	35.131	0.28%	0.19%
WYBACK	7.365	2.677	1.129	-0.696	20.825	0.1360	0.0544	34.048	0.28%	0.21%

^a equivalent to $(f_{35} + f_{epi,35}) \times 100$

^b equivalent to $(f_{39} + f_{epi,39}) \times 100$

D.2 The Depth Profile

The whole rock major element chemistry for samples in the depth profile is presented in Table D.4 and the trace element chemistry in Table D.5. The whole rock major element concentrations and uranium and thorium concentrations were measured by XRF, and boron, gadolinium and samarium were measured by ICP-MS (see § 4.2.3).

Table D.4 Whole Rock Major Element Chemistry of the Wyangala depth profile (% wt).

Sample Name	SiO ₂	TiO ₂	Al ₂ O ₃	Fe ₂ O ₃	MnO	MgO	CaO	Na ₂ O	K ₂ O	P ₂ O ₅
WYBACK	72.28	0.48	13.75	3.13	0.04	0.89	1.80	2.50	5.01	0.10
WYTOP	72.85	0.50	13.33	3.16	0.04	0.91	1.92	2.49	4.60	0.10
WY005-010	74.69	0.40	12.88	2.57	0.03	0.72	1.77	2.44	4.63	0.10
WY016-020	71.70	0.49	13.81	3.11	0.04	0.89	1.67	2.48	5.49	0.10
WY039-045	72.91	0.37	13.41	2.38	0.03	0.67	1.50	2.34	5.89	0.10
WY050-055	71.37	0.47	14.39	2.98	0.04	0.84	1.88	2.62	5.55	0.10
WY080-085	72.42	0.51	13.29	3.27	0.04	0.93	2.00	2.54	4.59	0.11
WY095-100	73.43	0.47	12.98	3.06	0.04	0.87	1.94	2.46	4.36	0.10
WY130-140	72.53	0.50	13.36	3.17	0.04	0.87	1.88	2.46	4.88	0.11
WY190-200	71.65	0.51	13.56	3.32	0.04	0.92	1.98	2.49	4.75	0.12
WY240-250	72.16	0.50	13.40	3.10	0.04	0.86	1.83	2.46	5.12	0.12
WY330-350	70.97	0.58	13.98	3.70	0.05	1.02	2.05	2.55	4.86	0.12
WY455-473	71.36	0.47	14.10	3.04	0.04	0.84	1.98	2.62	5.16	0.11
WY535-550	71.71	0.49	13.44	3.22	0.04	0.90	1.89	2.49	4.94	0.10
WY585-600	72.58	0.46	13.51	2.95	0.03	0.85	2.00	2.58	4.72	0.10
WY600-610	72.12	0.51	13.45	3.21	0.04	0.90	2.00	2.56	4.68	0.11

The chemical composition of the rock is very uniform and the numbers also agree well with trace element measurements made on other granite samples from the Wyangala pluton [Cha97].

Table D.5 Whole Rock Trace Element Concentrations of the Wyangala depth profile.

Sample Name	B (ppm)	Gd (ppm)	Sm (ppm)	U (ppm)	Th (ppm)
WYBACK	1.6	13.1	15.7	3	22
WYTOP	3.8	5.6	6.3	3	22
WY005-010	2.8	9.2	10.9	2	20
WY016-020	2.1	10.1	12.4	2	23
WY039-045	3.9	14.7	17.5	3	19
WY050-055	2.2	9.2	11.4	3	21
WY080-085	5.0	10.8	12.4	4	25
WY095-100	3.7	9.8	11.4	3	21
WY130-140	4.3	10.5	12.3	4	25
WY190-200	3.0	10.5	12.2	4	29
WY240-250	1.5	6.5	7.7	3	23
WY330-350	4.3	7.9	8.9	4	29
WY455-473	4.6	11.5	13.6	4	22
WY535-550	4.3	12.1	14.3	3	24
WY585-600	4.5	10.5	12.1	4	24
WY600-610	2.1	8.5	10.2	4	28

Table D.6 contains the derived quantities that determine the low-energy neutron production rate, which are calculated from the values in Tables D.4, D.5, 7.7. It is of note that because of the consistently low chloride concentrations and high potassium concentrations for the entire depth profile, the percentage of low-energy neutrons captured by ^{35}Cl is only ~60% higher than the percentage captured by ^{39}K , despite the large difference in the cross sections.

Table D.6 Derived Quantities for Wyangala K-feldspar mineral separates.

Sample Name	$\Sigma \sigma_i N_i$ $\times 10^3$	$\Sigma I_i N_i$ $\times 10^3$	Spallogenic Thermal Neutrons			Spallogenic Epithermal Neutrons			Percent of low-energy neutrons captured by:	
			k_1	k_2	L_{th}	k_3	k_4	L_{epi}	$^{35}\text{Cl}^a$	$^{39}\text{K}^b$
WYBACK	7.365	2.677	1.129	-0.696	20.82	0.1345	0.0538	34.05	0.28%	0.21%
WYTOP	5.804	2.612	1.131	-0.740	23.44	0.133	0.0531	34.44	0.43%	0.23%
WY005-010	6.359	2.538	1.133	-0.725	22.38	0.129	0.0514	34.91	0.44%	0.23%
WY016-020	6.886	2.716	1.127	-0.706	21.58	0.138	0.0553	33.86	0.35%	0.21%
WY039-045	6.899	2.704	1.123	-0.703	21.61	0.137	0.0548	34.02	0.28%	0.20%
WY050-055	6.732	2.719	1.129	-0.712	21.80	0.138	0.0554	33.81	0.31%	0.21%
WY080-085	6.345	2.683	1.127	-0.721	22.44	0.136	0.0545	34.01	0.36%	0.22%
WY095-100	6.574	2.595	1.130	-0.717	22.04	0.132	0.0526	34.57	0.35%	0.22%
WY130-140	6.904	2.693	1.127	-0.706	21.52	0.137	0.0547	33.96	0.36%	0.21%
WY190-200	6.610	2.664	1.085	-0.681	22.03	0.135	0.0542	34.20	0.36%	0.21%
WY240-250	6.579	2.877	1.118	-0.708	22.08	0.146	0.0582	32.90	0.36%	0.19%
WY330-350	6.420	2.715	1.130	-0.721	22.30	0.138	0.0554	33.80	0.32%	0.22%
WY455-473	7.188	2.734	1.125	-0.697	21.12	0.139	0.0556	33.76	0.31%	0.21%
WY535-550	7.254	2.711	1.589	-0.695	21.05	0.138	0.0551	33.94	0.32%	0.20%
WY585-600	6.421	2.641	1.128	-0.720	22.32	0.134	0.0536	34.30	0.37%	0.22%
WY600-610	6.326	2.622	1.129	-0.723	22.50	0.133	0.0533	34.44	0.36%	0.22%

^a equivalent to $(f_{35} + f_{epi,35}) \times 100$

^b equivalent to $(f_{39} + f_{epi,39}) \times 100$

Bibliography

- [And86] Andrews, J. N., J. -Ch. Fontes, J. -L. Michelot and D. Elmore, *In-situ* neutron flux, ^{36}Cl production and groundwater evolution in crystalline rocks at Stripa, Sweden, *Earth Planet. Sci. Lett.* **77**, p 49-58, 1986.
- [Atk86] Atkinson, T. C., K. Briffa, G. R. Coope, J. M. Joachim and D. W. Perry, Climate Calibration of coleopeteran data. In *Handbook of Holocene Palaeoecology and Palaeohydrology*, ed B. E. Berlund, p 851 – 858, Chichester: Wiley, 1986.
- [Bal94] Ballantyne, C. K and C. Harris, *Periglaciation of Great Britain*, Cambridge University Press, 1994.
- [Bar55] Bartholomew, R. M., A. W. Boyd, F. Brown, R. C. Hawkings, M. Lounsbury, and W. F. Merritt, The Half-Life of ^{36}Cl , *Can. J. Phys.* **33**, p 43, 1955.
- [Ben92] Benn D.I., Lowe, J.J. & Walker M.J.C., Glacier response to climatic change during the Loch Lomond Stadial and early Flandrian: geomorphological and palynological evidence from the Isle of Skye, Scotland, *J. Quat. Sci.*, **7**, p 125-144, 1992.
- [Bet40] Bethe, H. A., S. A. Korff, and G. Placzek, On the interpretation of neutron measurements in cosmic radiation, *Phys. Rev.*, **56**, p 573-587, 1940.
- [Bev92] Bevington, P. R. and D. K. Robinson, *Data Reduction and Error Analysis for the Physical Sciences*, second edition, McGraw-Hill, 1992.
- [Bou79] Boulton, G. S., and A. S. Jones, Stability of temperate ice caps and ice sheets resting on beds of deformed sediment. *Journal of Glaciology* **24**, p 29-44, 1979.

- [Cha71] Charalambus, S., Nuclear Transmutation by Negative Stopped Muons and the Activity Induced by the Cosmic-Ray Muons, *Nucl. Phys.* **A166**, p 145-161, 1971.
- [Cha97] Bruce Chappell, private communication, 1997.
- [Cla95] Clark, D. H., P. R. Bierman and P. Larsen, Improving *in situ* cosmogenic chronometers, *Quaternary Research*, **44**, p 366-376, 1995.
- [Con86] Conard, N. J., D. Elmore, P. W. Kubik, H. E. Grove, L. E. Tubbs, B. A. Chrunyk and M. Wahlen, The chemical preparation of AgCl for measuring ^{36}Cl in polar ice with accelerator mass spectrometry. *Radiocarbon* **28**, p 556-560, 1986.
- [Con50] Conversi, M., Experiments on cosmic-ray mesons and protons at several altitudes and latitudes. *Phys. Rev.* **79**, p 749-767, 1950.
- [Coo66] Cooper, J. A., I. D. Martin and M. J. Vernon, Evaluation of rubidium and iron bias in flame photometric potassium determination for K-Ar dating, *Geochem. Cosmochim. Acta*, **30**, p 197 - 205, 1966.
- [Dee93] Deer, W. A., R. A. Howie and J. Zussman, *An Introduction to the Rock-Forming Minerals* 2nd Edition, Longman Scientific and technical, Longman Group UK Ltd, 1993.
- [Dep94] Dep, L., D. Elmore, M. Lipschutz, S. Vogt, F. M. Phillips, M. G. Zreda, Production rate systematics of *in-situ* produced nuclides in terrestrial rocks: Monte Carlo methods, *Nucl. Instr. Meth.*, **B92**, p 321 - 325, 1994b.
- [Dep95] Dep, L. D., *Cosmogenic radionuclide production in terrestrial rocks: Accelerator mass spectrometry measurements and Monte Carlo simulations*, Ph.D. Dissertation, Purdue University, 1995.
- [Eva93] Evans, J. M., Determination of the production rate of *in-situ* chlorine-36 as a function of depth in limestone: with emphasis on the production due to negative muons, Honours thesis, The Australian National University, 1993.
- [Eva97] Evans, J. M., J. O. H. Stone, L. K. Fifield and R. G. Cresswell, Cosmogenic chlorine-36 production in K-feldspar, *Nucl. Instr. Meth.*, **B123**, p 334 - 340, 1997.

- [Eva80] Evans, Keenan L., and Carleton B. Moore, Combustion-Ion Chromatographic Determination of Chloride in Silicate Rocks, *Anal. Chem.* **52**, p 1908-1912, 1980.
- [Eva81] Evans, Keenan L., James G. Tarter, and Carleton B. Moore, Pyrohydrolic-Ion Chromatographic Determination of Fluorine, Chlorine, and Sulfur in Geological Samples, *Anal. Chem.* **53**, p 925-928, 1981.
- [Fab88] Fabryka-Martin, J. T., Production of Radionuclides in the Earth and their Hydrogeologic Significance, With Emphasis on Chlorine-36 and Iodine-129, Ph.D. Dissertation, University of Arizona, 1988.
- [Fei68] Feige, Y., B. G. Oltman and J. Kastner, Production rates of neutrons in soils due to natural radioactivity. *J. Geophys. Res.* **73**, p 3135 - 3142, 1968.
- [Fif94] Fifield, L. K., G. L. Allen, J. Stone and T. R. Ophel, The ANU AMS system and research program. *Nucl. Inst. Meth.*, **B92**, p 85 - 89, 1994.
- [Fif99] Fifield, L. K., Accelerator mass spectrometry and its applications, *Rep. Prog. Phys.* **62**, p 1223 - 1274, 1999.
- [Gla55] Glasstone, S., Principles of Nuclear Reactor Engineering. D. van Nostrand, Princeton, New Jersey, 1955.
- [Gol66] Goldstein, G., Partial Half-Life for beta-decay of ³⁶Cl, *J. Inorg. Nucl. Chem.* **28**, p 937, 1966.
- [Gra91] Gray J.M. & P. Coxon, The Loch Lomond Stadial glaciation in Britain and Ireland. In: Ehlers, J., Gibbard, P.L. and Rose, J., eds. *Glacial deposits in Great Britain and Ireland*. Balkema, Rotterdam, p 89-105, 1991.
- [Gre97] The Greenland Summit Ice Cores CD-ROM, University of Colorado at Boulder, and the World Data Center-A for Paleoclimatology, National Geophysical Data Center, Boulder, Colorado, 1997.
- [Hay69] Hayakawa, S., Cosmic Ray Physics, Interscience Monographs and Texts in Physics and Astronomy, Vol. XXII, John Wiley & Sons, New York, 1969.

- [Hei97] Heisinger, B., M. Niedermayer, F. J. Hartmann, G. Korschinek, E. Nolte, G. Morteani, S. Neumaier, C. Petitjean, P. Kubik, A. Synal, S. Ivy-Ochs, *In-Situ* Production of radionuclides at great depths, Nucl. Instr. Meth., **B123**, p 341 – 346, 1997.
- [Hei00] Heisinger, B., and E. Nolte, Cosmogenic in-situ production of radiogenic nuclides: Exposure ages and erosion rates, Nucl. Instr. Meth., **B172**, p 790 – 795, 2000.
- [Hen66] Hendrick, L. D. and R. D. Edge, Cosmic-ray neutrons near the earth, Phys. Rev. **145**, p 1023-1025, 1966.
- [Lal67] Lal, D. and B. Peters, Cosmic Rays produced radioactivity on Earth, in: Handbuch der Physik, XLVI/2, Springer, Berlin, p 551-612, 1967.
- [Lal88] Lal, D., In Situ-produced cosmogenic isotopes in terrestrial rocks, Ann. Rev. Earth Planet. Sci. 1988, **16**, p 355 – 388, 1988.
- [Lal91] Lal, D., Cosmic ray labelling of erosion surfaces: *in situ* nuclide production rates and erosion models, Earth. Planet. Sci. Lett, **104** p 424-439, 1991.
- [Lin63] Lingenfelter, R. E., Production of carbon 14 by cosmic-ray neutrons, Rev. geophys. **1**, 3p 5 – 55, 1963.
- [Lin76] Lingenfelter, R. E., Cosmic ray produced neutrons and nuclides in the earth's atmosphere, in: Spallation nuclear reactions and their applications, B.S.P. Shen and M. Merker, eds., p 193-205, Reidel, Dordrecht, 1976
- [Lit87] Litherland, A. E., Fundamentals of Accelerator Mass Spectrometry, Phil. Trans. R. Soc. Lond. A **232**, p 5-21, 1987.
- [Liu94] Liu, B., F. M. Phillips, J. T. Fabryka-Martin, M. M. Fowler, and W. D. Stone, Cosmogenic ^{36}Cl accumulation in unstable landforms, 1. Effects of the thermal neutron distribution. Water Resources Research, **30**, p 3115 – 3125, 1994
- [Lyo86] Lyons, Louis, Statistics for Nuclear and Particle Physicists, Cambridge University Press, 1986.

- [Koh92] Kohl, C. P., and K. Nishiizumi, Chemical isolation of quartz for measurements of in-situ produced cosmogenic nuclides, *Geochim. Cosmochim. Acta*, **56**, p 3583, 1992
- [Mac80] MacPherson, J. B., Environmental changes during Loch Lomond Stadial: evidence from a site in the Upper Spey Valley, Scotland. In J. J. Lowe, J. M. Gray & J. E. Robinson (eds.), *Studies in the Lateglacial of North-west Europe*. 89-102 Oxford: Pergamon, 1980.
- [Mas95] Masarik, J. and R.C. Reedy, Terrestrial cosmogenic-nuclide production systematics calculated from numerical simulations, *Earth and Plan Sci. Lett.* **136** p 381-395, 1995
- [Mas96] Masarik, J. Reedy, R. C., Monte carlo simulation of in-situ-produced cosmogenic nuclides. *Radiocarbon*, **38**(1): 163, 1996.
- [Mez86] Mezger, L., D. Burbank, Geological Society of America Abstracts with Programs **18**, p 157, 1986.
- [Mon36] Montgomery, C. G. and D. D. Montgomery, The intensity of neutrons of thermal energy in the atmosphere at sea level, *Phys. Rev.* **56**, p 10-12, 1936.
- [Nis89] Nishiizumi, K., E. L. Winterer, C. P. Kohl, J. Klein, R. Middleton, D. Lal and J. R. Arnold, Cosmic ray production rates of ^{10}Be and ^{26}Al in quartz from glacially polished rocks, *J. Geophys. Res.* **94**, 17, p 907-17,915, 1989.
- [Nis91a] Nishiizumi, K., C. P. Kohl, J. R. Arnold, J. Klein, D. Fink and R. Middleton, Cosmic-ray produced ^{10}Be and ^{26}Al in Antarctic rocks: Exposure and erosion history., *Earth Planet. Sci. Lett.* **104**, p 440-454, 1991a.
- [Nis91b] Nishiizumi, K., C. P. Kohl, E. M. Shoemaker, J. R. Arnold, J. Klein, D. Fink and R. Middleton, ^{10}Be - ^{26}Al exposure ages at Meteor Crater, Arizona, *Geochim. Cosmochim. Acta.* **55**, p 2699-2703, 1991b.
- [Nor89] Norstrom D. K., S. Lindblom, R. J. Donahoe, and C. C. Barton. Fluid inclusions in the Stripa granite and their possible influence on the groundwater chemistry. *Geochim. Cosmochim. Acta.* **53**, p 1741-1755, 1989.

- [O'Br78] O'Brien, Cosmic Ray Induced Neutron Background Sources and Fluxes for Geometries of Air Over Water, Ground, Iron, and Aluminium, *J. Geophys. Res.* **83**, p 114-120, 1978.
- [O'Su00] O'Sullivan, P. B., D. L. Gibson, B. P. Kohn, B. Pillans and C. F. Pain, Long-term Landscape Evolution of the Northparkes Region of the Lachlan Fold Belt, Australia: Constraints from Fission Track and Paleomagnetic Data, *Jour. Geol.* **108**, p 1-16, 2000.
- [Pea89] Peacock, J. D., D. Harkness, R. A. Housley, J. A. Little and M. A. Paul, Radiocarbon ages for a glaciomarine bed associated with the maximum of the Loch Lomond Readvance in West Benderloch, Argyll, *Scott. J. Geol.*, **25**, (1), 69-79, 1989.
- [Phi95] private communication with Dr John Stone, 1995.
- [Phi96] Phillips, M. Fred, Marek G. Zreda, and Montgomerv R. Flinsch, A reevaluation of cosmogenic ^{36}Cl production rates in terrestrial rocks, *Geophys. Res. Letters*, Vol 23 No 9, p 949-952, 1996.
- [Pre87] Press, W. H., B. P. Flannery, S. A. Teukolsky, W. T. Vetterling, *Numerical Recipes*, p 529 -539, Cambridge University Press, 1987.
- [Ros87] Rose, J., Status of the Wolstonian Glaciation in the British Quaternary, *Quaternary Newsletter* **53**, p 1-9, 1987.
- [Ros88] Rose, J., J. J. Lowe & R. A. Switsur, A Radiocarbon date on plate detritus beneath till from the type area of the Loch Lomond Readvance, *Scottish Journal of Geology*, **24**, p 113, 1988.
- [Rud77] Ruddiman, W. F., C. D. Sancetta, & A. McIntyre, Glacial/interglacial response rate of subpolar North Atlantic water to climate change: the record of ocean sediment. *Philosophical Transactions of the Royal Society of London* **280 B**, p 119-142, 1977.
- [Sat90] Satcher, G. R., *Introduction to Nuclear Reactions* 2nd edition, Oxford Uni Press, New York, 1990
- [She92] Shea, M. A. and D.F. Smart, Recent and Historical Solar Proton Events, *Radiocarbon* **34**, 2, p 255-262, 1992

- [She76] Shen, B. S. P., Spallation nuclear reactions and their applications, 1-8. Shen and Merker (eds), D. Reidel Publishing company, Holland, 1976.
- [Sim51] Simpson, J. A., Neutrons produced in the atmosphere by the cosmic radiations, *Phys. Rev.* **83** (6), p 1175-1188, 1951.
- [Ste83] Stephan, H. -J., and J. Ehlers, North German till types. In J. Ehlers (ed.), *Glacial Deposits in North-West Europe*: p 239-247. Rotterdam: Balkema, 1983.
- [Sto94] Stone, J., G. L. Allan, L. K. Fifield, J. M. Evans and A. R. Chivas, Limestone erosion measurements with cosmogenic chlorine-36 in calcite – preliminary results from Australia, *Nucl. Instr. Meth.*, **B92**, p 311 – 316, 1994.
- [Sto96] Stone, J., K. Lambeck, L. K. Fifield, J. M. Evans, R. G. Cresswell, A Lateglacial age for the Main Rock Platform, western Scotland, *Geology*, **24**, 8, p. 707-710, 1996
- [Sto97] Stone, J. O. H., G. Allen, L. K. Fifield and R. G. Cresswell, Cosmogenic chlorine-36 from calcium spallation, *Geochim. Cosmochim. Acta* **60**, p 679-692, 1997.
- [Sto98] Stone, J. O. H., J. M. Evans, L. K. Fifield, G. Allen and R. G. Cresswell, Cosmogenic chlorine-36 production in calcite by muons, *Geochim. Cosmochim. Acta* **62**, p 433-454, 1998.
- [Sto01] Stone, J. O. H., private communication, 2001.
- [Sut84] Sutherland, D. G., The Quaternary deposits and landforms of Scotland and the neighbouring shelves: a review. *Quaternary Science Reviews* **3**: p 157-254, 1984.
- [Sut85] Sutton, S. R., Thermoluminescence measurements on shock-metamorphosed sandstone and dolomite from Meteor Crater, Arizona: 2. Thermoluminescence age of Meteor Crater, *J. Geophys. Res.* **90**, p 3690-3700, 1985.
- [Swa92] Swanson, T. W., P. Sharma, F. M. Phillips, and M. Zreda, Determination of Chlorine-36 production rates from the deglaciation history of Whibey Island, WA (*Abs*), *Symposium on Accelerator Mass Spectrometry: Applications of Rare Isotopes as Traces in*

Science and Technology, Division of Nuclear Chemistry and Technology, San Francisco, CA, 1992.

- [Swa94] Swanson, T. W., Determination of Chlorine-36 production rates from the deglaciation history of Whibey Island, Washington, , Ph.D. Dissertation, University of Washington, 1994.
- [Swe54] Swetnick, M. J., Cosmic-ray neutrons in water at an altitude of 10,600 feet, *Phys. Rev.*, **95**, p 793-796, 1954.
- [Twi00] Twidale, C. R., Early Mesozoic (?Triassic) Landscapes in Australia: Evidence, Argument, and Implications, *Journ Geol*, **108**, p 537-552, 2000.
- [Van73] Vandenbosch, R. and J. R. Huizenga, *Nuclear Fission*, Academic Press, 1973.
- [Win56] Winsberg, L. The production of chlorine-39 in the lower atmosphere by cosmic radiation, *Geochim. Cosmochim. Acta*, **9**, p 183 - 189, 1956
- [Wyk65] Wykoff, J. M., B. Ziegler, H. W. Kocj, and R. Uhlig, Total photonuclear cross sections for low atomic number elements, *Phys. Rev.* **137**, p B576 - B594, 1965
- [Yam66] Yamashita, M., L. D. Stephens and H. W. Patterson, Cosmic-ray-produced neutrons at ground level: neutron production rate and flux distribution, *J. Geophys. Res.* **71**, p 3817-3834, 1966.
- [Yok77] Yokoyama, Y., I. L. Revss and F. Guichard, Production of radionuclides by cosmic rays at mountain altitudes, *Earth Planet. Sci. Lett.* **36**, p 44 - 50, 1977.
- [Zre91] Zreda, M. G., F. M. Phillips, D. Elmore, P. W. Kubik, P. Sharma and R. I. Dorn, Cosmogenic Chlorine-36 Production Rates in Terrestrial Rocks: Earth and Planetary Science Letters, **105**, p 94-109, 1991.
- [Zre94] Zreda, M. G., Ph.D. Dissertation, New Mexico Institute of Mining and Technology, 1994.

Missing References

[Bie95] Bierman, P., A. Gillespie, M. Caffee, Cosmogenic Ages for Earthquake Recurrence Intervals and Debris-Flow Fan Deposition, Owens Valley, CA. *Science*, **270**, 447-450, 1995.

[Phi01] Phillips F. M., W. D. Stone and J. T. Fabryka-Martin, An improved approach to calculating low-energy cosmic-ray neutron fluxes near the land/atmosphere interface, *Chem. Geol.* **175**, 689 - 701, 2001.

[Phi95] should read

[Phi95] Phillips, F., private communication with Dr John Stone, 1995.